
Trends in
Biomaterials
and
Artificial Organs

Editors-in-Chief

Dr. Harikrishna Varma, FBAO

*Head, Biomedical Technology Wing
Sree Chitra Tirunal Institute for Medical Sciences & Technology,
Poojappura, Thiruvananthapuram 695012, India*

Dr. Chandra P Sharma, FBSE, FBAO

Founder SBAOI & STERMI

sbaoi

Published by the **Society for Biomaterials and Artificial Organs (India)**

Trends in Biomaterials and Artificial Organs

Editors-in-Chief

Dr. Harikrishna Varma

Sree Chitra Tirunal Institute for Medical Sciences & Technology, India

Dr. Chandra P Sharma

Founder, SBAOI & STERMI, India

Associate Editors

Prof. Gilson Khang

Chonbuk National University, Republic of Korea

Prof. Devendra Kumar Agrawal

Creighton University, USA

Dr. Manoj Komath

Sree Chitra Tirunal Institute for Medical Sciences & Technology, India

Managing Editor

Mr. Willi Paul

Sree Chitra Tirunal Institute for Medical Sciences & Technology, India

Trends in Biomaterials and Artificial Organs is a peer reviewed international journal incorporating research mainly related to Biomaterials, Artificial Organs, Tissue Engineering, Regenerative Medicine and Drug Delivery. The journal publishes Original Research Articles, Short Communications, Review Articles and Letter to Editor, in English language. The focus of publication is centred on the synthesis, characterisation and biocompatibility studies of biomaterials and the design, validation and performance evaluation of medical devices. Biomaterials include synthetic materials falling in the classes of metals, alloys, polymers and ceramics, as well as natural materials like chitosan, silk, collagen and processed animal and human tissues. Composite forms of these materials and nanostructures have made their impact in this area and fabrication techniques like 3D bioprinting is changing the scenario. Innovative devices, implants and prostheses are being developed, spanning across various medical specialities like cardiovascular, neurological, orthopaedic, maxillofacial, spinal and ophthalmic, along with dentistry. The topics of interest extend to scaffolds fabrication and tissue regeneration aspects and to diagnostic devices and drug delivery systems.

Trends in Biomaterials and Artificial Organs provides a platform for sharing the state-of-the-art information on the role of biocompatible materials and their structures and functional ensembles, in enhancing the quality of life. Objective of the journal is to act as a catalyst in the rapid growth of Biomedical research and support its translation to products useful for healthcare.

International Editorial Board

Dr. Ika Dewi Ana

Gadjad Mada University, Indonesia

Prof. Hsin-Cheng Chiu

National Tsing Hua University, Taiwan

Prof. Allan S. Hoffman

University of Washington, Seattle, USA

Prof. Sachiko Iseki

Tokyo Medical and Dental University, Japan

Prof. Subhas C. Kundu

University of Minho, Portugal

Prof. Ki Dong Park

Ajoun University Seoul, South Korea

Prof. Erhan Piskin

Hacettepe University, Turkey

Prof. Laura Poole-Warren

The University of New South Wales, Australia

Prof. Seeram Ramakrishna

National University of Singapore, Singapore

Dr. Viktor I. Sevastianov

Institute of Transplantology and Artificial Organs, Moscow, Russia

Dr. Hideharu Shintani

Chuo University, Japan

Dr. Vishwa P. Srivastava

CBEAS, Purbanchal University, Nepal

Prof. Justin Cooper White

University of Queensland, Australia

Prof. Yoshiyuki Yokogawa

Osaka City University, Osaka, Japan

Prof. Xing Dong Zhang

Sichuan University, China

Dr. Kantesh Balani

Indian Institute of Technology Kanpur, India

Prof. Bikramjit Basu

Indian Institute of Technology, Kanpur, India

Dr. Naresh Bhatnagar

Indian Institute of Technology Delhi, India

Dr. Santanu Dhara

Indian Institute of Technology Kharagpur, India

Prof. Bhuvanesh Gupta

Indian Institute of Technology Delhi, India

Dr. Dharendra S. Katti

Indian Institute of Technology Kanpur, India

Prof. Veena Kaul

Indian Institute of Technology Delhi, India

Prof. Naveen Kumar

Indian Veterinary Research Institute, Bareilly, India

Prof. T.S. Sampath Kumar

Indian Institute of Technology Madras, India

Dr. Biman B. Mandal

Indian Institute of Technology Guwahati, India

Dr. Geetha Manivasagam

VIT University, Vellore, India

Dr. N. Rajendran

Anna University, Chennai, India

Dr. Neetu Singh

Indian Institute of Technology Delhi, India

Dr. T.M. Sridhar

University of Madras, Chennai, India

Dr. A.M. Balamurugan

Bharathiar University, Coimbatore, India

Trends in Biomaterials and Artificial Organs is a peer reviewed journal publishing four issues per volume, per year.

Published by the **Society for Biomaterials and Artificial Organs (India)**

Editorial Office : Room No. CAF/210, Satelmond Palace Campus, SCTIMST, Poojappura, Trivandrum 695012, India

Phone: +91 471 2520434; Web Site: <http://www.biomaterials.org.in/tibao> E-mail: editor.tibao@gmail.com

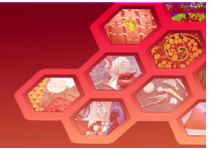


Table of Contents

Stable Solid Magnetic Nanoparticles: With a Potential for Nucleic Acid Recovery and Delivery	1
<i>S.R. Sreelekshmi, Susan Mani, S. Suresh Babu, Francis Boniface Fernandez, P.R. Harikerishna Varma</i>	
Aqueous Cissus quadrangularis Stem Extract Integrated Biodegradable Tissue Engineering Scaffold Augments Early Biomimetic and Biomineralization <i>In Vitro</i>	8
<i>Praseetha R. Nair, S. Sreeja and G. S. Sailaja</i>	
Stress Analysis During Occlusal Loading in a Human Skull with Maxillary Defect: A Finite Element Study	15
<i>Varadaraju Magesh, Pandurangan Harikerishnan, Arayambath Balamani, Elumalai Canmany, Akash Kasatvar, Ramamurthy Suresh</i>	
Differential Surface Thrombogenicity of Heparin Coated Bovine Pericardium: Implication in Bioprosthetic Valve Fabrication	19
<i>Sachin J. Shenoy, S.L. Devika, Vivek V. Pillai, G. Maneesha, P.R. Umashankar, G. Ranjith</i>	
Polysaccharide-PVA/PEG blended Crosslinked Hybrid Hydrogels for Cardiac Tissue Engineering	27
<i>Soumya K. Chandrasekhar, Joshi C. Onseph</i>	
A Novel Use of Tissue Conditioner as a Local Drug Delivery Medium for Microbial Control around Dental Implants: <i>In Vitro</i> Release Studies of Antibiotics and Curcumin	36
<i>Vibha Shetty, R. Deveswaran, Beena Antony, Shrestha Shetty, K. Ranganath</i>	
Yeast: A Potential Vaccine Delivery Carrier	44
<i>V.C. Patole, J.G. Mahore, S.S. Deshkar, S. Shekade, A. Gutte</i>	
A Review on Biomedical Applications of Titanium Dioxide	49
<i>Pradeep C. Dathan, Deepak Nallaswamy, S. Rajeshkumar, Suja Joseph, Shabin Ismail, Lakshmi Ajithan, Leon Jose</i>	

Original Article

Stable Solid Magnetic Nanoparticles: With a Potential for Nucleic Acid Recovery and Delivery

S.R. Sreelekshmi, Susan Mani, S. Suresh Babu, Francis Boniface Fernandez*, P.R. Harikrishna Varma

Division of Bioceramics, Biomedical Technology Wing, Sree Chitra Tirunal Institute for Medical Sciences and Technology, Poojappura, Thiruvananthapuram 695012, India

Received: 30 May 2022

Accepted: 30 June 2022

Published online: 30 June 2023

Keywords: magnetic nanoparticles, nucleic acid, surface modification, diagnostics

Expanding scope of magnetic nanoparticles amongst various nucleic acid recovery methods is often questioned with the stability that it offers. Oxidation from magnetite state to maghemite state which is often accompanied by aggregation can affect their efficacy. Isolation of nucleic acid through conventional methods necessitates the need of precipitation, centrifugation and sophisticated equipment. Correspondingly, it initiates the outflow of aerosols into the working environment. Isolation assisted via magnetic nanoparticles can eliminate the spread of infection. High surface area possessed by iron oxide nanoparticles (IONPS) is an add-on property with its magnetic nature that enhances isolation from traces of nucleic acid. Present study involves surface modifications of IONPS using polyethyleneimine (PEI) and silicon alkoxide. This aims for an enhancement in stability of IONPS along with their binding and retrieval efficacy. Results validated using standard DNA confirmed a 70% retrieval efficacy for PEI coated IONPS. Silicon alkoxide surface modification offered improved life time and stability with a reduction in agglomeration of IONPS than PEI. Qualitative and quantitative analysis carried out confirmed the characteristics and stability of various IONPS and standard DNA. Automated DNA extraction can be seen as an extended goal for this technique.

© (2023) Society for Biomaterials & Artificial Organs #20061722

Introduction

Magnetic nanoparticles (MNPs) assisted nucleic acid retrieval techniques are opening up new avenues in diagnosis with the development of point of care diagnostic kits. An easy isolation and purification which is required for a quick, simple and robust method in the emerging field of diagnostics and medicine is offered by them. This also provides a high throughput method for isolation from diverse sources due to their ability to perform magnetically controlled aggregation, dispersion & purification. Retrieval using MNPs avoids column separation or vacuum filtration providing a device independent application. But the efficacy of MNPs have a linear dependence with its ability in retaining their magnetic nature for an extended time period. Aggregation, a consequence of strong dipole-dipole interaction reduces the homogeneous distribution of MNPs when kept in suspension form [1]. Similarly, interaction of MNPs with atmosphere results in oxidation, consequently switching its state from magnetite to maghemite. Correspondingly, its magnetic

nature shifts from paramagnetic to ferromagnetic upon this conversion which reduces saturation magnetization in turn reducing the magnetic property [2]. Nanoparticles also possess an advantage of high surface area to volume ratio when compared to macro and bulk particles. As a result, MNPs offers more reactive sites for DNA to bind with which varies increases with the reduction in particle size.

Stability of magnetic nanoparticles can be retained subjective to the coatings applied on to them. The surface coating creates a corona around the MNPs that can simultaneously increase their stable shelf life along with prevention of oxidation [1]. In addition to this, stability of nanoparticles is also achieved along with their protection against corrosion (acid and basic) [3].

We provide data on iron oxide nanoparticles (IONPS) that were synthesized by coprecipitation method. Further to have a comparative study of their stability and reliability with surface modified IONPS, they were modified with silica and polyethyleneimine. Silica coated IONPS assures an easy release of DNA from its surface as they bind non-electrostatically with nucleic acid [4]. This modification exhibits higher stability over a wide

* Corresponding author

E-mail address: francisbf@scimst.ac.in (Dr. Francis Boniface Fernandez)

range of pH in aqueous conditions and is more resistant towards biodegradation than organic coating materials like chitosan etc [5]. The robustness and simplicity offered by this method makes it very valuable for low cost, large scale DNA and RNA separations [2]. Thickness of silica shell can be controlled by varying TEOS concentration which can directly influence the charge of the nanoparticle [6]. PEI is an organic cationic polymer alkyl chain with primary, secondary and tertiary amines [7]. Positive charge provided by the protonation of single nitrogen atom present in every three atoms found in the backbone can enable an electrostatic interaction with the negatively charged backbone of DNA [8-10]. PEI has an ability to neutralise excess anionic colloidal charge under different pH conditions.

Among the commercially available magnetic particles, Mag-bind, MagJET, Magmax are matrices based on silica, glass, agarose, cellulose, polystyrene and silane. But all these MNPs are available in a suspension form in an appropriate buffer. The presence of which can reduce its shelf life as the buffer can retain its property only up to 3-6 months [11]. While this method enables the storage of dry IONPS which can be resuspended at the user end depending upon their requirements.

Materials and Methods

Ferric chloride FeCl_3 (Sigma Aldrich), ferrous chloride tetrahydrate $\text{FeCl}_2 \cdot 4\text{H}_2\text{O}$ (Sigma Aldrich), polyethyleneimine (branched, MW – 25000) PEI (Sigma Aldrich), sodium hydroxide pellets NaOH (S.D. Fine), δ -DNA (TaKaRa), tetraethylorthosilicate (TEOS) $\text{SiC}_8\text{H}_{20}\text{O}_4$ (Sigma Aldrich), ammonium solution NH_4OH (Avantor), agarose low EEO superior grade (Sisco Research Laboratories), cetyl trimethyl ammonium bromide (CTAB) $\text{C}_{19}\text{H}_{42}\text{BrN}$ (Sisco Research Laboratories).

Synthesis of IONPS

Co-precipitation is the synthesis technique used where ferric chloride, FeCl_3 (0.1M) and ferrous chloride tetrahydrate $\text{FeCl}_2 \cdot 4\text{H}_2\text{O}$ (0.1M) were dissolved in HCl in Fe_3O_4 stoichiometric ratio. The mixture is drop wisely added into 2 M NaOH upon continuous heating and stirring in the presence of nitrogen for 20 minutes. This is followed by dropwise addition of 25% ammonia in the required amount under continuous stirring for 30 minutes.



The black slurry obtained is further modified by cooling, centrifugation and peptization. IONPS is preserved at room temperature as a suspension in distilled water and lyophilization is carried out afterwards (herein after, this synthesis route is referred to as U and synthesized IONPS as U-IONPS).

Surface modification of IONPS

Modifications were done in order to evaluate the retrieval efficacy of DNA using different IONPS.

Synthesis of Silica coated IONPS

For the synthesis of iron oxide nanoparticles, required proportion of FeCl_3 and $\text{FeCl}_2 \cdot 4\text{H}_2\text{O}$ is mixed together in distilled water. This is followed by dropwise addition of 25% ammonia in the required amount under continuous stirring for 30 minutes. Solution heated for 1 hour without boiling is further cooled, centrifuged and peptized. An aqueous sodium citrate solution is added to IONPS. Continuous stirring is given for about 30 minutes followed by the magnetic separation of IONPS (Herein after, this synthesis route is referred to as S and synthesized IONPS as S-IONPS). The separated IONPS were added to 90% ethanol taken in a round

bottom flask (RB) under continuous stirring. The solution was heated at a temperature below boiling point. Dropwise addition of TEOS diluted with purified ethanol and ammonia is done. The suspension is continuously stirred and lyophilized (herein after, this synthesis route is referred to as S1 and synthesized IONPS as S1-IONPS). Same procedure is done S1-IONPS for an additional coating and is preserved (herein after, this synthesis route is referred to as S2 and synthesized IONPS as S2-IONPS).

Synthesis of PEI coated IONPS

FeCl_3 and $\text{FeCl}_2 \cdot 4\text{H}_2\text{O}$ are separately dissolved in deionized water in the presence of nitrogen. Both are mixed together to which 0.1M CTAB and 5 M ammonia were added. Continuous stirring was given for 40 minutes. IONPS separated magnetically were washed and stored in vacuum desiccator for drying. 5M NH_4OH is added drop wisely to 20% PEI solution prepared in distilled ethanol. The solution is heated up to 50°C. Required quantity of dried IONPS is added and stirred continuously for 30 minutes. The suspension is magnetically separated, washed and stored in vacuum desiccator for drying. The samples were preserved at room temperature (herein after, this synthesis route is referred to as P and synthesized IONPS as P-IONPS).

Retrieval of Nucleic acid using IONPS

2 mg of IONPS (all types) were taken and washed with TE Buffer. 5 μg of δ DNA (0.35 $\mu\text{g}/\mu\text{l}$) is added to Eppendorf's containing IONPS and kept idle for some time. IONPS are magnetically separated and washed in ethanol. 20 μl of autoclaved water is added to DNA bound IONPS for elution and is kept in water bath maintained at 60°C. The IONPS are magnetically separated preserving the supernatant containing eluted DNA. The purity and concentration of DNA is analyzed using Nanodrop Spectrophotometer.

Physical Studies

The particle size and charge is determined using Dynamic Light Scatterer, DLS (Zetasizer Nanoseries, Nano ZS, Malvern Instruments). The concentration of the sample is adjusted to 0.1% w/v particles in distilled water. Before analysis, samples are sonicated to ensure uniform distribution.

Morphological Studies

The surface morphology of magnetic nanoparticles is analysed by scanning electron microscope, SEM (FEI, Quanta). IONPS suspended in distilled water is dropped onto a glass plate after sonication. Glass plate is then coated with Au/Pd material using sputter coater (E1010, Hitachi). This will ensure the conductivity to carry charged electrons across the surface.

For transmission electron microscope, TEM analysis, IONPS dispersed in distilled water after sonication is dropped onto the formvar coated TEM grid made of copper. Grid is allowed to dry. A magnified image of the sample is obtained with the help of electron beam ejected out of electron gun at a very high voltage (Hitachi H-7650).

Chemical Studies

Fourier transform infrared spectroscopy (FT-IR, Thermo Nicolet 5700 spectrometer (USA) gives information about various functional groups and components present in the sample. Spectrometer is operated in DRIFT mode. KBr powder (IR Grade) is mixed along with sample against KBr background. The sample is scanned between a wavelength region 4000 cm^{-1} - 400 cm^{-1} (mid IR Region) with 64 number of scans and 4 cm^{-1} resolution.

Energy dispersive X-ray spectroscopy (EDS) gives surface elemental compositions (FEI, Quanta). This microanalysis technique is accompanied with SEM. The X-Rays emitted from the sample during SEM analysis provides necessary information regarding samples elemental composition.

X-ray diffraction (XRD) provides the crystallinity and phase of samples (Bruker D8 Advance, Germany). Including their size, crystal structure, composition etc. Cu-K α radiation at a current of 30mA and voltage of 40KV is used for scanning. X-ray diffraction occurs when they collide with the sample depending up on the arrangement of planes in them. XRD pattern is a curve of 2θ v/s intensity; θ being the angle of diffraction. 2θ ranges from 20-80° with a speed rate of 2°/minute at a step size of 0.02 degree.

Magnetic studies

Vibrating sample magnetometer (VSM) having 10^{-6} emu sensitivity with 1 second averaging is used. Magnetic field up to 100kOe with field sweeping from -100kOe to +100kOe was used to determine saturation magnetism at 300K (Multipurpose Broad Band Probe with ATM (SmartProbe BB(F)-H-D 5mm – AZ: PH3723-500), broad band inverse probe with ATM (BBI Broad Band Inverse Probe H-BB-D 5mm – Z: PH3162-500)

DNA retrieval

To determine the purity and quantity of DNA retrieved, Nanodrop spectrophotometer (NanoDrop™ 2000/2000c) is used. This is a full spectrum UV-Vis microvolume spectrophotometers. They require samples less than 0.5 μ l which is dropped directly on the optical measurement surface of the instrument. Concentration and purity of DNA sample is the ratio of absorbance at 260 nm and 280 nm. Generally accepted ratio for pure DNA is 1.8 and 1.8-2.2 for pure nucleic acid. Between 0.4ng/ μ l and 15000ng/ μ l is the detection range of nanodrop spectrophotometer.

Luminescent image analyzer

Luminescent image analyzer (LAS 4000 Fuji Film, Japan) provides the fluorescence image of the gel after run. Gel upon illumination by different filters provides images using multipurpose CCD camera. EtBr intercalated with DNA shows enhanced fluorescence when illuminated with 312nm and 365 nm filter (UV region) at an exposure time is adjusted to 1/30th and 1/15th of a second.

Results

DLS and zeta potential

U-IONPS were found to be monodispersed with a particle size of 166 nm as per the DLS measurements whereas 743.7 nm and 669 nm for P-IONPS and S2-IONPS respectively. At pH=7, zeta potential of different IONPS were measured as +22.1 mV for U-IONPS, +43.4 mV for P-IONPS, -50.3 mV for S1-IONPS and -44.7 mV for S2-IONPS.

Morphological studies

SEM micrographs in figure 1 depicted the size of IONPS as 146nm for U-IONPS, 88 nm for P-IONPS, 372nm for S-IONPS, 394.5nm for S1-IONPS. IONPS were found to be clustered for S2-IONPS. TEM micrographs in figure 2 depicted the size of IONPS as 37.38 nm for U-IONPS, 64.24 nm for S-IONPS and 340.86 nm for S2-IONPS. The XRD pattern of U-IONPS (figure 3a) possess characteristic peaks of Fe₃O₄ at $2\theta = 29.878^\circ, 35.454^\circ, 42.891^\circ, 53.589^\circ, 57.015^\circ$ and 62.651° corresponding to (2 2 0), (1 1 0), (4 0 0), (4 2 2), (5 1 1) and (2 1 2) planes respectively. This exactly matches with the pattern of magnetite (pdf number – 01.071.6336 Magnetite). XRD pattern of P-IONPS (figure 3b) possess characteristic peaks of Fe₃O₄ at $2\theta = 30.251^\circ, 35.639^\circ$ and 43.220° corresponding to (220), (110) and (400) planes respectively. Broad and less intense peaks are seen between 10° and 20°, 40° and 50°

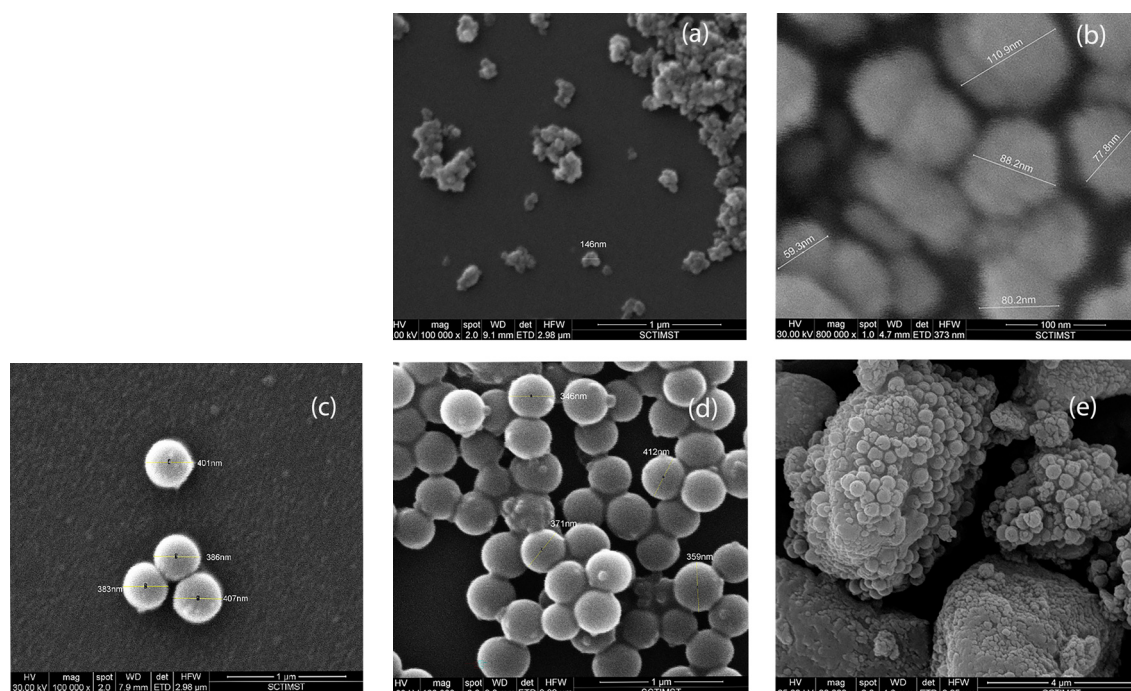


Figure 1: Effect of surface modifications on IONPS as depicted in SEM micrographs for various IONPS

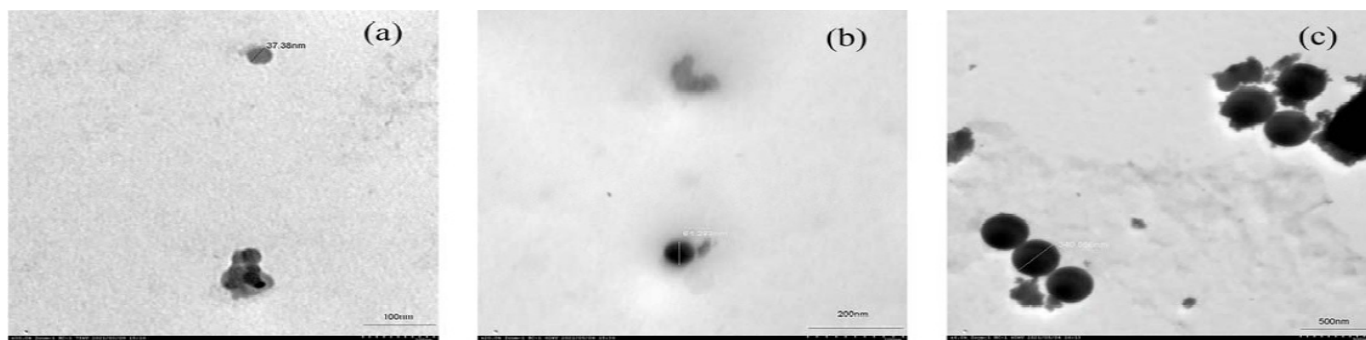


Figure 2: TEM micrographs of IONPS (a) U-IONPS (b) S-IONPS (c) S2-IONPS

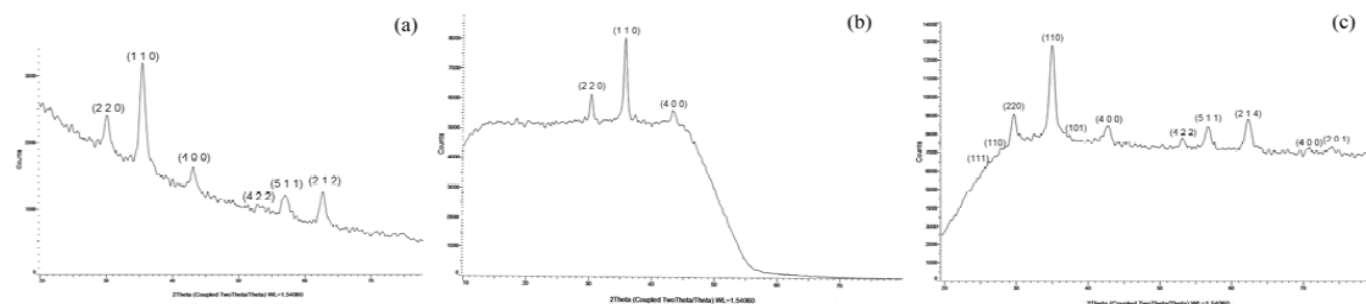


Figure 3: XRD Pattern of (a) U-IONPS, (b) P-IONPS, (c) S2-IONPS

while the XRD pattern of S2-IONPS (figure 3c) possess of characteristic peaks of Fe_3O_4 at $2\theta = 29.657^\circ, 34.990^\circ, 42.873^\circ, 53.124^\circ, 56.693^\circ$ and 62.303° corresponding to (220), (110), (400), (422), (511) and (212) respectively and characteristic peaks of silicon oxide at $2\theta = 26.161^\circ, 28.588^\circ, 37.384^\circ, 70.888^\circ, 73.963^\circ$

corresponding to (111), (110), (101), (400) and (201) respectively. This corresponds to peaks of magnetite (pdf number - 01.071.6336) and silicon oxide (pdf number - 00.013.0026).

From the Debye Scherrer's equation the size of the U-IONPS was found to be 102 nm, for S2-IONPS 103.8 nm and for P-IONPS 181.6 nm.

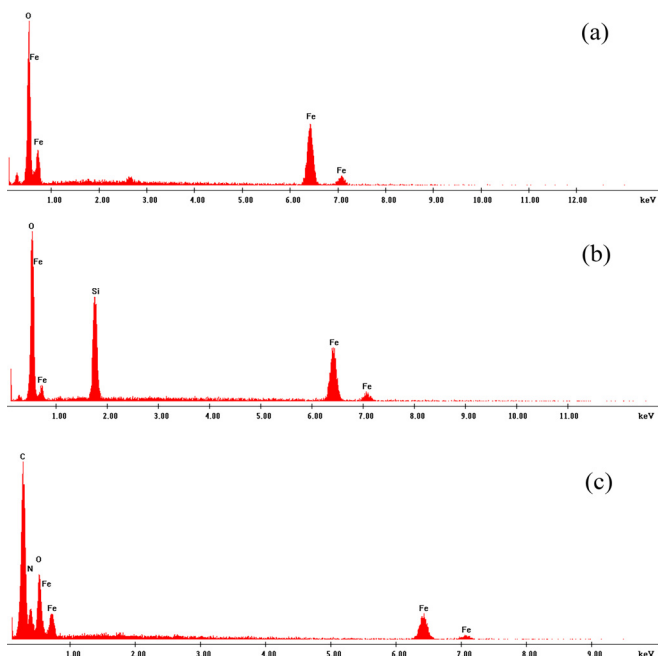


Figure 4: EDS Analysis to confirm the surface modifications on IONPS (a) U-IONPS, (b) P-IONPS, (c) S1-IONPS

EDS pattern

EDS pattern shows only the presence of Fe (Iron) and O (Oxygen) peaks at figure 4a. This ensures chemical purity of U-IONPS. The presence of silicon peaks (figure 4b) along with Fe and O peaks indicates the silica coating of S1-IONPS. Presence of C, O and N peaks in EDS pattern of P-IONPS (figure 4c) along with Fe peaks indicates the PEI coating.

FTIR Spectrum

FTIR spectrum of U-IONPS shows the characteristic band around 582 cm^{-1} and 557 cm^{-1} due to Fe-O stretching vibration (figure 5a) in Fe_3O_4 . In figure 5b, along with the characteristic band around 577 cm^{-1} due to the absorption of Fe-O, other characteristic bands around 1109 cm^{-1} corresponding to asymmetrical stretching vibrations of Si-O-Si and around 799 cm^{-1} corresponding to Si-O stretching vibrations were found. Thereby indicating the presence of silica coating on IONPS.

The FTIR pattern of P-IONPS shows additional characteristic bands apart from 543 cm^{-1} due to Fe-O vibration in Fe_3O_4 (figure 5c). The characteristic bands around 1397 cm^{-1} due to C-N stretching and around 2848 cm^{-1} due to C-H bond stretching present in PEI. The bands between 1553 cm^{-1} and 1646 cm^{-1} are due to NH_2 bending present in PEI. This confirms the presence of PEI coating on the IONPS.

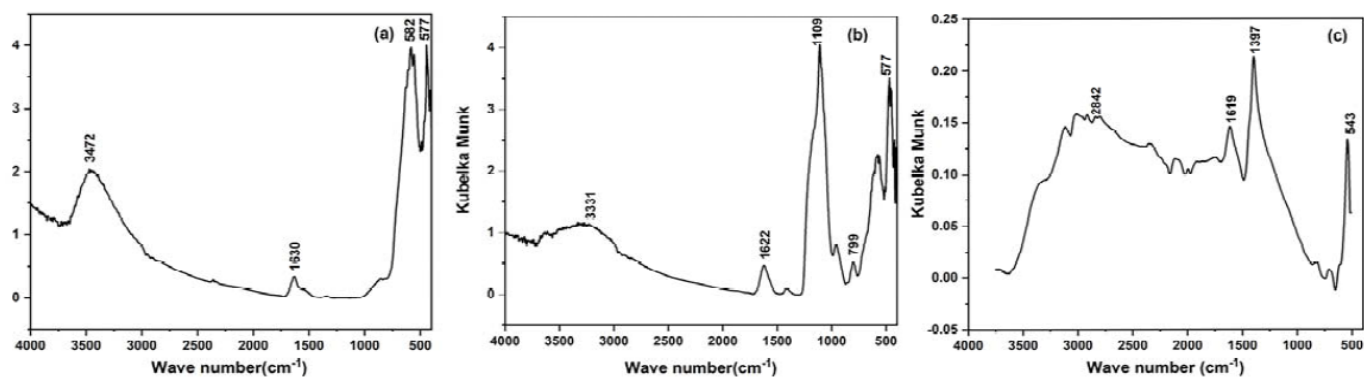


Figure 5: IR Spectrum of (a) U-IONPS, (b) S1-IONPS, (c) P-IONPS

VSM Analysis

A strong magnetic response in M-H curve is observed for all samples with an increase in magnetic field (figure 6). A sharp increase in magnetic field is seen within the range of 0 to 30kOe after with saturation is reached. Here, saturation magnetism of U-IONPS can be taken as a reference, 62 emu/g which varies upon coating. Maximum saturation magnetism (M_s) is observed for P-IONPS, 70 emu/g. Silica coating decreased M_s value to 42 emu/g and 40 emu/g for S1-IONPS and S2-IONPS respectively. Our sample exhibits zero residual magnetism and coercive force as seen from the graph i.e. no magnetism is retained in the material once external magnetic field is removed.

DNA Retrieval using IONPS

Nanodrop spectroscopic analysis confirmed the ability (table 1) of the coated and uncoated IONPS to retrieve nucleic acid and retrieval efficacy was calculated.

Discussion

IONPS offers numerous advantages in nucleic acid retrieval techniques. Isolation of nucleic acid through conventional methods necessitates the need of precipitation, centrifugation and

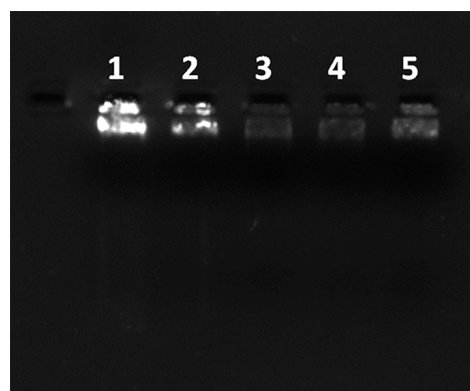


Figure 7: Agarose Gel Electrophoresis (1%) image of λ DNA retrieved using IONPS. Lane 1 control [λ DNA], Lane 2 U-IONPS alone, Lane 3 S1-IONPS, Lane 4 S2-IONPS, Lane 5 P-IONPS

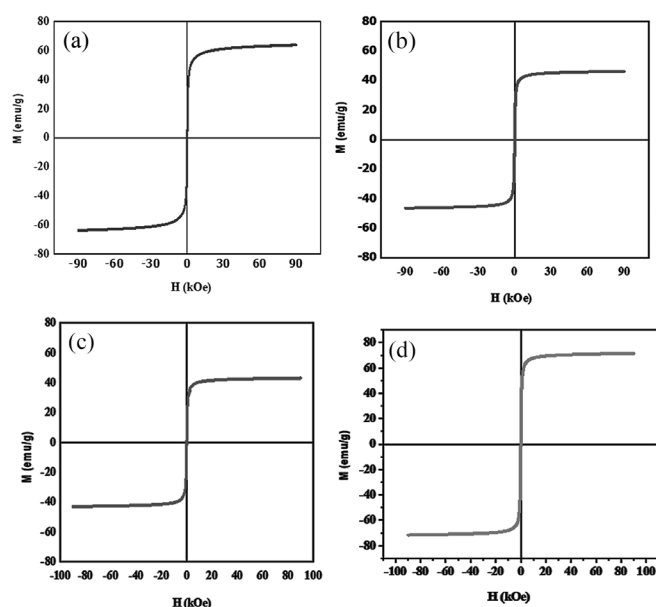


Figure 6: Magnetic responses of Superparamagnetic IONPS (a) U-IONPS, (b) P-IONPS, (c) S1-IONPS, (d) S2-IONPS

Table 1: Concentrations of λ DNA retrieved using different IONPS

IONPS	Initial concentration (ng/ μ l)	Retrieved concentration (ng/ μ l)	Retrieval Efficacy (%)
U-IONPS	246.00	131.00	53.25
P-IONPS	259.40	232.50	89.63
S1-IONPS	246.00	116.00	46.75
S2-IONPS	246.00	81.30	33.05
After 3 months			
U-IONPS	214.00	22.30	10.42
P-IONPS	350.00	144.00	41.14
S1-IONPS	214.00	93.50	43.69
S2-IONPS	214.00	49.40	23.08

sophisticated equipment while magnetic nanoparticle assisted retrieval techniques are quick, simple and robust. DNA adsorbed onto them can be simply eluted in water. At the same time, their performance is hindered due to their inability to hold its property in long run. Agglomeration of IONPS can directly influence their shelf life and will reduce its nucleic acid binding capacity. Higher the surface charge of IONPS, greater will be its shelf life. As the surface charge increases agglomeration is also reduced as equal charges gets repelled. The magnetic property possessed by the IONPS also need to be sufficient for magnetic separation.

These stability issues can be minimized by surface modifications to an extent by making IONPS in a buffer free format. Commercially available IONPS are suspended in proprietary buffer (Mag-bind, MagJET, Magmax).

U-IONPS synthesized here bear a positive charge which can initiate the adsorption via electrostatic interaction (phosphate backbone in DNA is negatively charged). The efficacy of nucleic acid isolation could be enhanced with the increase of positive charge as retrieval efficacy has a direct effect on positive charged IONPS.

Electrostatic interaction can be promoted by inducing positively charged moieties onto the IONPS [12] like PEI. This contributed to more positive charge on the IONPS in turn enhancing the electrostatic attraction [13]. Density of charge imparting amino groups in PEI can directly influence to the amount of DNA adsorbed [12]. The peaks corresponding to PEI were seen as broad and less intense peaks (figure 3b) due to the amorphous nature of PEI.

Surface modification of IONPS with PEI, showed that its retrieval efficacy increased up to 1.6 fold times as that of U-IONPS (table 1). PEI modification witnessed an increase in its magnetic properties as well (figure 6b). This has reduced agglomeration of molecules and increased the reactive site of IONPS. Though P-IONPS exhibit higher efficacy than U-IONPS, but they showed a shorter shelf life (table 1).

In order to address this stability issue, IONPS were modified with silicon alkoxide. In spite of the negative charge possessed by silicon alkoxide coating and increased agglomeration due to it, they exhibited an enhanced resistance towards degradation. Thereby, ensuring their stability and increased shelf life in a wider range of pH. IONPS shares a covalent bond with silicon alkoxide which strengthens the coating. Their bind with DNA is via non electrostatic bonding [13]. This agrees with the findings of Lee et al and Bertolucci et al [2] where he has examined the adsorption of DNA onto silicon alkoxide coated IONPS that takes place through intermolecular hydrogen bonds. Hydrogen bonds can occur between the unwound nucleotides and silica surface [14]. In addition to that, prevention of oxidation from magnetite to maghemite is also achieved. Surface modification by silicon alkoxide helps allows for further modification if required as the silanol groups can bind with other functional groups.

The results showed an enhanced stability of S1-IONPS when compared with both U-IONPS and P-IONPS (table 1). At the same time, silicon alkoxide coating on the surface of IONPS inhibits the penetration of external magnetic field into the sample (figure 6). This reduction in magnetization can also be considered as a way to confirm silicon alkoxide coating onto the IONPS [15]. Similar to the results obtained by M. Abbas et al. as the number of silicon alkoxide coatings on the IONPS, its magnetization decreased. They found a considerable decrease in the saturation magnetization when the external magnetic field varied from -15kOe to +15kOe at 300K

which is comparable to the results obtained here [16]. Silicon alkoxide coating did not exhibit any change in the retrieval efficacy. Comparable to the observation made by [17] gelation of silica resulted in formation of clusters which subsequently reduced specific surface area of IONPS (figure 1). Due to reduced reaction site of IONPS, DNA could not bind effectively with them.

As the literature says, magnetic properties of IONPS depends on their particle size and also on the coatings made on them [15]. The M-H magnetic responses curve of different IONPS synthesized by coprecipitation method confirms their magnetic property (figure 6). Superparamagnetism is the magnetic property shown by ferromagnetic materials when their size reduces down to single domain. This agrees with the fact that, size of the particles synthesized are in the nano-regime. As magnetization curve showed no hysteresis behavior, superparamagnetic nature of IONPS is proved. Wallyn, Anton, and Vandamme (2019) studied the nature of IONPS, their report can be correlated to confirm the superparamagnetic nature of synthesized IONPS. Neither remanence nor coercivity was observed in any of the samples.

Both the coatings were successful in the prevention of IONPS agglomeration [13]. The strong dipole-dipole interaction which exist between IONPS that results in agglomeration is avoided here (figure 1, figure 2). Large positive and negative charges for IONPS ensures greater stability. As the magnitude of charge increases, more is the repulsive force that exist between IONPS. This repulsion will prevent the particle agglomeration.

These IONPS synthesized is stored in dried form. When IONPS are suspended in buffer, oxidation will be initiated and the magnetic state of IONPS will shift from magnetite to maghemite in turn reducing its saturation magnetization. The charge of IONPS varies as the pH of buffer changes. This can possibly affect their retrieval efficacy [11]. This instability can be reduced when nanoparticles are stored in stable powdered form. The properties possessed by the IONPS are retained on resuspension. There by extending their flexibility in utilization, storage and application based on users needs.

Conclusion

In summary, we have validated the properties of iron oxide nanoparticles (IONPS) synthesized by co-precipitation method, further modified using silicon alkoxide and polyethyleneimine. Qualitative and quantitative analysis were carried out. Finding indicated that nucleic acid retrieval efficacy and saturation magnetization was higher for P-IONPS compared to other samples but they exhibit shorter shelf life. Surface modified IONPS using silicon alkoxide showed consistency in their retrieval efficacy and showed longer shelf life. Here, the storage of synthesized IONPS in solid form is an added advantage. Evaluation and optimization of parameters to increase the retrieval efficacy is also carried out. This strategy offers a magnetic nanoparticle mediated nucleic acid recovery limiting aerosol with better retrieval efficacy. This technique can be extended for automated DNA extraction.

Future Scope

As silicon alkoxide coating offers more sites for binding it enables further modifications. This can increase its acceptance in nuclei acid retrieval techniques. The retrieval efficacy and shelf of S1-IONPS can be compared with other silicon coating agents apart from TEOS.

Acknowledgement

The authors would like to acknowledge Dr. Manoj Komath, Head

Department of Biomaterial Science and Technology, Biomedical Technology wing, Sree Chitra Tirunal Insititue for Medical Sciences and Technology, Trivandrum.

References

1. Wallyn, Anton, and Vandamme. Synthesis, Principles, and Properties of Magnetite Nanoparticles for In Vivo Imaging Applications-A Review. *Pharmaceutics* 11 (11), 601 (2019).
2. Lee, Alex H.F., Steven F. Gessert, Yutao Chen, Nikolay V. Sergeev, and Babak Haghiri. Preparation of Iron Oxide Silica Particles for Zika Viral RNA Extraction. *Heliyon* 4 (3), e00572 (2018).
3. A G Pershina, A E Sazonov, V D Filimonov. Magnetic Nanoparticles - DNA Interactions: Design and Applications of Nanobiohybrid Systems. *Russian Chemical Reviews* 83 (4), 299–322 (2014).
4. J.R Sosa-Acosta, J.A. and Silva, L. Fernández-Izquierdo, S. Díaz-Castañón, M. Ortiz, J.C. Zuaznabar_Gardona, A.M. Díaz-García. Iron Oxide Nanoparticles (IONPs) with Potential Applications in Plasmid DNA Isolation, *Colloids and Surfaces A: Physicochemical and Engineering Aspects*, 545, 167–78 (2018).
5. Dae-Won Lee, and Hira Fatima, and Kyo-Seon Kim. 2018. “Preparation of Silica Coated Magnetic Nanoparticles for Bioseparation.” *Journal of Nanoscience and Nanotechnology* 18: 1414–18.
6. Kang, Kiho, Jinsub Choi, Joong Hee Nam, Sang Cheon Lee, Kyung Ja Kim, Sang-Won Lee, and Jeong Ho Chang. Preparation and Characterization of Chemically Functionalized Silica-Coated Magnetic Nanoparticles as a DNA Separator, *113(2)*, 536-543 (2009).
7. Danielle C. Arruda, Céline Hoffmann, Christine Charrueau, Pascal Bigey, Virginie Escriou. Innovative Nonviral Vectors for Small-Interfering RNA Delivery and Therapy, in *Nanostructures for Novel Therapy*, 713–40 (2017).
8. Adheesha N. Danthanarayana, , Danushika C. Manatunga, , Rohini M. De Silva, N. Vishvanath Chandrasekharan, and K.M. Nalin De Silva, Magnetofection and Isolation of DNA Using Polyethyleneimine Functionalized Magnetic Iron Oxide Nanoparticles. *Royal Society of Open Science* 5 (12), 181369 (2018).
9. Qiyi Feng, Yanping Liu, Jian Huang, Ke Chen, Jinxing Huang Kai Xia. Uptake, Distribution, Clearance, and Toxicity of Iron Oxide Nanoparticles with Different Sizes and Coatings, *Scientific Reports*, 8(1), 2082 (2018).
10. S.C. McBain, H.H.P. Yiu, A. El Haj J. Dobson. Polyethyleneimine Functionalized Iron Oxide Nanoparticles as Agents for DNA Delivery and Transfection. *Journal of Materials Chemistry* 17, 2561–65 (2007).
11. Bloemen, Maarten, Ward Brullot, Tai Thien Luong, Nick Geukens, Ann Gils, and Thierry Verbiest. Improved Functionalization of Oleic Acid-Coated Iron Oxide Nanoparticles for Biomedical Applications.” *Journal of Nanoparticle Research*, 14(9), 1100 (2012).
12. Kudr, Jiri, Yazan Haddad, Lukas Richtera, Zbynek Heger, Mirko Cernak, Vojtech Adam, and Ondrej Zitka. Magnetic Nanoparticles: From Design and Synthesis to Real World Applications. *Nanomaterials* 7(9), 243 (2017).
13. Tiwari, A. P., S. J. Ghosh, and S. H. Pawar. Biomedical Applications Based on Magnetic Nanoparticles:DNA Interactions. *Analytical Methods* 7(24), 10109–20 (2015).
14. Vandeventer, Peter E., Jessica S. Lin, Theodore J. Zwing, Ali Nadim, Malkiat S. Johal, and Angelika Niemz. Multiphasic DNA Adsorption to Silica Surfaces under Varying Buffer, PH, and Ionic Strength Conditions. *The Journal of Physical Chemistry B*, 116(19), 5661–70 (2012).
15. Bertolucci, Elisa, Anna Maria Raspolli Galletti, Claudia Antonetti, Mirko Marracci, Bernardo Tellini, Fabio Piccinelli, and Ciro Visone. Chemical and Magnetic Properties Characterization of Magnetic Nanoparticles. In *2015 IEEE International Instrumentation and Measurement Technology Conference (I2MTC) Proceedings*, 1492–96. Pisa, Italy: IEEE (2015).
16. Abbas, Mohamed, B. Parvatheeswara Rao, Md. Nazrul Islam, S.M. Naga, Migaku Takahashi, and CheolGi Kim. Highly Stable- Silica Encapsulating Magnetite Nanoparticles (Fe₃O₄/SiO₂) Synthesized Using Single Surfactantless-Polyol Process. *Ceramics International* 40(1), 1379–85 (2014).
17. Haddad, Yazan, Kledi Xhaxhiu, Pavel Kopel, David Hynek, Ondrej Zitka, and Vojtech Adam. The Isolation of DNA by Polycharged Magnetic Particles: An Analysis of the Interaction by Zeta Potential and Particle Size. *International Journal of Molecular Sciences* 17(4), 550 (2016).



Original Article

Aqueous *Cissus quadrangularis* Stem Extract Integrated Biodegradable Tissue Engineering Scaffold Augments Early Biomimetic and Biomineralization *In Vitro*

Praseetha R. Nair¹, S. Sreeja¹ and G. S. Sailaja^{*1,2,3}

¹Department of Polymer Science and Rubber Technology, ²Inter-University Centre for Nanomaterials and Devices (IUCND), ³Centre of Excellence in Advanced Materials, Cochin University of Science and Technology, Kochi 682022, India

Received: 9 December 2021
Accepted: 25 December 2022
Published online: 30 June 2023

Keywords: biodegradable scaffold, biomimetic mineralization, biomineralization, *Cissus quadrangularis*, aqueous extract

Biodegradable tissue engineering scaffolds with tunable degradation, high biocompatibility, adequate mechanical strength and intrinsic biomineralization potential instigating biomimetic interactions with osteogenic cells have been well-received for effective bone-defect repair. This study demonstrates the early biomimetic as well as biomineralization of aqueous stem extract (WE) of *Cissus quadrangularis* (CQ) integrated natural scaffold composed of chitosan and collagen (CC) with a tunable degradation profile. Results demonstrate that the scaffold (CC-WE) synergistically contributes to its biomineralization, water absorption capacity and tunable degradation. The microporous CC-WE with an average pore size of $43.13 \pm 13.59 \mu\text{m}$ attained complete swelling within 1h and maintained equilibrium swelling for 10 days and subsequently underwent controlled degradation (42.3% by day 60) under physiological pH and ambient temperature. Early biomimetic mineralization has been observed by SEM analysis after immersing CC-WE in simulated body fluid under biomimetic conditions for 7 days. In complementary, early biomineralization has been confirmed by Alizarin Red S (ARS) and von Kossa (VK) staining upon interaction with Human Osteosarcoma (HOS) cells for 7 days, viewed as respective coloured adduct formation. The findings, therefore, suggest innate biomineralization proficiency of CC-WE scaffold under a beneficial biological microenvironment to aid faster bone defect healing.

© (2023) Society for Biomaterials & Artificial Organs #20062222

Introduction

In the biomimetic therapeutic approach, natural systems are being emulated to mimic the structural and biofunctional features, presenting revolutionary contributions to effective tissue regeneration. Indeed, a significant number of natural as well as synthetic materials have been explored for regenerative tissue engineering by biomimetic approaches, including organic/inorganic matrices to augment biomineralization, a distinctive feature of osteogenesis [1, 2]. Such mineralized materials could function as superior matrices to facilitate a better cell-material interface triggering enhanced cell attachment, proliferation, and differentiation by promoting extracellular microarchitecture functions and simultaneously eliminating unfavourable cellular responses [3]. In particular, the cellular and molecular level interactions would be

key factors for the primary osteo-supportive microenvironment that leads to osteogenesis, thereby rectifying the bone defects.

The predominant requisites for a biomimetic bone graft essentially entail a hierarchically porous microstructure resembling the innate bone tissue microenvironment, a higher degree of compatibility with specific cells, controlled biodegradability to function as the supportive temporary extracellular matrix and invoke biomineralization of apatite with Ca/P ratio analogous to the stoichiometric ratio of host bone [1, 4]. Inspired by the natural mineralization process, collagen-based systems with diverse biological characteristics have been extensively used as tissue engineering scaffolds [5, 6].

The structural similarities with glycosaminoglycan and its biodegradable nature enable chitosan, the natural biocompatible polysaccharide, to function as a structural component of therapeutic tissue regeneration scaffolds [7]. Besides, it enhances the activity of growth factors to promote cell proliferation [7]. Moreover,

* Corresponding author
E-mail address: sailajags@cusat.ac.in (Dr. G.S. Sailaja)

chitosan is a cationic polyelectrolyte under acidic pH, contributed by its protonating primary amine groups, which leads to the formation of water-insoluble polyelectrolyte complexes with anionic substances [8]. Interestingly, collagen, a polyanionic fibrous protein that contains receptor-recognition repeats [9, 10], can form such ionic complexes with chitosan [8].

It is a vital factor to envisage that, in the native bone, the glycosaminoglycan in Extra Cellular Matrix (ECM) interweaves the fibrous structure of collagen to ensure mechanical stability to the bone tissue [7]. Hence, chitosan-collagen complex scaffolds could be expected to provide a favourable mechanical match with the host bone to be repaired and initiate osteogenic signals [7]. Furthermore, the chitosan-collagen scaffolds mimic the natural mineralization process and can act as an appropriate supportive platform to repair bone defects. [7]

Plants with medicinal significance are an enriched traditional resource, and extensive research is ongoing to investigate their active components towards formulating innovative therapeutic options [11]. *Cissus quadrangularis* Linn (CQ) is a perennial plant from the family *Vitaceae* with well-documented medicinal importance [12]. Various CQ stem extracts have extensively been investigated for osteoporotic defect repair and bone tissue regeneration applications [13,14]. Ethanolic CQ extract has been reported to induce bone regeneration in ovariectomized rats [13], while petroleum ether and hexane extracts of CQ have been investigated for their efficacy in bone fracture healing *in vitro* [14, 15]. We have recently reported a comparative evaluation of various extracts of CQ stem in augmenting biomineralization [16]. Our studies manifested that hexane and aqueous extracts have superior cell-proliferation and biomineralization index [17]. The therapeutic efficacy of these herbal medicines to invoke osteogenesis when combined with an appropriate supporting matrix in the form of a scaffold would complement each other for sustained functioning until the regeneration phase is complete.

Herein, we present a natural biodegradable bone scaffold, aqueous CQ stem extract (WE) integrated chitosan-collagen (CC), holding early biomimetic and biomineralization potential. Chitosan-collagen 75:25 (w/w) crosslinked with glyoxal has specifically been chosen owing to its optimum physico-chemical and mechanical characteristics, as per our recent study [16, 17]. The CC-WE scaffold has been evaluated for its physicochemical and morphological features, water absorption capacity and degradation behavior under physiological conditions. Subsequently, biocompatibility evaluation (MTT assay and actin-DAPI staining) and proficiency to induce Ca-P mineralization (in biomimetic conditions and after cell-scaffold interaction) were determined to present tangible evidence of matrix mineralization, a noticeable characteristic of a bone regenerative scaffold. The CC-WE demonstrates inherent early Ca-P mineralization, better cytocompatibility, hydrophilicity, and biodegradation; hence, it could be proposed as a suitable biofunctional scaffold for bone tissue repair and regeneration.

Materials and Methods

All the reagents for Phosphate Buffered Saline (PBS), Simulated Body Fluid (SBF) [Sodium chloride (NaCl), Potassium chloride (KCl), Potassium dihydrogen phosphate (KH_2PO_4), Di-sodium hydrogen phosphate dihydrate ($\text{Na}_2\text{HPO}_4 \cdot 2\text{H}_2\text{O}$), Sodium bicarbonate (NaHCO_3), Di-potassium hydrogen phosphate (K_2HPO_4), Magnesium chloride hexahydrate ($\text{MgCl}_2 \cdot 6\text{H}_2\text{O}$), Calcium chloride (CaCl_2), Sodium sulphate (Na_2SO_4), and Tris buffer] were procured from Sigma Aldrich, India. Cell culture media and its supplements were obtained from Gibco ThermoFisher

Scientific, India and Hi media, India. In addition, reagents and stains for biocompatibility and biofunctional assays were purchased from Sigma Aldrich, India. Silver nitrate was obtained from Spectrochem, India.

Fabrication of CC and CC-WE scaffold

The CC scaffold has been fabricated as per the optimized procedure reported recently, where the chitosan-collagen ratio has been optimized as 75:25 for favourable physico-chemical and mechanical characteristics [17]. In a typical procedure, chitosan and collagen in the ratio (w/w) of 75:25 was mixed thoroughly and allowed to stir for 3h. Subsequently, 25 mg of WE were added to 10 mL of polymer solution; bath sonicated for 60 min and lyophilized for 48h. The lyophilized sample was then cross-linked with a 4% (v/v) glyoxal solution followed by a repeated lyophilization procedure for another 48h to obtain the CC-WE scaffold. The CC scaffold without WE served as the control of the study. Finally, the as-obtained scaffold was cut into square pieces (2 mm × 2 mm) for further analyses.

Physico-chemical characterizations

The compositional evaluation of CC and CC-WE scaffolds was performed by ATR spectral analysis (PerkinElmer, UK), while surface morphology and microarchitecture analyses were carried out by Optical (Lawrence and Mayo, India) as well as Scanning Electron Microscopy (SEM; (JEOL Model, JSM-6390 LV, UK)).

In vitro swelling and degradation studies

Swelling and degradation of the scaffolds were conducted in phosphate-buffered saline (1X PBS, pH 7.4) under ambient conditions. Briefly, the dry weight of the scaffolds ($n = 3$) was recorded and then immersed in PBS solution (1X; pH 7.4) at 37°C. The medium was replenished every third day, and the weight of the scaffolds was measured at definite time intervals. The percentage of swelling was calculated as per equation (1). After 60 days of incubation, the scaffolds were dried at 37°C, and the percentage of degradation was calculated using equation (2).

$$\% \text{ Swelling} = [(w_1 - w_0)/w_0] \times 100 \quad (1)$$

(w_0 and w_1 are dry and wet weights of the scaffolds, respectively).

$$\% \text{ degradation} = [(w_i - w_f)/w_i] \times 100 \quad (2)$$

(w_i and w_f are the initial and final weights of the scaffolds, respectively).

In vitro mineralization in SBF

The CC and CC-WE scaffolds were immersed in SBF (1.5X; pH 7.4) for determining the biomimetic mineralization potential of the scaffolds, according to the procedure reported elsewhere [18]. The scaffolds in SBF were incubated at 37°C for 14 days. The medium (SBF) was refreshed every alternative day to maintain the ionic concentration and pH of the medium intact. On days 7 and 14, the scaffolds were carefully collected, washed with Milli Q water, and dried at 37°C overnight. The Au-sputtered scaffolds were subjected to SEM analysis to gather information on the nucleation of apatite and mineralization features. The CC scaffolds treated in the same way served as control.

MTT assay and Actin/DAPI staining

The biocompatibility of the scaffolds was evaluated using Human Osteosarcoma (HOS) cells (procured from NCCS, Pune, India) by MTT assay and Actin/DAPI staining. In brief, the HOS cells (1×10^4

cells/well) were cultured on the sterile scaffold ($n = 3$) and placed in a 24-well plate provided with standard culture media and conditions. After 24h of incubation, an MTT assay was performed, and the absorbance of formazan crystals dissolved in DMSO was measured at 570 nm using Spark® Multimode Microplate Reader (Tecan, Switzerland). The percentage viability of the cells on the scaffolds with respect to the control (cells without scaffolds) was calculated. For Actin/DAPI staining, the cells (1×10^4 cells/well) were seeded into a 24-well plate on the sterile scaffold and incubated for 24h under standard culture conditions. After incubation, the cells were fixed with 4% (w/v) paraformaldehyde solution for 20 min, and Alexa fluor-488 Phalloidin was added to stain the F-actin filaments of the fixed cells followed by counterstaining with 4'6 diamidino-2-phenylindole (DAPI). The stained cells were observed under a phase-contrast inverted fluorescence microscope (Nikon Eclipse Ti2 Series, India).

Alizarin red S and von Kossa staining

Alizarin red S (ARS) and von Kossa staining methods were adopted to determine the innate Calcium Phosphate mineralization potential of the CC and CC-WE scaffolds [19, 20]. The HOS cells (1×10^4 cells/well) were seeded onto the sterile scaffolds in 24 well culture plates and incubated for 7 days by following standard cell culture conditions. After 7 days of incubation, the cells were fixed with 4% (w/v) paraformaldehyde solution for 20 min. For ARS staining, the fixed cells were washed multiple times with sterile

water followed by ARS (40mM; pH 4.1) staining for 30 min under gentle shaking. The cells were carefully washed with water, and the red-coloured deposition of Ca nodules was observed using a phase-contrast inverted microscope (Nikon Eclipse Ti2 Series, India). In the von Kossa staining procedure, the fixed cells were washed with cacodylate buffer and incubated with 5% (w/v) silver nitrate solution under UV light for half an hour and finally added 5% (w/v) sodium thiosulphate. The brownish to black deposition of phosphate was captured using a phase-contrast inverted microscope.

Results and Discussions

Physico-chemical and morphological characterizations of the scaffolds

The photographic and optical microscopic images provide preliminary information on the physical features of the scaffolds. The porous architecture of CC and CC-WE scaffolds is visible from optical micrographs [figure 1A (a-b)]. The yellowish colour of CC scaffold [figure 1A(a) (inset)] is transformed to intensified brown colour for CC-WE scaffolds due to the presence of WE [figure 1A(b) (inset)]. The characteristic peaks of chitosan and collagen in the CC-WE scaffold are affirmed from the ATR spectrum [figure 1B]. More specifically, the broad peak at 3291 cm^{-1} exemplifies -NH stretching vibrations of CC. Peaks observed at 2941 cm^{-1} and 2864 cm^{-1} represent asymmetric and symmetric stretching vibrations of the $-\text{CH}_2$ group, while the presence of residual N-acetyl group

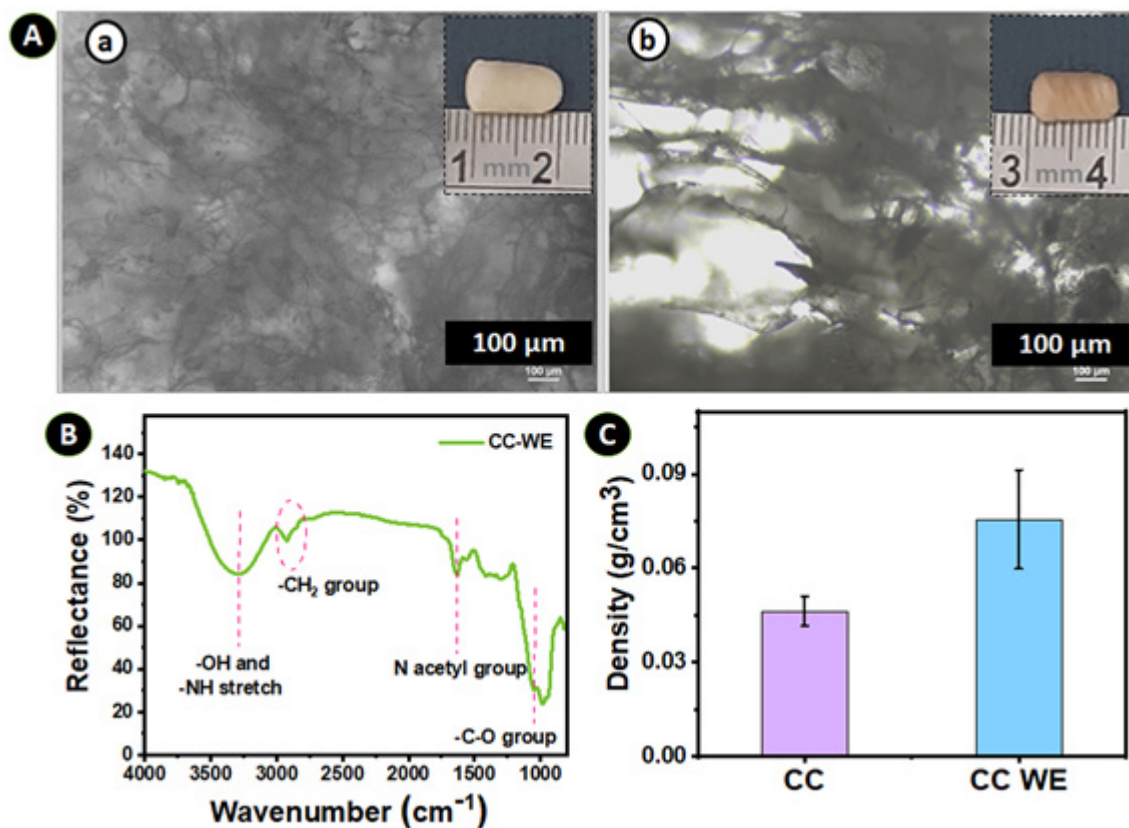


Figure 1: Physico-chemical characteristics and optical microscopic images of CC and CC-WE scaffolds, wherein A (a) and A (b) represent optical microscopic images of CC and CC-WE scaffold with photographs of the scaffolds as inset; (B) ATR spectrum and (C) density chart of CC and CC-WE scaffolds (all values are presented as mean \pm SD)

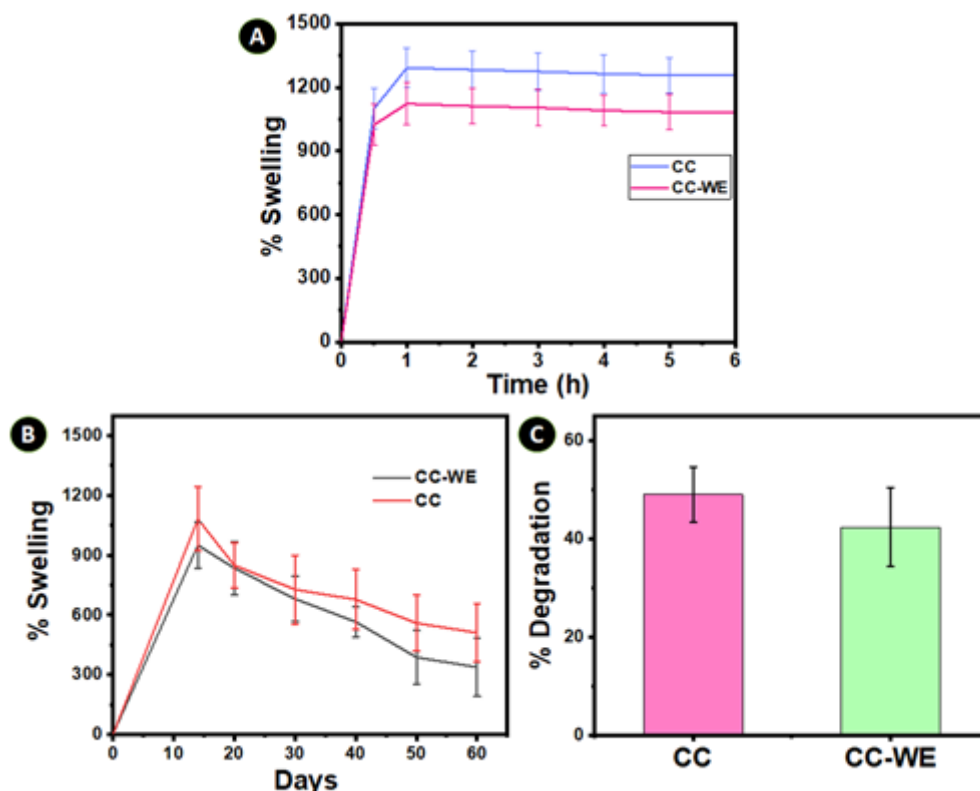


Figure 2: Swelling behavior of CC and CC-WE scaffolds after (A) short term and (B) long term incubation in PBS; (C) degradation kinetics of scaffolds. All values are presented as mean \pm SD.

was confirmed by the peak at 1645 cm^{-1} . Additionally, the peak responsible for $-\text{CO}$ stretching vibrations is noticed at 1035 cm^{-1} . Density measurement data [figure 1C] indicate an increment in density for CC-WE ($0.076 \pm 0.015\text{ g/cm}^3$) compared to CC scaffold ($0.046 \pm 0.005\text{ g/cm}^3$), which is contributed by the presence of WE.

Water absorption and Degradation of CC-WE scaffold

The swelling and degradation profile of the scaffolds were investigated in biomimetic physiological conditions (figure 2A and B). Maximum swelling of CC and CC-WE scaffolds was obtained within 1h of incubation [figure 2A] in the medium and from there onwards a plateau is maintained for 10 days [figure 2B]. Thereafter, a drop in mass is observed for the scaffolds and is correlated to the preliminary phase of degradation, and an average weight reduction of 49% was recorded for CC and 42.3% for CC-WE on day 60 [figure 2C]. The swelling profile supports the suitability of the scaffolds for tissue regeneration applications. Precisely, the hydrophilic nature of the CC and CC-WE scaffold is crucial for cellular infiltration through the supportive three-dimensional matrix as well as for nutrient and metabolites transfer [21]. Apart from this, the increase in pore size and surface area/volume ratio of the scaffolds, due to controlled degradation, provide a better environment for the cells to infuse, attach and thereby enhance proliferation and differentiation [22]. Furthermore, the slow degradation of these scaffolds would deliver adequate support to the tissue until the repair phase completes [23].

Both CC and CC-WE exhibited microporous structure with open and closed cells evident from the SEM images [figure 3 A (a-b)], where the pore size is in the range of 34.0 to $64.7\text{ }\mu\text{m}$ and 23.4 to

$64.4\text{ }\mu\text{m}$, respectively. The inter-connected microporous arrangement of the scaffolds together with surface roughness provides a better platform for cellular infiltration [22,24], which would facilitate the cell-matrix interaction and initiate appropriate signaling to promote cell growth and proliferation [25]. It is well-known that the surface roughness enhances the nucleation and growth of apatite crystals [26]. Further, the amino groups of chitosan reinforce the triple helical structure of the collagen while cross-linking via dialdehyde, donated by glyoxal, significantly enables matrix integrity [27]. The EDX spectra of the scaffolds provided in figure 3A inset confirm the elements present in the system.

Biomimetic mineralization of scaffolds in SBF

Biomimetic mineralization in SBF provides preliminary insight into the bone-bonding ability of a three-dimensional tissue engineering matrix [18, 28]. The coherent apatite nucleation is apparent in SBF treated CC and CC-WE scaffolds (SEM micrographs) on days 7 and 14 [figure 3B and C]. The primary nucleation on the matrix (day 7) validates early mineralization [figure 3C (a)]. The thick layer of nodule-like mineralization, predominantly on CC-WE (day 14), provides clear evidence for the progression of nucleation to a secondary level, confirming the inherent biomimetic mineralization potential of CC-WE [figure 3C (b-c)]. A similar trend, but to a lesser extent, has been observed for the CC scaffold [figure 3B (b-c)]. The early mineralization witnessed in the CC-WE scaffold can be attributed to the synergistic effect of the chitosan-collagen and bioactive phytoconstituents of the WE containing nucleation sites and subsequently accelerating the mineralization process [29,30].

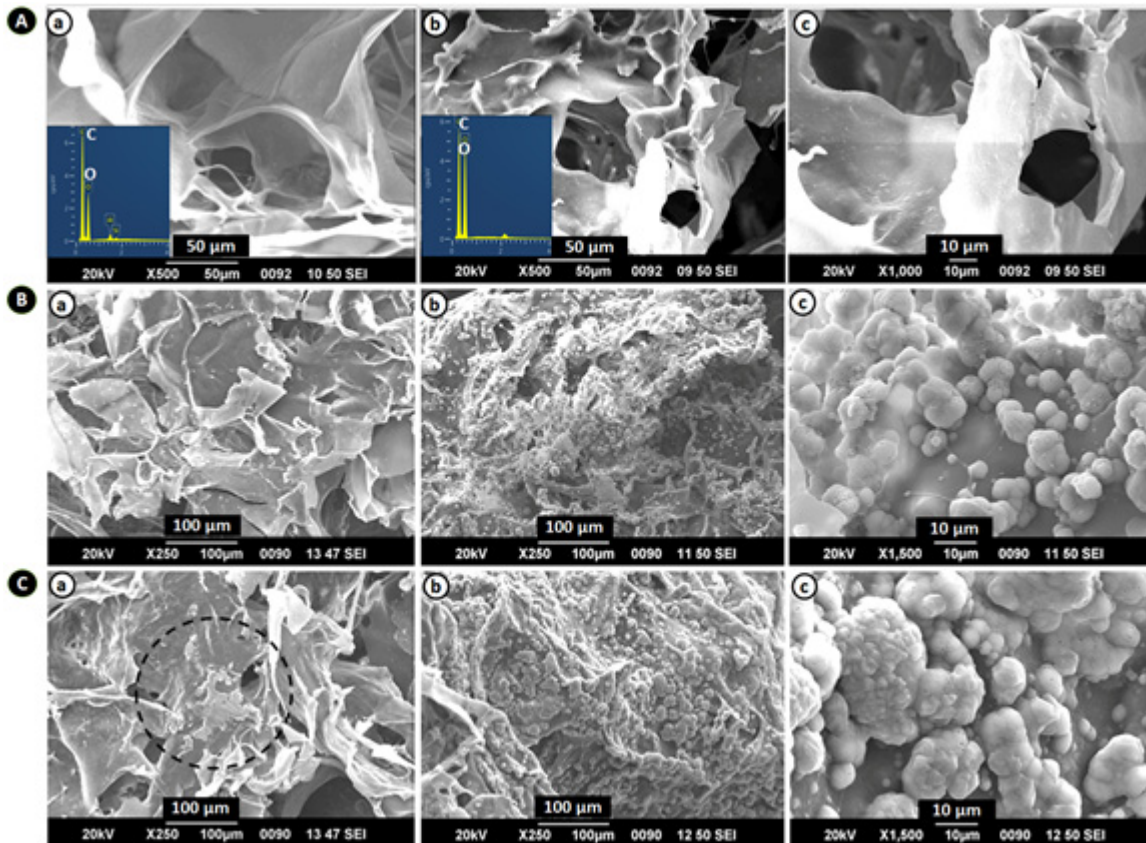


Figure 3: SEM images of the porous microarchitecture and biomimetic mineralization of CC and CC-WE scaffolds: Fig A (a) represents SEM images of the CC scaffold, A (b-c) represent the CC-WE scaffold at two different magnifications. Inset illustrates corresponding EDX spectrum. B(a) and C (a) represent SEM images of CC and CC-WE after 7 days of incubation in SBF, whereas B (b-c) and C (b-c) represent SEM images of CC and CC-WE scaffolds after 14 days of incubation at two different magnifications.

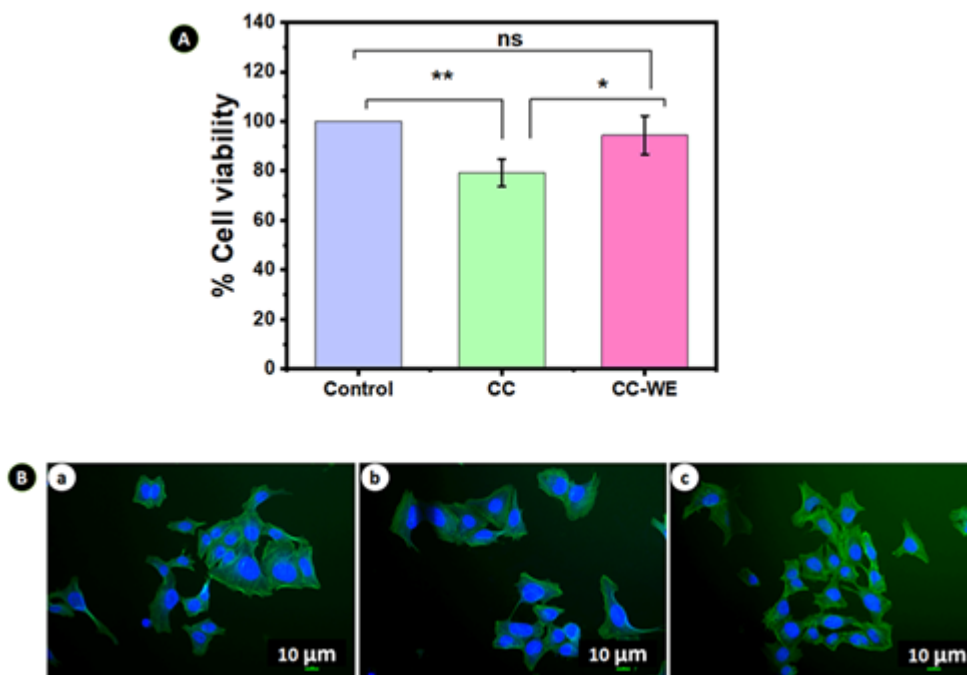


Figure 4: Cytocompatibility of CC and CC-WE scaffolds by (A) MTT assay and (B) Actin/DAPI staining [B(a-c) represent the control (no scaffold), CC and CC-WE respectively]. *Note:* Values are presented as mean \pm SD. 'ns' indicates non-significance with $p > 0.05$; * and ** indicate statistical significance with p -value < 0.05 and < 0.01 , respectively.

Cytocompatibility evaluation of CC and CC-WE scaffold

The viability and morphological architecture of the cells demonstrated by MTT assay and F-actin/DAPI staining affirmed cytocompatibility of the CC-WE scaffold [figure 4]. The viability data from the MTT assay is presented as percentage cell viability in figure 4A, demonstrating CC-WE for a significantly high viability index ($94.5\% \pm 7.7$), which is comparable to that of the control (untreated; no scaffold) cells, inferring the presence of metabolically active cells. Corroborative findings were noticed from Actin/DAPI staining as well [figure 4B]. The cells exhibited typical normal F-actin cytoskeleton morphology, indicating cytocompatibility of the scaffolds. Further supportive evidence was obtained from DAPI stained nuclei, where the nuclei remain intact analogous to the control cells after the cell-scaffold interactions. The elevated cytocompatibility of CC-WE originated from the synergistic effect of bioactive phytocomponents in the aqueous extract of CQ bound to the microporous CC scaffold presenting abundant availability of these components to interact with the cells and thereby, providing an adequate cellular microenvironment for adhesion and proliferation of the cells.

Biom mineralization of CC-WE scaffolds

In general, an efficient bone tissue engineering scaffold should be capable of eliciting extracellular biomineralization while in contact with the cells [30]. The biomineralization potential of the scaffolds assessed by ARS and von Kossa staining following 7 days of cell-scaffold interaction is illustrated in figure 5. The ARS forms a red-colored complex with Ca nodules, while von Kossa staining produces a brownish to the black-colored product upon reaction with phosphate groups [19, 20], suggestive of biomineralization. An appreciable amount of red-colored Ca-ARS adduct was evident in the CC-WE scaffold [Fig. 5A(c)] and the cells incubated with CC scaffolds also showed Ca nodule formation, but less intense than

CC-WE [figure 5 A (b)]. Further, a higher degree of brownish-black deposition in CC-WE than CC after von Kossa staining portrays the cell-scaffold interaction triggered intense mineralization [figure 5 B]. The above observations clearly describe the innate capability of the CC-WE to persuade biomineralization, a remarkable feature of bone tissue regeneration.

The integration of WE to the natural CC scaffold refined the tissue regeneration behavior of the scaffold system by exploring the defined osteogenic potential of the individual components. As-fabricated CC-WE scaffold with well-distributed interconnected pores augmented the early biomimetic mineralization with added benefits on controlled degradation profile in the physiological condition, illustrating its suitability for bone tissue regeneration. Besides active components, the compatible cellular response due to suitable functional group, surface characteristics and morphological microarchitecture facilitated a better scaffold-cell interface subsequently invoked significant biomineralization.

Conclusions

Recent decades witnessed a notable advancement in translational medicine, where traditional medicinal plants related knowledge are scientifically transformed into an established strategy with greater therapeutic potential. The present study demonstrates solid evidences of the early biomineralization potential of the aqueous CQ stem extract (WE) integrated chitosan-collagen hybrid scaffold. The porous micro-architecture and other surface features together with controlled degradation profile transformed the entire system (CC-WE) as an appropriate matrix, consequently facilitating better interaction with the cells, and thereby, augmented the aggregation of Ca-P minerals, a remarkable event of osteogenesis. Altogether, the CC-WE scaffold delivers a favorable microenvironment to promote a forthcoming platform for bone tissue regeneration applications.

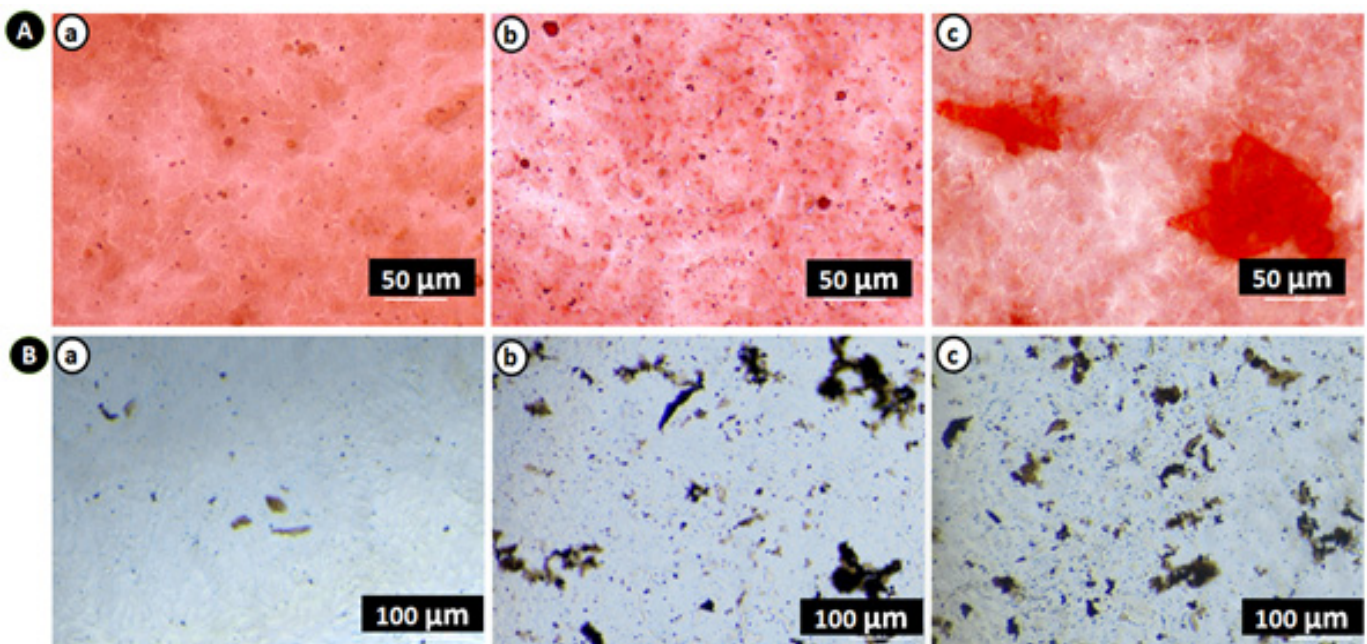


Figure 5: Early biomineralization of the scaffolds. A (a-c) represent ARS-stained images of the control (no scaffolds), CC, and CC-WE respectively. B (a-c) denote the control (no scaffolds), CC, and CC-WE, respectively, after von Kossa staining.

Acknowledgements

Praseetha R. Nair gratefully acknowledges the Kerala State Council for Science, Technology and Environment (KSCSTE -WSD Back to Lab scheme), Kerala, for the financial support of this work. The authors are very much grateful to the Department of Biotechnology, CUSAT for providing their cell culture facility.

References

1. J.Y. Park, S.H. Park, M.G. Kim, S.H. Park, T.H. Yoo, M.S. Kim, Biomimetic Scaffolds for Bone Tissue Engineering, *Adv. Exp. Med. Biol.*, 1064, 109–121 (2018).
2. L.P. Corrales, M.L. Esteves, J.A. E. Vick, Scaffold Design for Bone Regeneration, *J. Nanosci. Nanotechnol.*, 14 (1), 15–56 (2014).
3. H. Ehrlich, Chitin and Collagen as Universal and Alternative Templates in Biomineralization, 52, 661–699 (2010).
4. L. Yu, M. Wei, Biomineralization of Collagen-Based Materials for Hard Tissue Repair. *Int. J. Mol. Sci.*, 22 (2), 1–17 (2021).
5. J. Wang, C. Liu, Biomimetic Collagen/Hydroxyapatite Composite Scaffolds: Fabrication and Characterizations. *J. Bionic Eng.*, 11 (4), 600–609. (2014).
6. D. Zhang, X. Wu, J. Chen, K. Lin, The Development of Collagen Based Composite Scaffolds for Bone Regeneration. *Bioact. Mater.*, 3 (1), 129–138 (2018).
7. A. Martínez, M.D. Blanco, N. Davidenko, R.E. Cameron, Tailoring Chitosan/Collagen Scaffolds for Tissue Engineering: Effect of Composition and Different Crosslinking Agents on Scaffold Properties. *Carbohydr. Polym.*, 132, 606–619 (2015).
8. F. Croisier, C. Jérôme, Chitosan-Based Biomaterials for Tissue Engineering. *Eur. Polym. J.*, 49 (4), 780–792 (2013).
9. I.V. Yannas, D.S. Tzeranis, B.A. Harley, P. T. C. So, Biologically Active Collagen-Based Scaffolds: Advances in Processing and Characterization. *Philos. Trans. R. Soc. A Math. Phys. Eng. Sci.*, 368 2123–2139 (2010).
10. C.G. Knight, L.F. Morton, A.R. Peachey, D.S. Tuckwell, R.W. Farndale, M.J. Barnes, The Collagen-Binding α -Domains of Integrins $\alpha 1/\alpha 1$ and $\alpha 2/\alpha 1$ Recognize the Same Specific Amino Acid Sequence, GFOGER, in Native (Triple- Helical) Collagens. *J. Biol. Chem.*, 275 (1), 35–40 (2000).
11. U. Anand, N. Jacobo-Herrera, A. Altemimi, N. Lakhssassi, A Comprehensive Review on Medicinal Plants as Antimicrobial Therapeutics: Potential Avenues of Biocompatible Drug Discovery. *Metabolites*, 9 (11), 1–13. (2019).
12. S. Siddiqui, E. Ahmad, M. Gupta, V. Rawat, N. Shivnath, M. Banerjee, M. S. Khan, M. Arshad, *Cissus Quadrangularis* Linn Exerts Dose-Dependent Biphasic Effects: Osteogenic and Anti-Proliferative, through Modulating ROS, Cell Cycle and Runx2 Gene Expression in Primary Rat Osteoblasts. *Cell Prolif.*, 48 (4), 443–454 (2015).
13. A. Shirwaikar, S. Khan, S. Malini, Antiosteoporotic Effect of Ethanol Extract of *Cissus Quadrangularis* Linn. on Ovariectomized Rat. *J. Ethnopharmacol.*, 89 (2–3), 245–250 (2003).
14. B.K. Potu, M.S. Rao, N.G. Kutty, K.M.R. Bhat, M.R. Chamallamudi, S.R. Nayak, Petroleum Ether Extract of *Cissus Quadrangularis* (Linn) Stimulates the Growth of Fetal Bone during Intra Uterine Developmental Period: A Morphometric Analysis. *Clinics*, 63 (6), 815–820 (2008).
15. R.H. Toor, S. Malik, H. Qamar, F. Batool, M. Tariq, Z. Nasir, R. Tassaduq, J.B. Lian, J.L. Stein, G.S. Stein, et al. Osteogenic Potential of Hexane and Dichloromethane Fraction of *Cissus Quadrangularis* on Murine Preosteoblast Cell Line MC3T3-E1 (Subclone 4). *J. Cell. Physiol.*, 234 (12), 23082–23096 (2019).
16. P.R. Nair, S. Sreeja, G.S. Sailaja, In Vitro Biomineralization and Osteogenesis of *Cissus Quadrangularis* Stem Extracts/: An Osteogenic Regulator for Bone Tissue Engineering. *J. of Biosci.*, 46:88 (2021).
17. P.R. Nair, S. Sreeja, G.S. Sailaja, Early Biomineralizing Chitosan–Collagen Hybrid Scaffold with *Cissus Quadrangularis* Extract for Regenerative Bone Tissue Engineering, *New J. Chem.*, 45 (42), 19733–19745, (2021).
18. T. Kokubo and Hiroaki. How Useful Is SBF in Predicting in Vivo Bone Bioactivity/? *J. Biomaterials*, 27, 2907–2915. (2006).
19. C.A. Gregory, W.G. Gunn, A. Peister, D.J. Prockop, An Alizarin Red-Based Assay of Mineralization by Adherent Cells in Culture/: Comparison with Cetylpyridinium Chloride Extraction. *Anal. Biochem.*, 329, 77–84,(2004).
20. G.S. Sailaja, K. Sreenivasan, Y. Yokogawa, T.V. Kumary, H.K. Varma, Bioinspired Mineralization and Cell Adhesion on Surface Functionalized Poly(Vinyl Alcohol) Films. *Acta Biomater.*, 5 (5), 1647–1655. (2009).
21. J. Li, H. Sun, D. Sun, Y. Yao, F. Yao, K. Yao, Biomimetic Multicomponent Polysaccharide/Nano-Hydroxyapatite Composites for Bone Tissue Engineering. *Carbohydr. Polym.*, 85 (4), 885–894 (2011).
22. C.M. Murphy, M.G. Haugh, F.J.O'Brien, The Effect of Mean Pore Size on Cell Attachment, Proliferation and Migration in Collagen-Glycosaminoglycan Scaffolds for Bone Tissue Engineering. *Biomaterials*, 31 (3), 461–466 (2010).
23. S. H. Park, E. S. Gil, H. Shib, H. J. Kima, K. Leeb, Relationships Between Degradability of Silk Scaffolds and Osteogenesis. *Bone*, 23 (1), 1–7 (2008).
24. A. Zareidoost, M. Yousefpour, The Relationship of Surface Roughness and Cell Response of Chemical Surface Modification of Titanium. *J Mater Sci Mater Med*, 23 (6), 1479–1488 (2012).
25. A.J. Engler, S. Sen, H.L. Sweeney, D.E. Discher, Matrix Elasticity Directs Stem Cell Lineage Specification., 677–689 (2006).
26. A. Arvidsson, F. Currie, P. Kjellin, Y.T. Sul, V. Stenport, Nucleation and Growth of Calcium Phosphates in the Presence of Fibrinogen on Titanium Implants with Four Potentially Bioactive Surface Preparations. An in Vitro Study. *J. Mater. Sci. Mater. Med.*, 20 (9), 1869–1879 (2009).
27. L.L. Fernandes, C.X. Resende, D.S. Tavares, G.A. Soares, L.O. Castro, J.M. Granjeiro, Cytocompatibility of Chitosan and Collagen-Chitosan Scaffolds for Tissue Engineering. *Polimeros*, 21 (1), 1–6 (2011).
28. S. Sreeja, C.V. Muraleedharan, P.R.H.K. Varma, G.S. Sailaja, Surface-Transformed Osteoinductive Polyethylene Terephthalate Scaffold as a Dual System for Bone Tissue Regeneration with Localized Antibiotic Delivery. *Mater. Sci. Eng. C*, 109, 110491 (2020).
29. H. Liu, H. Yazici, C. Ergun, T.J. Webster, H. Bermek, An in vitro Evaluation of the Ca/P Ratio for the Cytocompatibility of Nano-to-Micron Particulate Calcium Phosphates for Bone Regeneration. *Acta Biomater.*, 4 (5), 1472–1479 (2008).
30. S. Talebian, M. Mehrali, S. Mohan, B.H.R. Raghavendran, M. Mehrali, H. M. Khanlou, T. Kamarul, A.M. Afifi, A.A. Abass, Chitosan (PEO)/Bioactive Glass Hybrid Nanofibers for Bone Tissue Engineering. *RSC Adv.*, 4 (90), 49144–49152. (2014).



Original Article

Stress Analysis During Occlusal Loading in a Human Skull with Maxillary Defect: A Finite Element Study

Varadaraju Magesh,¹ Pandurangan Harikrishnan,^{2,3*} Arayambath Balamani,⁴ Elumalai Canmany⁴, Akash Kasatwar,⁵ Ramamurthy Suresh⁶

¹Department of Mechanical Engineering, College of Engineering and Technology, SRM Institute of Science and Technology, Kattankulathur 603203, Tamil Nadu, India

²Department of Orthodontics, Faculty of Dental Sciences, SGT University, Gurugram 1224505, Haryana, India

³Craniofacial Orthodontist, Teeth “N” Jaws Center, Lake Area, Nungambakkam, Chennai 600034, Tamilnadu, India

⁴Department of Orthodontics, Mahatma Gandhi PG Institute of Dental Sciences, Puducherry 605006, India

⁵Department of Dentistry, Government Hospital, Ballarpur, Chandrapur 442701, Maharashtra, India

⁶Department of Dental Surgery, Thanjavur Medical College and Hospital, Thanjavur 613004, Tamilnadu, India

Received: 22 July 2022
Accepted: 22 August 2022
Published online: 30 June 2023

Keywords: human skull, maxillary defect, maxillectomy, skull defect, FEA, stress distribution, occlusal loading

Human skull is designed to absorb the stress from the chewing forces and trauma to the head region. Teeth transfers the chewing forces to the maxilla and mandible and then to the skull bones. In this study, a skull with a maxillary defect due to surgical treatment of mucormycosis is evaluated for stress distribution from occlusal loading. Finite element model is constructed from a CBCT of an adult male patient with maxillectomy defect. Bilateral occlusal loading was done in the remaining posterior teeth in the asymmetrically present maxillary arch. Stress distribution is visualised and quantified both in frontal and lateral skull views. Results showed more stress on the left side than the right side and varied stress trajectories. Thus, we conclude that reconstruction of the maxillary defect is vital to gain proper morphology and symmetric stress distribution to maintain a functionally healthier craniofacial skeleton.

© (2023) Society for Biomaterials & Artificial Organs #20064423

Introduction

In a human skull, normal stress trajectories are followed during occlusal loading while chewing which distributes the stress from the jaws to the skull [1]. It varies in skull with defects and in cleft skull as shown in the literature [2]. So, it is obvious that a skull with a defect is prone to have variations in stress distribution. Mucormycosis (black fungus) is an acute opportunistic infection caused by a saprophytic fungus found in soil, bread molds, and decaying fruits and vegetables. Predisposing risk factors are poorly controlled diabetics, immunocompromised patients, hematologic malignancies and more recently in post-covid diabetics [3-5]. As mucormycosis is destructive and fast spreadin, the mainline of management is the surgical removal of the affected tissues and debridement. This leads to mutilating defects in the facial region [6].

Maxillectomy is a common surgical procedure where partial or subtotal or complete maxilla is removed due to reasons like malignancies, infections etc. The created defect has to be filled for

cosmetic and functional causes. Obturators are a commonly used option to reconstruct the maxilla which fullfils the cosmetic but not the strength part [7]. Surgically reconstructed maxilla should behave like a normal maxilla and transfer the chewing forces accordingly. Finite element (FE) analysis is a useful tool for simulation analysis of stress distribution in engineering and widely used for skull analysis due to the complexity of the experimentation [8-9]. So, we considered a real-time patient's maxillectomy skull defect model for FE analysis to study the stress distribution pattern.

Materials and methods

A CBCT scan of a 26 years old male patient, with a history of post-Covid mucormycosis who had maxillectomy of the whole anterior maxilla removed upto the 2nd premolar on the right and upto 1st premolar on the left was used for this study. Institutional research review committee approval was taken for the study.

The CBCT had slice increments of 0.3 mm and pixel size of 0.3 mm upto 122 slices. Image reconstruction tool MIMICS (Materialise Inc., Leuven, Belgium) was used for the model generation and thresholding was done after every slice such that we can take only part of the anatomical model for analysis. The

* Corresponding author
E-mail address: teethujaws@gmail.com (Dr. Pandurangan Harikrishnan)

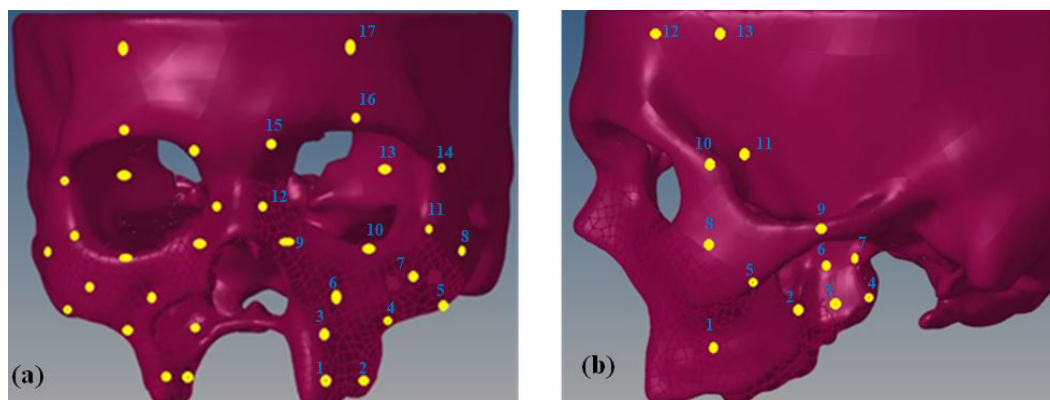


Figure 1: Skull Model (a) Frontal view and (b) Lateral view of the skull showing the points marked for measurement of stress distribution

teeth along with the whole skull of the patient was modelled excluding the mandible to visualise the lateral parts of the skull. Maxilla is considered as cancellous and the remaining portion of the skull as cortical. To avoid complications during the analysis, the image processing was done properly.

The CT data arrived as points and the surface modeling was generated using the Geomagic Design software (Geomagic Inc., Raleigh, North Carolina, USA). The required surface model was done by smoothening of the surface of the skull. The surface model was exported for the construction of the FE model in Hypermesh software (Altair Engineering, Troy, Michigan, USA). The 2D mesh was created with four noded tetrahedral elements. Later, the 3D mesh was created using solid 185 elements which are more suitable for structural analysis. In the Hypermesh software, the cancellous, cortical and tooth were filtered separately to enable the material properties during analysis [10]. The meshed model was exported to ANSYS R18.2 (ANSYS, Inc., Southfield, Michigan, USA) for analysis.

The material properties were assigned as follows: cancellous bone Young's modulus: 7900 MPa, cortical bone: 13,400 MPa and teeth 19,600 MPa. The Poisson ratio of 0.3 was taken for entire model [11]. A total force of 200 N was applied vertically towards the occlusal plane on the available teeth in the maxilla on each side. The boundary conditions are along the tangential passing through the anterior most point of foramen magnum and the pterion region arresting all degrees of freedom on the back of the skull. Static, linear structural analysis was carried out. The Von Mises stress distributions on the skull model were noted in the selected points in the frontal and lateral view of the skull (left and right side) as shown in figure 1.

Results

The points marked to capture the stress distribution in the frontal and lateral views of the maxillary defect skull model are shown in figures 1a and b. The stress distributions in the frontal and lateral views of the skull for 200 N occlusal force applied on both sides of the jaw are shown in figures 2a and b. The stress values in the marked points in both frontal and lateral views are shown in tables 1 and 2 respectively.

Table 1: Stress values in the Frontal region of the Skull (L-Left & R- Right side points)

Point	Name	Stress (MPa)	Point	Stress (MPa)
L1	Premolar region	0.972	R1	2.820
L2	Molar region	2.142	R2	1.192
L3	Posterior alveolar process	1.849	R3	0.876
L4	Maxillary buttress	2.531	R4	0.049
L5	Zygomatico-maxillary junction-Inferior	2.003	R5	0.454
L6	Mid-Maxilla	1.986	R6	0.430
L7	Zygomatico-maxillary junction-Mid	2.277	R7	0.331
L8	Zygomatic bone	0.107	R8	0.020
L9	Naso-maxillary junction	2.492	R9	0.548
L10	Zygomatico-maxillary junction-superior	0.236	R10	0.959
L11	Lateral orbital rim	1.593	R11	0.306
L12	Nasal bone	0.748	R12	0.469
L13	Sphenoid-Greater wing-Medial	0.593	R13	0.605
L14	Zygomatico-frontal junction	0.696	R14	0.782
L15	Fronto-Nasal process	0.227	R15	0.667
L16	Supra-Orbital rim	0.415	R16	0.236
L17	Frontal bone	0.361	R17	0.403

Table 2: Stress values in the Lateral region of the Skull (L-Left & R- Right side points)

Point	Name	Stress (MPa)	Point	Stress (MPa)
L1	Molar Alveolar process	1.895	R1	2.170
L2	Pterygomaxillary junction	0.694	R2	0.897
L3	Antero-inferior lateral pterygoid	1.591	R3	0.328
L4	Postero-inferior lateral pterygoid	0.362	R4	0.163
L5	Inferior zygoma	2.277	R5	2.819
L6	Antero-superior Lateral pterygoid	0.489	R6	1.464
L7	Postero-superior lateral pterygoid	0.335	R7	0.236
L8	Mid-zygoma	0.828	R8	1.337
L9	Zygomatic arch	0.359	R9	0.229
L10	Upper-zygoma	0.682	R10	0.232
L11	Greater wing of Sphenoid-inferior	1.084	R11	0.374
L12	Frontal bone	0.225	R12	0.570
L13	Parietal bone	0.440	R13	0.281

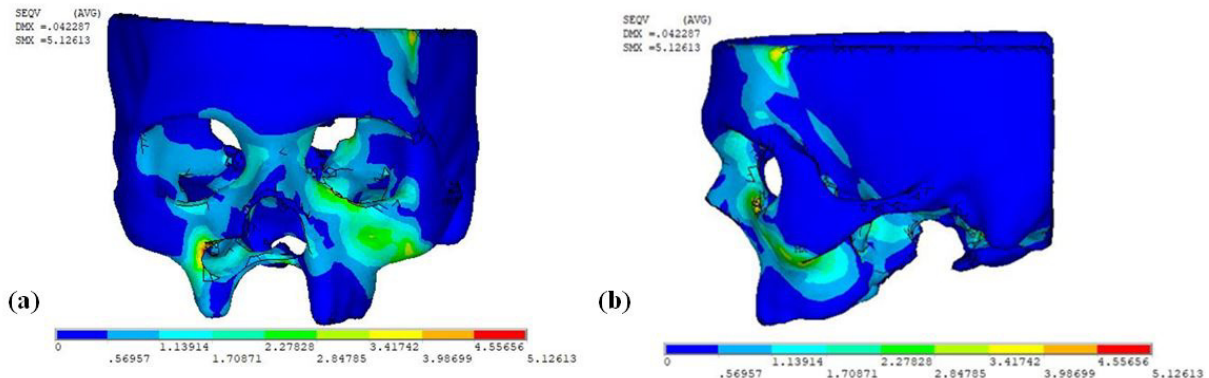


Figure 2: Stress distribution for 200 N occlusal loading on each side (a) Frontal view and (b) Lateral view of the skull

The stress distributed in the craniofacial region on occlusal load of 200 N each side was recorded. In this model, more teeth were present in the left side than the right side and collectively 200N was applied on each side teeth. Maxillary buttress and inferior zygoma regions in the left side recorded maximum stress as 2.531 and 2.277 MPa respectively. Highest stress on the right side were recorded in the premolar and inferior zygoma regions as 2.820 and 2.819 MPa. Lowest stresses on the left side were in the zygomatic bone and frontal bones as 0.107 and 0.225 MPa, and on the right side in the maxillary buttress and postero-inferior lateral pterygoid regions as 0.049 and 0.163 MPa respectively.

Discussion

Maxillectomies are one of commonly done surgical procedures due to various etiologies as mentioned before. It is important to restore the resected part of the maxilla by grafting or by artificial means like the obturator to restore the morphology and function. Till the restoration of the defect, patients eat with the remaining teeth and the chewing forces are transferred to the skull bones which might be highly varied due to the asymmetric anatomy between the right and the left side due to the defect. Results from this study clearly indicate this asymmetric stress distribution between each side as the maxillary buttress and inferior zygoma regions in the left side recorded maximum forces as 2.531 and 2.277 MPa respectively. Meanwhile, highest forces on the right side were recorded in the premolar and inferior zygoma regions as 2.820 and 2.819 MPa.

Large stress variations were seen between the left and right side in the maxillary molar region, posterior alveolar process, maxillary buttress, zygomatico-maxillary junction-inferior, mid-maxilla, mid-zygomatico-maxillary junction, naso-maxillary junction, lateral orbital rim, antero-inferior lateral pterygoid and greater wing of sphenoid regions as shown in Figure 2. The left side stresses were twice higher than the right side. This clearly demonstrates that there is a deviation of stress trajectories between the sides in this anatomically asymmetric situation. It is shown that symmetric normal skull models show a uniform stress distribution and unilateral cleft defect skull models have shown asymmetric stress distribution because of the defect [2]. But higher stress values were found in the right side in premolar region, zygomatico-maxillary junction-superior, fronto-nasal process, molar alveolar process, inferior zygoma, antero-superior lateral pterygoid and frontal bone regions. Even in the right side there are less number of teeth for occlusal loading, for the same loading forces, the stress

in the mentioned areas are more than the left side side.

Our findings showed that the asymmetric anatomy transferring the forces deviated from the normal trajectories. Almost similar stress were found in both left and right side in medial part of greater wing of sphenoid, zygomatico-frontal junction, postero-superior lateral pterygoid plate and zygomatic arch regions. Interestingly, this shows that as the forces transfer to the superior part of the orbital and the posterior part of the lateral pterygoid plate regions, it reaches similar stress values. Thus, even the forces travel asymmetrically on each side it is dissipated terminally similar to each other. The asymmetric stress leads to asymmetric strain leading to vertical plane bending in the medial infra-orbital rim and nasal bone regions as also reported in the literature [12].

It is important to note that in our model the absence of maxilla upto premolar region eliminates the frontal and canine pillars of stress trajectories. All our occlusal loading travelled through the pterygoid and zygomatic pillars on both sides, but travels to the nasal bones and medial orbital rims anteriorly due to the resistance from the superior skull bones which are more cortical in nature. It was reported that while occlusal loading of molars, the stresses were transferred predominantly through the infrazygomatic crest [13]. Such maxillary defect puts excess asymmetric stress on the pterygoid and zygomatic pillars which can cause bone damage and dehiscence and fenestration in the teeth regions [14].

Our FE findings clearly showed that the anatomical defect leads to skeletal asymmetry which leads to the asymmetric stress distribution for similar occlusal loading as the forces travel towards the skull. The muscles attached to the jaws play an important role in chewing mechanism and the force distribution, which is not modelled and thus a limitation of this study.

Conclusion

Our FE study on a skull with maxillary skeletal defect skull showed asymmetric stress distribution during simulated occlusal loading of the teeth on each side of the maxilla. Thus, symmetric reconstructions of maxillary defects at the earliest are vital in regaining the normal stress distribution in restoring the functional health of the craniofacial skeleton.

References

- Alexandridis C, Caputo AA, Thanos CE. Distribution of stress in the human skull. *J Oral Rehabil*, 12, 499-507 (1982).

2. Harikrishnan P, Balakumaran. Analysis of Stress Trajectories in Human Adult Cleft Skull. *J Craniofac Surg*, 28(6):1552-1553 (2017).
3. Sun HY, Singh N. Mucormycosis: its contemporary face and management strategies. *Lancet Infect Dis*, 11(4):301-11 (2011).
4. Jones AC, Bentsen TY, Freedman PD. Mucormycosis of the oral cavity. *Oral Surg Oral Med Oral Pathol*, 75(4):455-60 (1993).
5. Rao V, Arakeri G, Madikeri G, Shah A, Oeppen R, Brennan P. Post-COVID Mucormycosis in India: A formidable challenge. *Br J Oral Maxillofac Surg*, 59(9):1095-1098 (2021).
6. Rapidis AD. Orbitomaxillary mucormycosis (zygomycosis) and the surgical approach to treatment: perspectives from a maxillofacial surgeon. *Clin Microbiol Infect*, 15 (Suppl 5): 98–102 (2009).
7. Kortés J, Dehnad H, Kotte ANT, Fennis WMM, Rosenberg AJWP. A novel digital workflow to manufacture personalized three-dimensional-printed hollow surgical obturators after maxillectomy. *Int J Oral Maxillofacial surg*, 47(9): 1214-1218 (2018).
8. Jose G, Somer N, George Y. Finite element analysis of human skull bone adaptation to mechanical loading, *Comput Methods Biomech Biomed Engin* 24(7): 753-764 (2021).
9. Pierre H, Guillaume D, Patrick G, Thomas S. Comparative finite element analysis of skull mechanical properties following parietal bone graft harvesting in adults. *J Craniomaxillofac Surg*, 46(2):2018, 329-337.
10. Janovic A, Saveljic I, Vukicevic A, Nikolic D, Rakocevic Z, Jovicic G, Filipovic N, Djuric M. Occlusal load distribution through the cortical and trabecular bone of the human mid-facial skeleton in natural dentition: a three-dimensional finite element study. *Ann Anat*, 197:16-23 (2015).
11. Choi DS, Cha BK, Jang I, Kang KH, Kim SC. Three-dimensional finite element analysis of occlusal stress distribution in the human skull with premolar extraction. *The Angle Orthodontist*, 83(2):204–211 (2013).
12. Gross MD, Arbel G, Hershkovitz I. Three-dimensional finite element analysis of the facial skeleton on simulated occlusal loading. *J Oral Rehabil*, 28(7):684-94 (2001).
13. Cattaneo PM, Dalstra M, Melsen B. The transfer of occlusal forces through the maxillary molars: a finite element study. *Am J Orthod Dentofacial Orthop*, 123(4):367-73 (2003).
14. Sana S, Kondody RT, Talapaneni AK, Fatima A, Bangi SL. Occlusal stress distribution in the human skull with permanent maxillary first molar extraction: A 3-dimensional finite element study, *Am J Orthod Dentofacial Orthop* 160(4): 552-559 (2021).



Original Article

Differential Surface Thrombogenicity of Heparin Coated Bovine Pericardium: Implication in Bioprosthetic Valve Fabrication

Sachin J. Shenoy¹, S.L. Devika¹, Vivek V. Pillai², G. Maneesha¹, P.R. Umashankar^{1*}, G. Ranjith³

¹Department of Applied Biology, ²Department of Cardiovascular and Thoracic surgery, ³Department of Medical Device Engineering, Sree Chitra Tirunal Institute of Medical Sciences and Technology, Thiruvananthapuram, India

Received: 9 December 2022
Accepted: 25 December 2022
Published online: 30 June 2023

Keywords: bovine pericardium, heparin coating, rough and smooth surface, thrombogenicity, bioprosthetic heart valve

Sub-acute valve thrombosis limits the full potential of bovine pericardial valves. In this study, the effect of heparin coating and the influence of rough versus smooth pericardial surface on thrombogenicity was evaluated by *in vitro* methods. This was followed by mitral implantation of bioprosthetic valves with different inflow surfaces in sheep. The presence of conjugated heparin was demonstrated through O-toluidine blue staining and micro Raman spectroscopy. Heparin was estimated by a colorimetric assay for depletion of O-toluidine blue stain following exposure to heparin modified tissue. Functionality of surface bound heparin was demonstrated by platelet adhesion and protein adsorption studies. Difference in surface thrombogenicity of heparin coated rough and smooth surface was evaluated by modified whole blood kinetic clotting time method. Bioprosthetic valves with either rough or smooth surface of heparin coated pericardium forming the inflow surface were implanted in the mitral position of sheep and observed for device thrombosis upto 6 months. Heparin coating rendered the pericardial surface hydrophilic. Adsorbed protein on heparin coated pericardium was less compared to non-coated one. SEM images for platelet adhesion showed absence of platelets on heparin-coated tissue. Surface thrombogenicity evaluation showed difference in thromboresistance for heparin coated and uncoated pericardial surfaces and between heparin coated rough/smooth surfaces. Sheep implanted with valve having heparin coated rough surface as valve inflow thrombosed in 53 days. In comparison, the valve having heparin coated smooth surface of pericardium forming the valve inflow surface completed the observation period of 6 and 12 months without any valve thrombosis.

© (2023) Society for Biomaterials & Artificial Organs #20066423

Introduction

Biological heart valves can be homograft or allograft when it is of human origin [1-5] or it can be made from chemically processed animal tissues [6,7]. Bioprosthetic heart valves (BHV) are made from glutaraldehyde processed animal tissues such as porcine aortic valve or bovine pericardium with supporting fabric covered stents or without it. Glutaraldehyde cross-linked bovine pericardia is widely used in the fabrication of BHV since 1970s [8] and have evolved through various pericardial post processing techniques to make it more conducive for clinical application. One of the major benefits of BHV over mechanical valve is the decreased dependency on anticoagulant therapy [9]. However, unlike its mechanical counterpart, both transcatheter and surgical BHV have been reported to fail on account of calcific structural degradation and

thrombosis [10-12] thus limiting its durability [1]. For any blood-contacting device, clot formation can result in dysfunction leading to device failure, or alternatively it may release emboli into the systemic circulation causing fatal thromboembolism of distal organs [13]. Occurrence of subclinical leaflet thrombosis in transcatheter heart valves (THVs) is found to range between 7 and 35% [5]. Although, the long established glutaraldehyde process is known to mask most of the cellular antigens present on the collagenous tissue, its residual immunogenicity and consequent chronic inflammation is still found to be associated with long term failure including valve thrombosis [14,15]. Glutaraldehyde treated pericardial surface is known to be hydrophobic and vulnerable to surface fibrinogen binding [16]. In conclusion, *in vivo* calcification and valve thrombosis has since remained elusive factors limiting the potential durability of glutaraldehyde processed bovine pericardial valve [17-19]. Surface immobilization of heparin is known to induce thromboresistance and even temporary immobilization of heparin to biomaterial surfaces has previously

* Corresponding author
E-mail address: umashnkr@scimst.ac.in (Dr. P.R. Umashankar, PhD)

shown to reduce thrombus formation on implanted blood contacting devices [20-22].

The present study demonstrates thromboresistance induced by surface immobilized heparin on glutaraldehyde processed bovine pericardium by way of resistance to platelet adhesion and reduced surface protein adsorption. Furthermore, this study highlights the difference in thromboresistance between rough/fibrous surface and smooth/parietal surface of heparin coated pericardium by *in vitro* and more importantly its effects on bioprosthetic valve thrombosis in sheep mitral implantation model.

Materials and Methods

Conjugation of heparin onto glutaraldehyde processed bovine pericardium

A proprietary method was used for glutaraldehyde processing of bovine pericardium and single step heparin conjugation onto it. In brief, bovine pericardia of veterinary certified cattle slaughtered for food purpose at Meat Products of India Ltd., Ernakulam Dist., Kerala was manually defatted and cleaned with several changes of clean water to remove blood and tissue debris. This was again cleaned and packed in sterile normal saline with antibiotic-antimycotic (AA) solution (HiMedia) and transported to the laboratory within 24 hours at room temperature. This pericardium was subjected to low concentration detergent treatment in deionized distilled water for overnight at RT followed by low concentration glutaraldehyde cross-linking for over three weeks. This glutaraldehyde processed bovine pericardium was thoroughly washed in normal saline and immersed in 0.05 Molar HCl solution containing 0.4g heparin for 48 hours at room temperature. This was followed by washing in normal saline solution. Processed tissues were sterilized and stored in 70% ethanol based liquid chemical sterilant until further use. Glutaraldehyde processed bovine pericardium prepared by the same method except for heparin surface conjugation was treated as control.

Demonstration of bound heparin

Heparin specific O-Toluidine blue staining

The presence of surface conjugated heparin post conjugation was demonstrated through O-toluidine blue staining. 1cm x 1cm pieces of heparin coated bovine pericardia were placed in 1ml of PBS (in triplicates and at pH 7.4) and incubated for 60 minutes under constant agitation. Another set of heparin coated samples were incubated in PBS for 7 days under agitation at 37°C. Heparin remaining bound at the end of 60 minutes and 7 days were demonstrated by staining with O-toluidine blue stain (20µg in 10ml deionised distilled water, which is made up to 100ml with deionized distilled water) for 30 minutes. The samples were observed for metachromatic purple staining. This was compared with uncoated sample.

Micro Raman Spectroscopy

The presence of surface conjugated heparin was further confirmed using the highly sensitive Raman spectroscopy technique. 1cm x 1cm pieces of heparin coated and uncoated processed bovine pericardium samples were completely air dried to remove any moisture and was analyzed for Raman spectra using Confocal Raman Microscope (alpha 300A, Witec Inc. Germany); following the method adopted from Witec Alpha 300FR Confocal Raman Microscope User Manual. Instrument was pre calibrated using silicon wafer calibration standard (accepted peak at 520 cm⁻¹). All samples were observed under 20x objective and excited using 785nm Laser

with integration time of 5s and a grating of 300 lines/mm. The resultant spectra were compared to identify laser induced fluorescence peaks for heparin.

Static water contact angle measurement:

Static water contact angle using sessile drop method of the Heparin coated and Heparin uncoated glutaraldehyde processed tissues were measured and compared to that of native tissue to identify the hydrophilic/hydrophobic nature of the material surface. 2cm x 2cm patches in triplicates were used from the native, heparin modified and glutaraldehyde processed pericardia. The angle of contact of a small sessile drop of distilled water placed on the material surface was measured with six measurements on each sample using Goniometer GII, Kern Instruments Inc, USA.

Estimation of Bound Heparin

The heparin content on the modified bovine pericardium was estimated indirectly by measuring the depletion of the metachromatic dye O-Toluidine blue in the immersion liquid following tissue immersion for set periods [23,24,25]. 500mg (blotted dry weight) heparin coated tissues were placed in 2.5mL of 40mg% O-toluidine blue solution followed by the addition of 2.5mL of normal saline. Tissues were incubated for 15min and to this 5mL hexane was added and vortexed. OD values for the supernatants were read at 631nm. A calibration curve was plotted using known concentrations of heparin and a polynomial equation was derived showing the relationship between OD values and the concentration of heparin by curve fitting. The unknown concentration of heparin was derived from the above mentioned equation.

Demonstration of functional activity of bound heparin

Platelet adhesion study by Environmental Scanning Electron Microscopy (ESEM)

Morphology and platelet adhesion on Heparin coated (test) and Heparin uncoated tissues (control) were observed using environmental scanning electron microscopy. For platelet adhesion, the pericardial samples (both test and control) were prepared by washing the samples in normal saline in three changes and were exposed to whole blood containing ACP for 30 minutes at 37°C followed by several washes with PBS. Fixation of samples were done using 2% Glutaraldehyde and kept at -20°C overnight and were repeatedly washed in sterile PBS. Samples were then treated in graded concentrations of 30%, 50%, 70%, 90% and 100% alcohol for 15 minutes each and observed using ESEM (SEM, Hitachi S-2400 Japan) using high vacuum secondary electron detector.

Estimation of adsorbed protein

Total protein adsorbed onto heparin coated tissue was evaluated by Lowry's method of protein estimation. Briefly, heparin coated and heparin uncoated processed bovine pericardia were rinsed thoroughly with normal saline for three times. The samples were then exposed to whole blood containing ACP for duration of 30 minutes at 37°C followed by several washes in phosphate buffered saline solution. To this tissue was added 0.1 N sodium hydroxide and was incubated overnight at room temperature to cleave all the proteins adsorbed to the surface. Samples were then centrifuged at 12000 rpm for 20 minutes at 4°C and the supernatant thus obtained was used to measure the adsorbed protein content on the tissue surface by following Lowry's method of protein estimation.

In vitro surface thrombogenicity evaluation

Heparin coated (test) and heparin uncoated (control) bovine pericardia were evaluated for the thrombogenicity of both their

rough and smooth surfaces using a modified procedure of the whole blood kinetic clotting time method [26,27]. Briefly, rough and smooth surfaces of the two treatment samples (n=6) having a 2 cm x 2 cm dimension were placed with their test surface facing upward in 6-well tissue culture plates. 10% (v/v) of 0.1 M CaCl₂ was added to citrated whole blood to activate the clotting reaction and a 100µL volume of the activated blood was placed on top of the pericardia immediately after activation. Samples were incubated at 37°C for 15 min followed by addition of 2.5 ml of distilled water and incubated for 5 min. This step caused hemolysis of free RBCs not entrapped in the clot on material surface thereby releasing hemoglobin into the supernatant, which is an indirect indication of clot size generated on the test material surface. Each well was sampled from the supernatant, in triplicates (200 µL each) and transferred to a 96-well plate. The concentration of hemoglobin in the supernatant solution was assessed by measuring the absorbance at 540 nm using a 96-well plate reader which is an indirect indicator of the size of clot formed on the tissue surface.

Sheep mitral implantation study

Animal protocol was approved by Institutional Animal Ethics Committee and CPCSEA, Government of India. Four healthy adult male sheep as confirmed by clinical and laboratory examination were implanted with bioprosthetic heart valve in the mitral position under general anesthesia and cardiopulmonary bypass. Atropine sulphate at 0.1mg/Kg was given subcutaneously as premedication, followed by intramuscular Xylazine hydrochloride 0.3mg/Kg and Ketamine hydrochloride 10mg/Kg. General anesthesia was induced using Thiopentone sodium at 5mg/Kg administered intravenously. Anesthesia was maintained with inhalant anesthetic Isoflurane at 1.5 to 2% and propofol 50 mg intravenous bolus administered as and when required. Sheep was positioned on right lateral recumbence and thoracotomy was done through left 4th intercostal space. Lung was retracted, azygous vein was ligated and divided. Pericardium was opened and tented. Under systemic heparinisation at 3mg/Kg, descending aorta and right atrium was cannulated using 18 size aortic cannula 31size DLP cannula respectively to institute CPB. Under cardioplegic heart arrest by delivery through aortic root, bioprosthetic valve was implanted using 15 to 18 3/0 pledgeted coated polyester sutures in horizontal mattress fashion taken at the mitral annulus retaining the native valve and chordae tendinae. Mitral annulus was approached through left atrium via a diagonal incision. Valve opening and closing was checked and left atrial incision was closed with two layers of 5/0 prolene sutures. Aortic clamp was removed and heart resumed rhythm spontaneously in most of the time. In some cases external defibrillation was required. Heart was de-aired, bypass was terminated and heart decannulated in stages with dopamine support. Chest was closed in layers with a pleuro-pericardial drain. The sheep were given 100mg Dipyridamol once daily for up to one-month post operatively as antiplatelet. Apart from this intramuscular Tramadol 50mg SID, Dexamethasone 4mg SID for 3 days, Ceftriaxone-Sulbactam 1.5 g SID for 7 days, Paracetamol 300mg and Meloxicam 5mg SID for 3 days were given along with oral probiotics post-operatively. Chest tube was removed on the next day and sutures were removed on 10th day.

Test valve fabrication

Test valves were fabricated using heparin conjugated bovine pericardium which had completed ISO 10993 tests and *in vivo* calcification study in juvenile rat subcutaneous implantation model. The first sheep was implanted with a bioprosthetic valve which is having heparin coated rough (fibrous) surface as the inflow surface, and the rest three sheep with the bioprosthetic valve with the heparin coated smooth surface (parietal surface) as the inflow surface. The

planned observation period was 6 months. One sheep was retained up to 12 months.

Statistical analysis

Statistical analysis was performed using Microsoft Excel software. F test was performed to study the variance and based on its significance, Student's t- test (for equal or un-equal variance) was used for further comparison between test and control groups. The results were considered significant at p-values less than 0.05 and presented as mean ± standard deviation (SD) along with p-value.

Results

Demonstration of bound heparin

Qualitative study: O-Toluidine blue staining

The presence of the conjugated heparin remaining on the sample surface after 60 minutes and 7 days of incubation under agitation was demonstrated by ortho toluidine blue staining reaction. The intense blue color of the metachromatic dye in comparison to light blue color of control samples indicated presence of surface bound heparin on heparin coated processed pericardium even after incubation in PBS (pH 7.4) for 7 days under agitation (figure 1).

Micro Raman Spectroscopy

Analysis of the Raman spectra of heparin coated and uncoated glutaraldehyde processed pericardia showed high level of background fluorescence in both groups on account of glutaraldehyde treatment as observed elsewhere [29]. Compared to the control group, spectrum for heparin coated glutaraldehyde processed bovine pericardium showed a distinct peak of low intensity at 1085 cm⁻¹ and an increase in intensity of the peak in the range 1250-1260 cm⁻¹ (figure 2), which can be assigned to the absorption by the primary and secondary sulfate groups of the heparin molecule as reported earlier [30].

Static water contact angle measurement

Water contact angle for both the rough and smooth surfaces of the heparin coated sample as well as the native bovine pericardium were below 90° and hence it is assumed to be hydrophilic. Moreover, a decrease in contact angle for the smooth surface compared to that of the rough surface as indicated in figure 3 was observed in both the groups irrespective of having heparin coating. Following heparin coating the contact angle decreased more for rough surface than for smooth surface which was statistically significant. Measured contact angle decreased from 80.45° ± 4.37° to 68.11° ± 6.87° for the rough

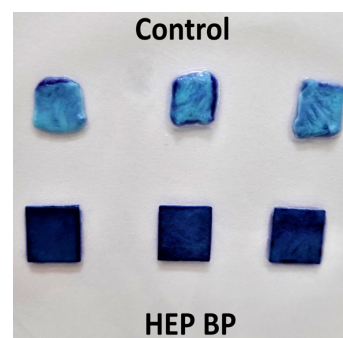


Figure 1: Photograph showing O-toluidine adsorption by heparin coated bovine pericardium as compared to native tissue even after seven days of incubation in PBS (pH 7.4)

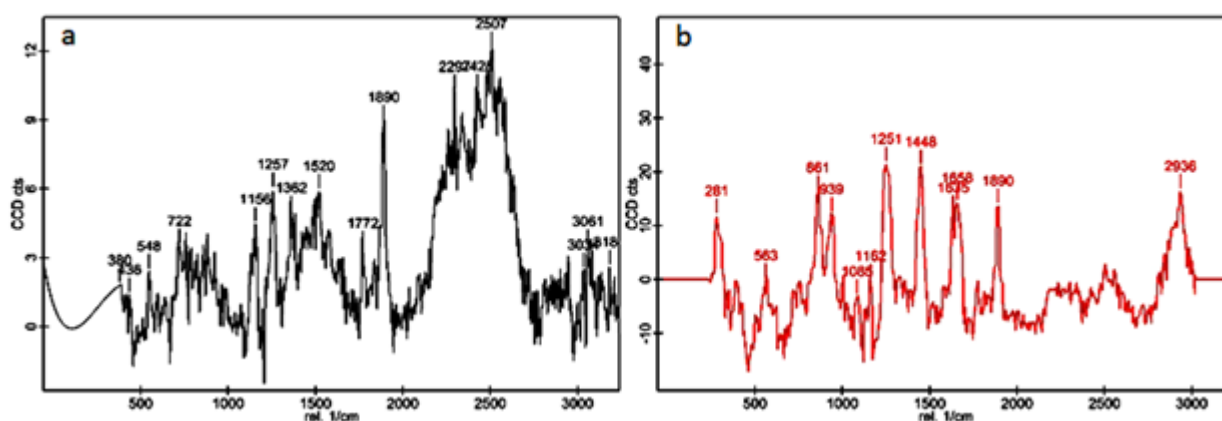


Figure 2: Micro Raman spectra of (a) Heparin uncoated glutaraldehyde processed bovine pericardium control group and (b) Heparin conjugated glutaraldehyde processed bovine pericardium. Figure (b) shows a distinct peak of low intensity at 1085 cm⁻¹ and an increase in intensity of the peak in the range 1250-1260 cm⁻¹

surface ($p=0.001$) and from $74.54^\circ \pm 5.32^\circ$ to $66.9^\circ \pm 6.57^\circ$ for the smooth surface ($p=0.02$), implying that following heparin coating, the pericardial surfaces have become more hydrophilic, with the effect of coating more prominent in the case of rough surface. The contact angle for glutaraldehyde processed heparin uncoated tissue could not be measured as sessile drop could not be formed on its surface and is reported as highly hydrophobic.

Estimation of bound heparin

Colorimetric assay determined the residual O-toluidine dye in the immersion liquid by measuring the spectrophotometric absorbance at 631nm after the set incubation periods. The depletion in absorbance was used as an indirect measure of bound heparin concentration on processed tissue surface. Following the assay and substituting the observed absorbance value in the polynomial equation, the heparin content was measured to be 0.717 ± 0.019 mg/500mg (wet weight) processed tissue following heparin conjugation.

Functional evaluation of bound heparin

Platelet adhesion study

When compared to uncoated surface, heparin coating reduced platelet adhesion after incubation in anti-coagulated whole blood for 30 minutes at physiologic pH and temperature as observed from the SEM image given as figure 4. Hence it is understood that the covalent immobilization has not compromised the physiological anticoagulant activity of heparin and the processed bovine pericardium surface is thus rendered less susceptible to platelet adhesion.

Protein adsorption study

Protein adsorption studies done through estimation of eluted protein from the whole blood exposed surfaces revealed that following heparin coating the adsorbed protein content on the heparin coated surface significantly reduced from 0.402 ± 0.019

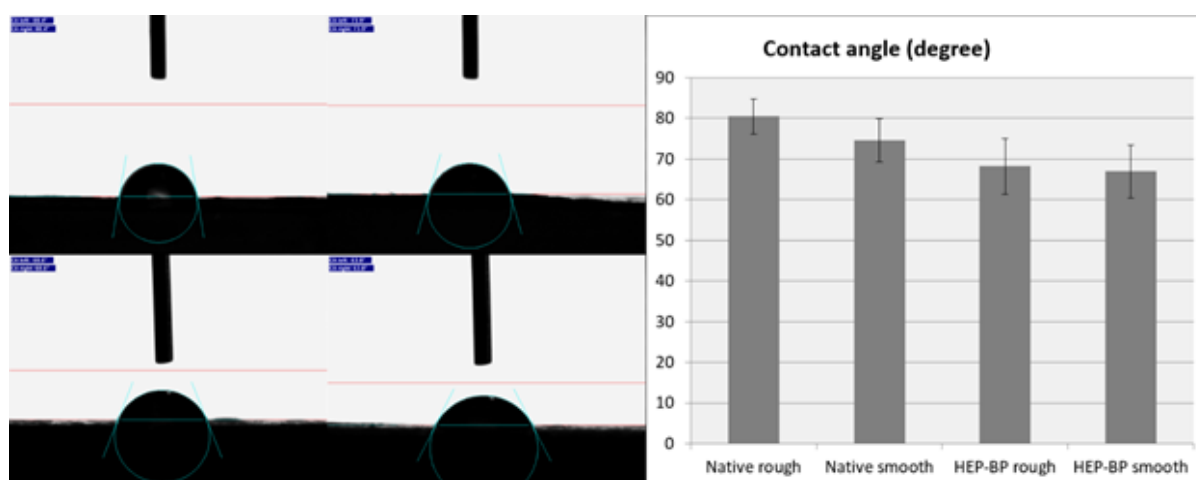


Figure 3: Chart showing water contact angle measurement of A) Native bovine pericardium rough surface, B) Native bovine pericardium smooth surface C) Heparin coated bovine pericardium rough surface and D) Heparin coated bovine pericardium smooth surface

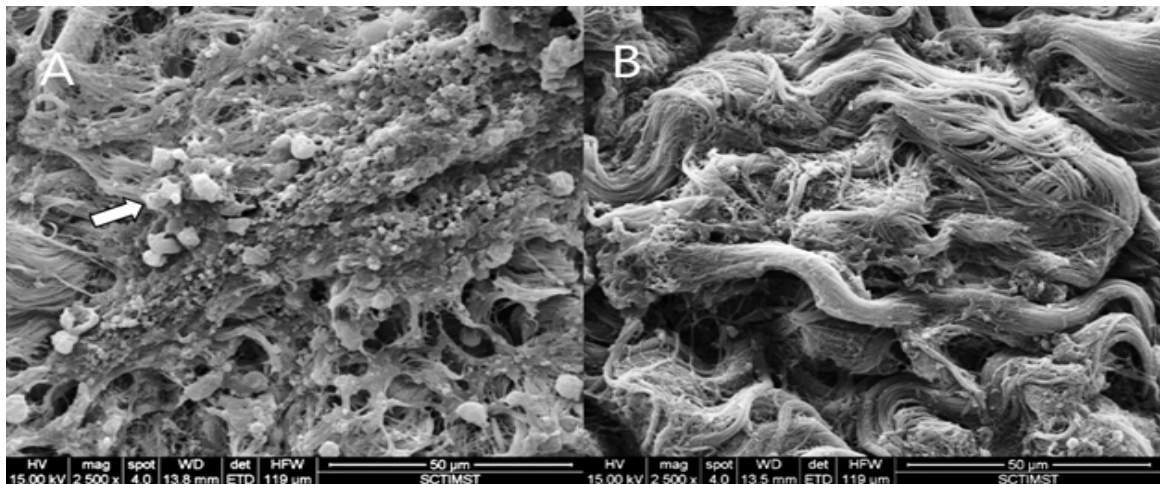


Figure 4: ESEM picture showing the presence of platelet adhesion on heparin unbound BP surface (A-bold arrow) in comparison to its absence in heparin coated BP surface (B)

mg/100mg tissue to 0.227 ± 0.0519 mg/100 mg tissue ($p=0.01$). This indicated the possibility for reduced blood coagulation on heparin coated pericardial surface (figure 5). This observation correlates well with the knowledge that when attached to a surface, covalently immobilized heparin has the capacity to reduce the thrombogenicity of artificial materials by way of reducing pro-coagulant protein adsorption on to surface [32], the effectiveness of which is dependent on the extent to which the catalytic activity of heparin is preserved after immobilization process, specifically on the AT uptake capacity of the heparin coated surface [33].

In vitro surface thrombogenicity evaluation

Thrombogenicity of the heparin coated tissue surface was analyzed in comparison to that of uncoated tissue following whole blood kinetic clotting time method with standardized time interval of 15 minutes. The contribution of rough and smooth pericardial surface to its surface thrombogenicity was also studied. The concentration of free hemoglobin measured by reading the absorbance at 540nm

is as an indirect indication of the size of clot formed on the tissue surface by tissue-blood interaction. It is assumed that only the RBCs outside of the clot are lysed by the addition of distilled water resulting in the release of hemoglobin into the medium. Therefore, absorbance value observed is inversely proportional to the size of clot, and hence to the surface thrombogenicity thereby indicating that higher hemoglobin value corresponds to lesser surface thrombogenicity (figure 6). As per this test, heparin coated smooth surface of the pericardium showed least thrombogenicity followed by heparin coated rough surface, heparin un-coated smooth surface and finally heparin uncoated rough surface which showed the least thromboresistance among the samples (figure 7). It was observed that, following heparin coating, the thromboresistance of smooth surface of glutaraldehyde processed pericardium significantly improved ($p=0.0001$) compared to that of rough surface ($p=0.0005$). It was also observed that the rough and smooth surfaces of heparin coated tissue also differed significantly ($p=0.006$) in their thromboresistance, whereas in the case of heparin uncoated tissue, this difference, though present, was not statistically significant ($p=0.067$).

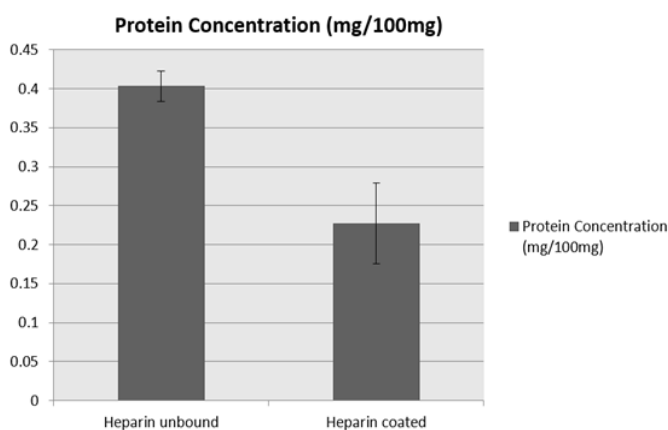


Figure 5: Chart showing eluted protein content in heparin uncoated and coated processed bovine pericardium respectively

Bioprosthetic valve implantation in sheep

Sheep implanted with the bioprosthetic valve having rough surface of pericardium forming the inflow surface showed bilateral jugular pulse at the base of the neck by 46th post-operative day and this ascended upward distally. Concomitantly, animal started showing tachypnea and respiratory distress which was managed with bronchodilators and diuretics. However, on 53rd day this sheep was found dead. Autopsy of this animal showed thrombus formation on the inflow surface of the valve almost occluding the valve affecting the forward blood flow (figure 7).

The other two sheep implanted with the bioprosthetic valve having smooth pericardial surface forming the inflow surface, completed the scheduled observation period of 6 months. Autopsy at the end of this observation period revealed thrombus free inflow surface (figure 8).

Discussion

The present study aimed at producing a thromboresistant surface

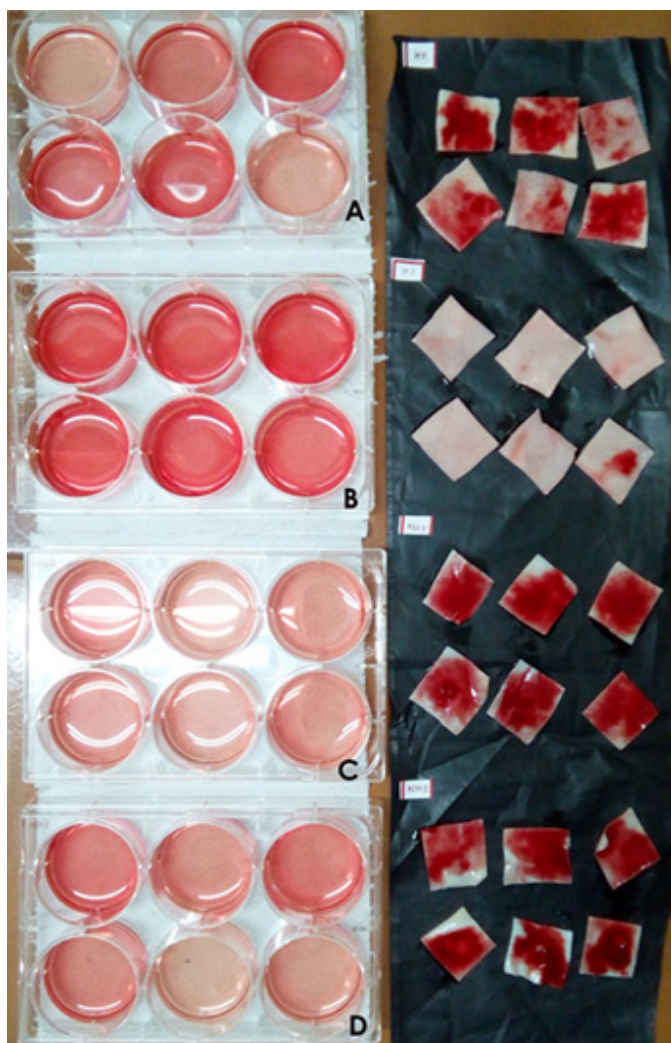


Figure 6: Photograph showing difference in clot formation in treatment groups A: Heparin coated rough surface, B: Heparin coated smooth surface C: Non-heparin coated rough surface D: Non-heparin coated smooth surface. Note the color intensity of pericardial wash in petri dish correlates with clot formation on the pericardial surface as maximum clot formation in sample D and vice versa in sample B

on glutaraldehyde processed bovine pericardium using a simple single step method and demonstrated the difference in thrombogenicity of rough (fibrous) and smooth (parietal) surface of heparin coated pericardium. It was carried out by heparin conjugation to a glutaraldehyde processed bovine pericardial surface, by hemi-acetal and acetal formation between aldehyde groups of the glutaraldehyde treated pericardium and OH groups of the heparin under acidic pH, without affecting sulphate groups responsible for the anticoagulation property of the heparin. This simple single-step reaction possibly has led to the formation of direct covalent linkage between heparin and glutaraldehyde treated pericardium resulting in a stable, functionally active heparin coated tissue surface. Literature reveal that the activity of surface bound heparin is largely dependent on the type of surface interaction between heparin and the material [34-36]. Therefore, surface binding of heparin does not always guarantee effective anti-thrombotic activity. Through this study it was demonstrated that this method

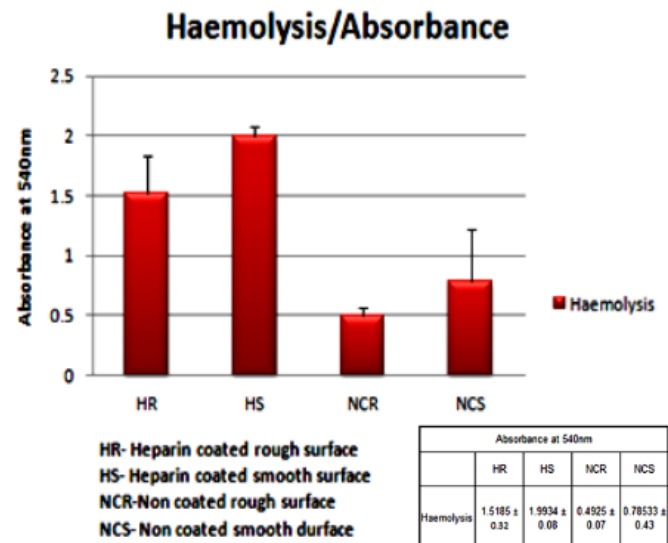


Figure 7: Chart showing the absorbance values at 540nm for the rough and smooth surfaces of Heparin coated and uncoated processed pericardia. Graph indicates absorbance as a measure of hemolysis. The greater the absorbance value, lesser the size of clot formed

of heparin conjugation on glutaraldehyde processed bovine pericardium did not compromise the anticoagulant activity of heparin. The successful immobilization of heparin to the processed pericardium tissue was visualized qualitatively through O-toluidine blue staining of heparin coated tissue in comparison to native tissue as control and quantitatively through the estimation of bound heparin.

The presence of heparin on glutaraldehyde processed bovine pericardium surface was confirmed by micro Raman spectroscopy. For glutaraldehyde cross linked pericardium, a weak peak in the range between 1150-1060 cm^{-1} corresponds to the asymmetric stretch C-O-C vibration [41] which can be attributed to an ether-type bond formation between the collagen fibers and glutaraldehyde [42]. In the present study, the presence and intensity of the peak in the range 1150-1060 cm^{-1} in comparison with the control tissue may be assumed to be contributed additionally by the acetal bond formation between the aldehyde groups of glutaraldehyde and hydroxyl groups of heparin. Studies have previously shown that glutaraldehyde cross-linking in pericardium results in very high fluorescence background, which interferes with the Raman spectra [29]. This may be factored into consideration for the very low intensity of the peaks formed and the presence of large number of peaks that could possibly skew the distribution of the significant peaks for heparin.

Results of protein adsorption and platelet adhesion studies showed an overall decrease in the amount of coagulation effectors on the heparin bound pericardium which may be attributed to its anticoagulant activity observed in the heparin coated samples. Heparin, through the interaction of its high affinity pentasaccharide sequence with antithrombin [37], inhibits the downstream coagulation cascade through inactivation of coagulation enzymes such as thrombin factor (IIa), factors Xa, IXa, XIa, and XIIa [38]. Also, it is known that heparin is a highly hydrophilic molecule and studies have previously shown decreased adsorption of plasma fibrinogen and subsequent thrombin formation on hydrophilic surfaces due to specific surface adsorption through α C-domain of



Thrombus on the inflow region formed by rough pericardial surface at 53 days



Thrombus free inflow region formed by smooth pericardial surface at 6 months

Figure 8: Photograph showing thrombus formation on valve inflow in the first row (heparin coated rough pericardial surface) compared to thrombus free inflow in the second row (heparin coated smooth pericardial surface)

fibrinogen [39]. The results of static water contact angle for the heparin coated tissue indicate that this surface modification rendered the surface even more hydrophilic than the native pericardium surface. Heparin itself is a hydrophilic molecule with various functional groups that contribute to its hydrophilic nature [40]. Direct conjugation of heparin to the glutaraldehyde processed bovine pericardium is thus expected to lower the contact angle for the otherwise hydrophobic modified surface, which could have potentially lowered both protein adsorption and subsequent platelet adhesion by the altered surface adhesion of plasma proteins. The reduced protein adsorption through the above mentioned mechanisms may be attributed to the overall decrease in platelet adhesion on the heparin coated glutaraldehyde processed tissue as visualized in the SEM.

The difference in thromboresistance of heparin coated rough and smooth pericardial surfaces were demonstrated by whole blood kinetic clotting time method as this method allowed specific study of coated surfaces. Results indicated that the surface thrombogenicity for the rough and smooth surfaces of heparin coated tissue varied significantly with increased thromboresistance for the smooth surface. Interestingly, for the heparin uncoated tissue, the difference in surface thrombogenicity identified was not statistically significant. Pericardial valves are typically fabricated with the rough side toward the inflow, to keep this surface well washed and thereby minimize the possibility of thrombosis [44]. However, the first bioprosthetic valve fabricated in this fashion with the heparin coated rough surface forming the inflow surface, thrombosed in 53 days in spite of the proven anti-platelet therapy given to this sheep [45]. Interestingly,

the rest two sheep implanted with the bioprosthetic valve having heparin coated smooth surface forming the inflow, completed the planned observation period of six months without valve thrombosis. This raises an interesting question, that is 'does the hydrophilic heparin coating make the rough surface of pericardium vulnerable to valve thrombosis even when it is significantly more thromboresistant than hydrophobic heparin uncoated pericardium?'. A conclusive answer to this question will be relevant in the manufacture of bioprosthetic heart valve using pericardium coated with hydrophilic thromboresistant coating such as heparin.

Conclusion

Through the *in vitro* experiments it is successfully verified that the key events in thrombus formation such as protein adsorption and platelet activation which are critical in determining the success of bioprosthetic valve with respect to subclinical valve thrombosis, are considerably reduced in heparin modified glutaraldehyde processed bovine pericardium in contrast to heparin unmodified tissue. And, differential thromboresistance were observed in the smooth (parietal) and rough (fibrous) surface of the pericardium with maximum thromboresistance observed in heparin coated smooth surface and the least thromboresistant was non-heparin coated rough surface of pericardium. However, contrary to the established knowledge, rough surface of pericardium caused valve thrombosis when it is heparin coated and hydrophilic.

Acknowledgement: The authors gratefully acknowledge the TRC grant and the support given by the Head, BMT Wing and the Director S.C.T.I.M.S.T. for the conduct of this study.

References

- Hilbert S.L., Schöen F.J., Ferrans V.J., Overview: Allograft Heart Valves. In: Cardiac Reconstructions with Allograft Tissues. Springer, New York, 193-199 (2005).
- Pillsbury, R.C., Shumway, N.E. Replacement of the aortic valve with the autologous pulmonic valve. *Surgical Forum*, 17, 176-177 (1966).
- Barratt-Boyes B.G. Homograft aortic valve replacement in aortic incompetence and stenosis. *Thorax*, 19(2), 131-150 (1964).
- Ross D.N. Homograft replacement of the aortic valve. *Lancet*, 2(7254), 487 (1962).
- Murray, G., Roschlau, W., Loughheed, W. Homologous Aortic-Valve-Segment Transplants as Surgical Treatment for Aortic and Mitral Insufficiency. *Angiology*, 7(5), 466-471 (1956).
- Ross D.N. Replacement of aortic and mitral valves with a pulmonary autograft. *Lancet*, 2(7523), 956-958 (1967).
- Puri, R., Auffret, V., Rodés-Cabau, J. Bioprosthetic Valve Thrombosis. *J. Am. Coll. Cardiol.*, 69(17), 2193-2211 (2017).
- Manji, R.A., Lee, W., Cooper, D. Xenograft bioprosthetic heart valves: Past, present and future. *Int. J. Surg.*, 23(B), 280-284 (2015).
- Ionescu, M.I., Smith, D.R., Hasan, S.S., Chidambaram, M., Tandon, A.P. Clinical durability of the pericardial xenograft valve: ten years' experience with mitral replacement. *Ann. Thorac. Surg.*, 34(3), 265-277 (1982).
- Head, S., Çelik, M., Kappetein, A. Mechanical versus bioprosthetic aortic valve replacement. *European Heart Journal*, 38(28), 2183-2191 (2017).
- Sachdev, S., Bardia, N., Nguyen, L., Omar, B. Bioprosthetic Valve Thrombosis. *Cardiology Research*, 9(6), 335-342 (2018).
- Rossee, L., De Backer, O., Søndergaard, L. Clinical Valve Thrombosis and Subclinical Leaflet Thrombosis Following Transcatheter Aortic Valve Replacement: Is There a Need for a Patient-Tailored Antithrombotic Therapy? *Frontiers in Cardiovascular Medicine*, 6, 44 (2019).
- Loop, F.D., Cosgrove, D.M., Kramer, J.R., Lytle, B.W., Taylor, P.C., Golding, L.A., Groves, L.K. Late clinical and arteriographic results in 500 coronary artery reoperations. *The Journal of Thoracic and Cardiovascular Surgery*, 81(5), 675-685 (1981).
- Jaffer, I.H., Fredenburgh, J.C., Hirsh, J., Weitz, J.I. Medical device-induced thrombosis: what causes it and how can we prevent it? *Journal of Thrombosis and Haemostasis*, 13(S1), S72-S81 (2015).
- Okamura, K., Chiba, C., Iriyama, T., Itoh, T., Maeta, H., Ijima, H., Mitsui, T., Hori, M. Antigen depressant effect of glutaraldehyde for aortic heterografts with a valve, with special reference to a concentration right fit for the preservation of grafts. *Surgery*, 87(2), 170-176 (1980).
- D.L. Amrani, C. Lee, K. Earles, J. DiOrio, M. Murphy, J. Yang, S. Rubalcaba, A.LiVecchi. An in vitro bovine pericardial hemocompatibility testing system. *J Heart Valve Dis*, 7(3), 268-72 (1998).
- Lee, W.K., Park, K.D., Keun Han, D., Suh, H., Park, J.C., Kim, Y.H. Heparinized bovine pericardium as a novel cardiovascular bioprosthesis. *Biomaterials*, 21(22), 2323-2330 (2000).
- Milgater, E., Uretzky, G., Siberman, S., Appelbaum, Y., Shimon, D. V., Kopolovic, J., Cohen, D., Jonas, H., Appelbaum, A., Borman, J. B. Pericardial meshing: an effective method for prevention of pericardial adhesions and epicardial reaction after cardiac operations. *The Journal of Thoracic and Cardiovascular Surgery*, 90(2), 281-286 (1985).
- Schoen, F.J., Collins, J.J., Jr, Cohn, L.H. Long-term failure rate and morphologic correlations in porcine bioprosthetic heart valves. *The American Journal of Cardiology*, 51(6), 957-964 (1983).
- Culliford, A.T., Spencer, F.C. Guidelines for safely opening a previous sternotomy incision. *The Journal of Thoracic and Cardiovascular Surgery*, 78(4), 633-638 (1979).
- Gott, V.L., Whiffen, J.D., Dutton, R.C. Heparin Bonding On Colloidal Graphite Surfaces. *Science*, 142(3597), 1297-1298 (1963).
- Biran, R., Pond, D. Heparin coatings for improving blood compatibility of medical devices. *Advanced Drug Delivery Reviews*, 112, 12-23 (2017).
- Qiao, Y., Liu, X. Biocompatible Coating, *Comprehensive Materials Processing*, 4, 425-447 (2014).
- Balamurugan, K., Kalaichelvan V., Dey A., Isolation and identification of heparin like substances from the body tissue of *Conus musicus*. *International Journal of Pharm Tech Research*, 1, 1650-1653 (2009).
- Ahola, M., Säilynoja, E., Raitavuo, M., Vaahtio, M., Salonen, J., Yli-Urpo, A. In vitro release of heparin from silica xerogels. *Biomaterials*, 22(15), 2163-2170 (2001).
- Smith, P.K., Mallia, A.K., Hermanson, G.T. Colorimetric method for the assay of heparin content in immobilized heparin preparations. *Analytical Biochemistry*, 109(2), 466-473 (1980).
- Cornelius, R.M., Sanchez, J., Olsson, P., Brash, J.L. Interactions of antithrombin and proteins in the plasma contact activation system with immobilized functional heparin. *Journal of Biomedical Materials Research*, 67(2), 475-483 (2003).
- Umashankar P.R., Arun T., Kumari T.V. Short duration glutaraldehyde crosslinking of decellularised bovine pericardium improves biological response. *J Biomed Mater Res A.*, 97(3), 311-320 (2011).
- Jastrzebska M., Wrzalik R., Kocot A., Zalewska-Rejda J., Cwalina B. Raman spectroscopic study of glutaraldehyde-stabilized collagen and pericardium tissue. *Journal of Biomaterials Science, Polymer Edition*, 14(2), 185-197 (2003).
- Noishiki Y, Miyata T. Successful animal study of small caliber heparin-protamine-collagen vascular grafts. *Transactions of the American Society for Artificial Internal Organs*, 31, 102-6 (1985).
- Liao, D., Wang, X., Lin, P.H., Yao, Q., Chen, C. Covalent linkage of heparin provides a stable anti-coagulation surface of decellularized porcine arteries. *Journal of Cellular and Molecular Medicine*, 13, 2736-2743 (2009).
- Sabino, R. M., Papat, K. C. Evaluating Whole Blood Clotting in vitro on Biomaterial Surfaces. *Bio-protocol*, 10(3), e3505 (2020).
- Ahola, M., Säilynoja, E., Raitavuo, M., Vaahtio, M., Salonen, J., Yli-Urpo, A. In vitro release of heparin from silica xerogels. *Biomaterials*, 22(15), 2163-2170 (2001).
- Sushko, N., Firsov, S., Zhibankov, R., Tsarenkov, V., Marchewka, M., Ratajczak, C. Vibrational spectra of heparins. *Journal of Applied Spectroscopy*, 61(5-6), 704-707 (1994).
- Kodama, K., Pasche, B., Olsson, P., Swedenborg, J., Adolfsson, L., Larm, O., Riesenfeld, J. Antithrombin III Binding to Surface Immobilized Heparin and Its Relation to F Xa Inhibition. *Thrombosis and Haemostasis*, 58(4), 1064-1067 (1987).
- Sanchez, J., Elgue, G., Riesenfeld, J., Olsson, P. Studies of Adsorption, Activation, and Inhibition of Factor XII on Immobilized Heparin. *Thrombosis Research*, 89(1), 41-50 (1998).
- Hirsh, J., Anand, S., Halperin, J., Fuster, V. Mechanism of Action and Pharmacology of Unfractionated Heparin. *Arteriosclerosis, Thrombosis, and Vascular Biology*, 21(7), 1094-1096 (2001).
- Khatib, R., Wilson, F. Pharmacology of Medications Used in the Treatment of Atherosclerotic Cardiovascular Disease. *Encyclopedia of Cardiovascular Research and Medicine*, 68-88 (2018).
- Sanchez, J., Elgue, G., Riesenfeld, J., Olsson, P. Control of contact activation on end-point immobilized heparin: The role of antithrombin and the specific antithrombin-binding sequence. *Journal of Biomedical Materials Research*, 29(5), 655-661 (1995).
- Kumar, S., Ali, J., Baboota, S. Polysaccharide nanoconjugates for drug solubilization and targeted delivery. *Polysaccharide Carriers for Drug Delivery*, 443-475 (2019).
- Zhang, L., Casey, B., Galanakis, D., Marmorat, C., Skoog, S.A., Vorvolakos, K., Simon, M., Rafailovich, M. The influence of surface chemistry on adsorbed fibrinogen conformation, orientation, fiber formation and platelet adhesion. *Acta biomaterialia*, 54, 164-174 (2017).
- Lin-Vien, D., Lin-Vien, D. *The handbook of infrared and Raman characteristic frequencies of organic molecules 1991*. Academic Press.
- Lai, J.Y., Ma, D.H., Glutaraldehyde cross-linking of amniotic membranes affects their nanofibrous structures and limbal epithelial cell culture characteristics. *International Journal of Nanomedicine*, 8, 4157-4168 (2013).
- Schoen F.J., Levy R.J., Tissue heart valves: current challenges and future research perspectives, *J Biomed Mater Res*, 47, 439-464 (1999).
- Bhuvaneshwar, G.S., Muraleedharan, C.V., Vijayan, G.A., Kumar, R.S. Valiathan, M.S., Development of the Chitra tilting disc heart valve prosthesis, *J Heart Valve Dis*, 5(4), 448-58 (1996).

Original Article

Polysaccharide-PVA/PEG blended Crosslinked Hybrid Hydrogels for Cardiac Tissue Engineering

Soumya K. Chandrasekhar^{1,2}, Joshi C. Ouseph^{2*}¹Department of Zoology, KKTU Government College (University of Calicut), Pullut, Kodungallur, Thrissur 680663, India²Department of Zoology, Christ College (University of Calicut), Irinjalakuda, Thrissur 680125, India

Received: 9 October 2022

Accepted: 7 January 2023

Published online: 30 June 2023

Keywords: cardiac tissue engineering, hybrid hydrogels, biocompatibility, regenerative cardiology, polymeric blend

As the native ECM exists as hydrogel, biocompatible polymeric hydrogel-based templates promise tissue engineering applications owing to their biomimetic nature. Hence, the choice of co-polymers employed is crucial in determining the cardiac performance of such hydrogels. On this juncture, the present study aimed to engineer biocompatible hybrid hydrogel scaffolds by the interpenetration and crosslinking of the natural polymers with synthetic polymers for cardiac regeneration. Two sets of hydrogels ACPVs (alginate, carboxy methyl cellulose and PVA as components) and ASPGs (Alginate, starch, and PEG as components) were prepared. FT-IR revealed the ample hydrophilic surface functional groups, water dynamics unveiled appreciable water holding capacity befitting native cardiac ECM, SEM analysis displayed surface porosity and dynamic contact angle unveiled the amphiphilic chemistry. The hydrogels were biodegradable as evaluated by aging in simulated biological fluids and the cytocompatibility was assessed with MTT cell viability assay and direct contact assay using H9c2 cardiomyoblasts. The hydrogel supported the growth and survival of H9c2 cardiomyoblasts onto the interstices. Also, the hydrogels were effective in imbibing antibiotics and arrested the growth of major Gram-positive and Gram-negative bacteria. Overall, the findings demonstrated that the reinforced hydrogel system exhibits optimum physicochemical properties, excellent biocompatibility, and appreciable biological performance to support cardiac cell growth suggesting the promising translational avenues in regenerative cardiology.

© (2023) Society for Biomaterials & Artificial Organs #20066723

Introduction

World Health Organization (WHO) recently reported that cardiovascular diseases (CVDs) accounts ~17.9 million deaths globally [1]. Also, American Heart Association (AHA) estimated a 21.1% increase in global CVD deaths from 2007 to 2017 [2]. Among CVDs, the incidence of myocardial infarction (MI) is alarming as four out of every five CVD death is due to heart failure [3]. The ischemic damage following the MI impairs cardiac function and output. The conventional treatment strategies for managing MI rely on pharmacotherapy and surgical restitution; however, heart transplantation remains to be the ultimate management option. Moreover, necessity for lifelong medicines, dearth of organ donors, infection, and immunological rejections associated with transplantation surgery offer hurdles. Even though

advancements in the field of biomedical engineering have been a boon in creating artificial organs, translational applications are limited warranting biocompatibility and functionality [4].

Cardiac tissue engineering (CTE) has been considered to be promising for the effective management of MI [5]. CTE approach triggers the inherent regenerative ability of human body by providing a supporting matrix loaded with specific cell phenotypes and growth factors using appropriate templates. The initial tissue consortium formed on such scaffolds accelerates ECM deposition restoring/regenerating the lost functions [6]. Importantly, meticulous designing of 3D scaffolds is important as the success rate depends solely on the performance of cells in scaffold until a functional cardiac extra cellular matrix (ECM) is being reconstructed by the surviving tissue. Hence, an ideal scaffold for CTE requires the physicochemical and biological properties identical to native cardiac ECM for supporting the formation of functional cardiac tissue [1]. In addition, the chance of infection warrants further

* Corresponding author

E-mail address: sowmyakc.kc@gmail.com (Dr. Joshi C. Ouseph Ph.D)

attention suggesting the scaffolds with antimicrobial properties [7].

On this background, the present study focused on the design and evaluation of a panel of hybrid hydrogel templates synthesized by interpenetrating the natural polysaccharide alginate, starch and the polysaccharide derivative carboxymethyl cellulose (CMC) with synthetic polymers such as poly(vinyl alcohol) (PVA) and poly(ethylene glycol) (PEG) for functional CTE applications.

Materials and Methods

Synthesis of hybrid hydrogels

Alginate-CMC-PVA (ACPV) hydrogels were prepared interpenetrating alginate, CMC and PVA. Briefly, 3% alginate was suspended in 5% Na_2HPO_4 which was mixed with 2% CMC and 5% PVA, followed by stirring the 1.5 % CaCl_2 and the mix was casted at 70°C overnight. The dried hydrogels were carefully removed from the petri dish and incubated in 10% CaCl_2 for an hour for additional crosslinking. Two batches of ACPV hydrogels, ACPV1 and ACPV2 were prepared which differs in alginate content: 5 ml and 10 ml respectively. The volume of PVA and CMC remained 5 ml each for both the batches. Similarly, the Alginate-starch-PEG (ASPG) hydrogels were prepared by mixing 3% alginate with 2% PEG in 5% starch blend following the above procedure. ASPG1 used 2.5 ml alginate and 5 ml blend whereas ASPG2 used 10 ml alginate and 5 ml blend. The hydrogel sheets were washed overnight in distilled water, freeze dried and stored at room temperature (RT) for further studies.

Analysis for surface functional groups

ATR spectrum, for assessing the surface functional groups, of ACPV and ASPG hybrid hydrogel subsets were recorded by using Nicolet iS50 FTIR spectrometer using lyophilized samples. Digitization and processing of the data were done using Microsoft Excel and Origin software was used to plot the spectra.

Equilibrium water content and weight swelling ratio

Freeze dried hydrogel samples were used to determine the water content and swelling capacity by soaking in distilled water (DW) and allowed to attain equilibrium for 24 h at RT. The swollen samples were wiped carefully using blotting paper to remove the excess water prior to weighing. The equilibrium water content and the swelling efficiency of the hydrogels were determined from the dry and wet weights following previously published reports [8].

Surface morphometry

The surface morphology and pore size of the scaffolds were determined using scanning electron microscope equipped with energy dispersive X-ray spectroscopy (SEMEDAX). The average length and breadth of pores on scaffold surfaces were calculated from SEM images using ImageJ software using multi-measure plugin following previously published protocols [9].

Tensile strength

Tensile strength of water swollen hydrogels were determined using Shimadzu Universal Testing Machine (model AG-I) using dumb bell-shaped specimens (ISO 527-2 type 5A). Tensile strength was tested with a load cell of 100 N at RT with a crosshead speed of 10 mm/min. The tensile properties were determined as reported elsewhere [10].

Dynamic water contact angle

Six clean samples of uniformly rectangular shape and known width

were swelled in distilled water and were used for determining the surface hydrophilicity by dynamic contact angle. The advancing and receding contact angle were determined by Wilhelmy method using KSV sigma 701 tensiometer by using distilled water as a solvent. The samples were immersed to a depth of 10 mm at a speed of 5 mm/min ignoring the first 2 mm length. The advancing and receding contact angle values were obtained automatically using the software associated with the instrument [9].

Biostability

The biostability of hybrid hydrogel subsets were determined by aging in PBS at RT. Changes in dry weight, pH, and total dissolved solids (TDS) were determined at a regular interval of 10 days for a period of 30 days [10].

Protein adsorption

The water swollen hydrogels were incubated with commercially available foetal bovine serum (FBS) (1:10 dilution in PBS) at 37°C on a shaker incubator overnight. Then the scaffolds were gently washed with PBS to remove the loose/unbound proteins, and vortexed in minimum PBS to extract the adhered proteins which were quantified by standard BCA method. Then percentage of proteins adsorbed on to the hydrogels was quantified with respect to total plasma protein content as control. SDS-PAGE using the extracted proteins was performed for assessing the extent of albumin adsorption using albumin (50µg/µl) as standard. The relative adsorption of albumin was calculated using the image analysis ImageJ software from the bands obtained the SDS-PAGE gels.

Cytocompatibility

Cell culture and maintenance

Rat cardiomyoblast cells (ATCC) was used for the cytocompatibility evaluations. The cells were grown in high glucose DMEM with 10% fetal bovine serum (FBS) (Cat# 30-2020, ATCC) at standard culture conditions (5% CO_2 , 37°C, and antibiotics). Upon 70-80% confluence the cells were split using standard trypsinization protocols.

Cytotoxicity

The cytotoxicity of hydrogels extract (in cell culture medium) was determined by standard MTT assay using H9c2 cardiomyoblasts cell culture following previously reported protocol [11].

Direct contact assay

The toxicity of the hydrogels under the direct influence of cell contact was determined by direct contact assay. Then the hydrogel samples (10 mm diameter) were placed over the monolayer of H9c2 cells and allowed to proliferate for 24 h which were examined microscopically for alterations in morphology compared to the control.

Anti-microbial assay

The antibiotic releasing efficiency of the hydrogels was analyzed using disc diffusion method. To prepare antibiotic incorporated scaffolds 10 mm discs were prepared and 5, 10, 20 µg respectively of amikacin and vancomycin were loaded by diffusion. Both gram-positive (*Staphylococcus sps.*) and gram-negative bacteria (*Pseudomonas sps.*) used for the study were kindly donated by Polyclinic, Kerala, India. The bacteria were cultured on Muller Hinton agar plates, the antibiotic incorporated scaffolds were placed, incubated at 37°C for 24 hours and the zone of inhibition was measured. Untreated

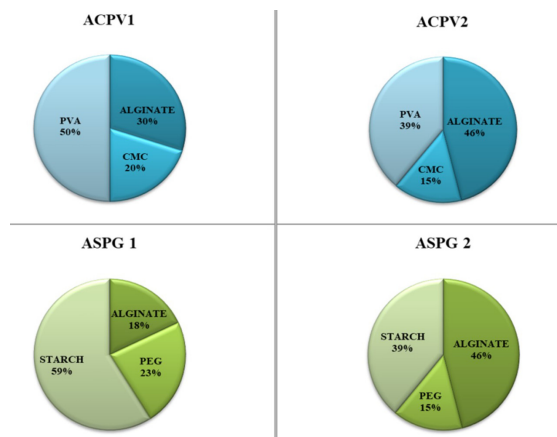


Figure 1: Percentage composition of constituent polymers in ACPV and ASPG hybrid hydrogel subsets

discs were used as control.

Statistical analysis

The results were expressed as mean \pm SEM and the statistical analysis for biodegradation studies was performed by Tukey's multiple comparison test. One-sample t test was utilized for protein adsorption studies and morphometry. The level of significance was set at $P < 0.05$ for all experiments.

Results

Synthesis of hybrid hydrogels

ACPV hybrid hydrogel system was prepared by interpenetrating alginate and cellulose with the synthetic polymer PVA. ACPV1 and ACPV2 were prepared by varying the ratio of polymer constituents. The natural polymers used in ASPG system included alginate and starch along with the synthetic polymer PEG. The two subsets ASPG1 and ASPG2 were prepared by altering the constituent ratio. Divalent cation, Ca^{2+} was used as the crosslinking agent in all preparations. The percentage composition of alginate, cellulose and PVA were 30%, 20% and 50% respectively for ACPV1 and 46%, 15% and 39% respectively for ACPV2. ASPG1 system contained 17%, 23% and 58% of alginate, PEG, and starch respectively whereas ASPG2 contained 46%, 15% and 39% with respect to alginate, PEG, and starch (figure 1).

Surface functional groups

ATR spectra demonstrated similar peaks suggesting the existence of similar functional groups on hydrogel surface (figures 2A-2D). The broad peak around 3500cm^{-1} in all the four hydrogels represented -OH stretching vibrations contained in alginate, starch, CMC, PVA and PEG. The sharp peak 1700cm^{-1} attributed to the stretching vibrations of carbonyl groups contained in the alginate. The sharp peak around 1750cm^{-1} representing stretching vibrations of -COOH is due to the presence of alginate and CMC. Previous analysis of IR spectra of alginate as well as CMC has revealed this

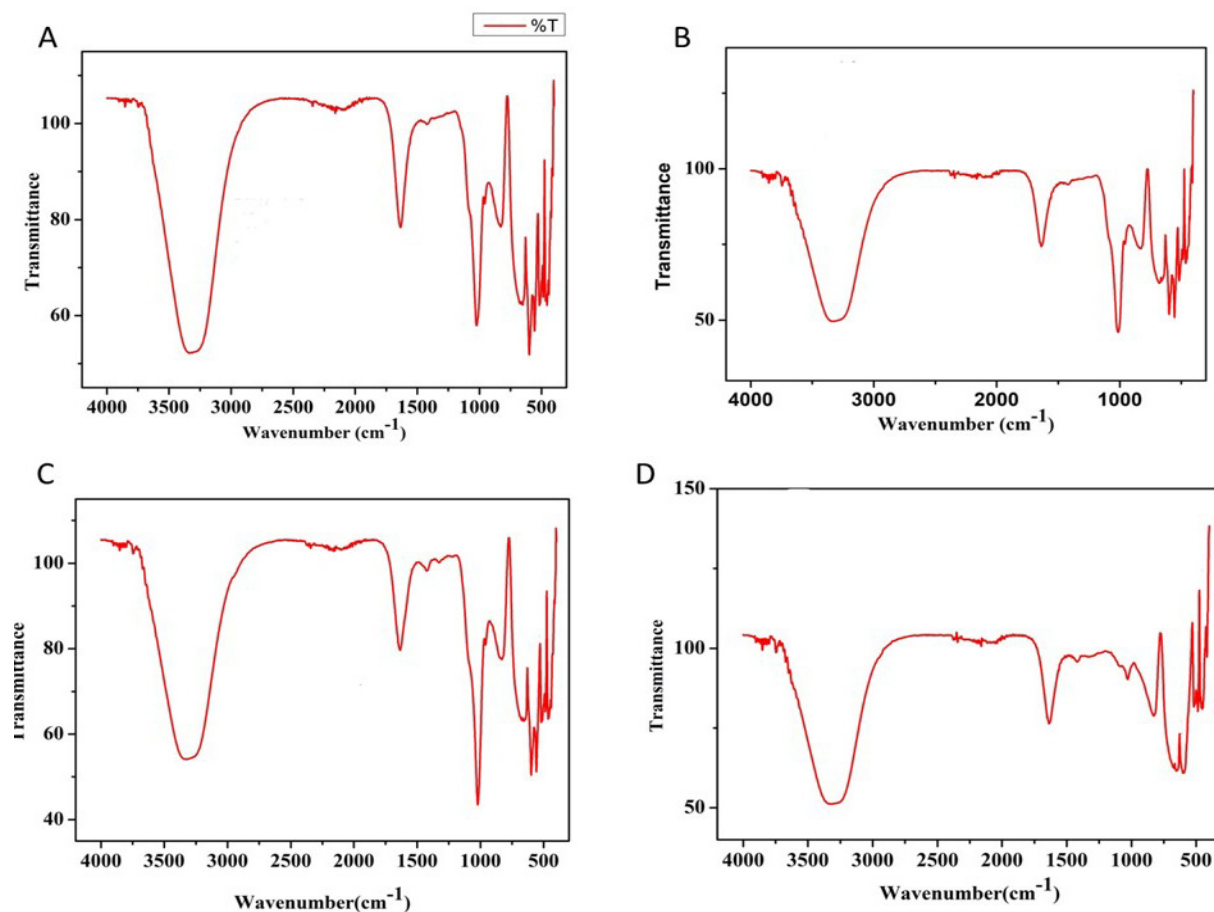


Figure 2: ATR spectra of hybrid hydrogels showing the peaks corresponding to characteristic functional groups: (A) ACPV1, (B) ACPV2, (C) ASPG1 and (D) ASPG2

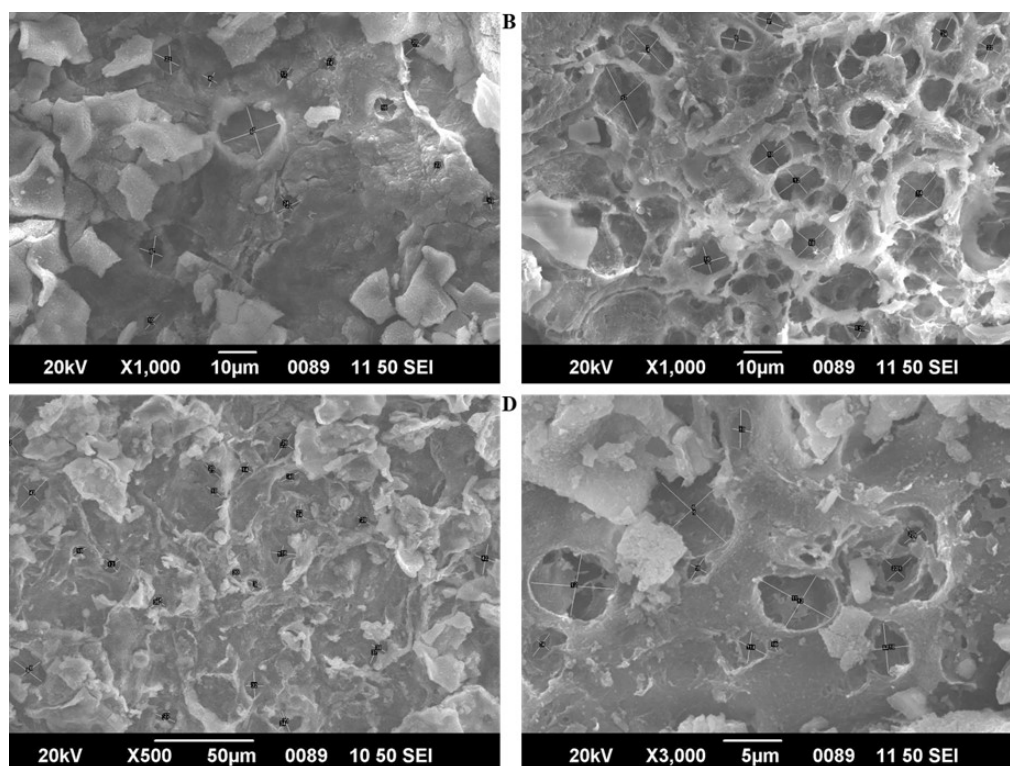


Figure 3: SEM images showing the pore distribution and size of hybrid hydrogel scaffolds: (A) ACPV1, (B) ACPV2, (C) ASPG1 and (D) ASPG2

peak around 1500 cm^{-1} . The sharp peak around 1000 cm^{-1} was due to the C-O-C stretching vibrations which represents the glycosidic bonds in the polysaccharides and in the PVA. Hence, the IR analysis suggests the presence of alginate, starch, CMC, PVA and PEG fractions in the surface of respective hydrogels.

Surface morphology

SEM imaging demonstrated the surface morphology and pore distribution of the hydrogels unveiling the porous morphology, pore density and pore interconnectivity (figures 3A-3D). ACPV2 and ASPG1 exhibited increased pore diameter when compared to ACPV1 and ASPG2 (table 1). However, there difference in pore length and breadth between ACPV1 ($P=0.0753$) and ACPV2

($P=0.1089$), ACPV1 ($P=0.3158$) and ASPG2 ($P=0.1348$) and ACPV2 ($P=0.7082$) and ASPG 1 ($P=0.9839$) were statistically not significant. Interestingly, the pore length and breadth in ACPV1 ($P=0.0017$) and ASPG1 ($P=0.0229$), ACPV2 ($P=0.0007$) and ASPG2 ($P=0.0002$), and ASPG1 ($P<0.0001$) and ASPG2 ($P<0.0001$) were statistically significant. Additionally, the pore aspect ratio of the hydrogels exhibited similar values and were statistically not significant suggesting the similar pore morphology (table 1).

Water profile

The EWC and water holding capacity of hybrid hydrogels displayed EWC $>79\%$ and swelling ratio >5 ; however, were statistically not significant among the groups except for the EWC between ASPG2

Table 1: Characterization of ACPV and ASPG hydrogels

Parameters	ACPV 1	ACPV2	ASPG1	ASPG2
Equilibrium water content	82.44 ± 4.58	88.40 ± 2.51	83.50 ± 5.09	78.57 ± 10.37
Swelling	6.00 ± 1.76	8.94 ± 2.21	6.43 ± 1.77	5.33 ± 2.08
Pore length	6.67 ± 3.31	10.35 ± 3.60	11.76 ± 4.20	4.03 ± 2.41
Pore breadth	5.20 ± 2.90	7.63 ± 2.70	7.96 ± 2.50	2.84 ± 1.72
Pore aspect ratio	1.34 ± 0.31	1.36 ± 0.20	1.48 ± 0.35	1.41 ± 0.29
Receding contact angle	44.44 ± 5.21	52.46 ± 4.40	45.14 ± 3.58	46.09 ± 7.94
Advancing contact angle	43.33 ± 4.51	48.88 ± 4.40	45.15 ± 4.8	47.2 ± 7.98
Tensile Strength	0.38 ± 0.06	0.47 ± 0.13	0.15 ± 0.07	0.91 ± 0.003
Young's Modulus	0.98 ± 0.15	1.51 ± 0.36	1.66 ± 0.37	4.50 ± 0.02
Protein adsorption (%)	41.05 ± 31.24	41.40 ± 19.60	75.42 ± 14.88	46.73 ± 26.83

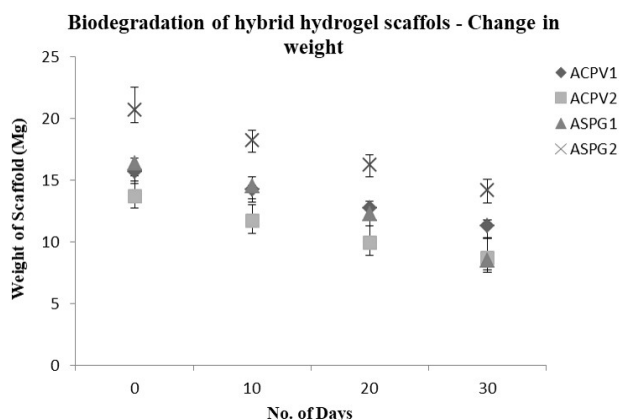


Figure 4: Biodegradation of hydrogels showing the progressive loss in dry weight

and ACPV2 ($P=0.0207$) (table 1). Interestingly, ACPV2 exhibited increased level of EWC (88.40 ± 2.51) suggesting the super absorbent nature. Overall, the four hydrogels exhibited similar water profile (table 1).

Tensile Strength

ASPG2 exhibited significantly greater tensile properties when compared with other three hydrogels. The tensile strength of ACPV1 ($P=0.7138$) was higher than ASPG1 and lower than ACPV2 ($P=0.1213$ respectively); however, the difference was statistically not significant. ASPG2 exhibited increased Young's modulus compared to the other three hydrogels; however, the increase was statistically not significant (table 1).

Table 2: Biodegradation of ACPV and ASPG hydrogels showing the alterations in TDS and pH

Hydrogel	TDS	PH
DAY 1		
ACPV1	3582 ± 0	7.10 ± 0
ACPV2	3582 ± 0	7.10 ± 0
ASPG1	3582 ± 0	7.10 ± 0
ASPG2	3582 ± 0	7.10 ± 0
DAY 10		
ACPV1	4609 ± 257	6.90 ± 0.03
ACPV2	4453 ± 198	6.90 ± 0.10
ASPG1	4343 ± 40	6.80 ± 0.05
ASPG2	4137 ± 1723	6.75 ± 0.07
DAY 20		
ACPV1	5010 ± 428	6.80 ± 0.015
ACPV2	5213 ± 328	6.85 ± 0.02
ASPG1	5429 ± 46	6.75 ± 0.05
ASPG2	5399 ± 519	6.80 ± 0.005
DAY 30		
ACPV1	5864 ± 596	7.08 ± 0.06
ACPV2	5691 ± 361	7.13 ± 0.02
ASPG1	6041 ± 462	7.03 ± 0.15
ASPG2	6006 ± 540	7.10 ± 0

Surface hydrophilicity

The advancing contact angles (ACA) of the hydrogels ranged between 43° to 48° whereas the receding contact angles (RCA) were between 44° and 52° suggesting the amphiphilic nature of the hydrogels; however, difference between ACA or RCA among the hydrogels were statistically not significant (table 1).

Biodegradation

Weight loss in ASPG1 hydrogel was minimal till day 10 when compared to the initial dry weight ($P>0.05$) followed by significant increase in weight loss as observed in days 20 and 30. A significant weight loss was shown by ASPG2 hydrogels in days 10 and 20; however, the weight loss after 20 days was statistically not significant ($p>0.05$). Additionally, the trend for weight loss was similar for ACPV hydrogels as minimal weight loss was observed in both hydrogels till day 10 and was significantly increased in day 30 for both hydrogels ($p<0.05$) (figure 4). TDS showed gradual increase throughout the course of the experiment which was significantly higher in day 30 when compared with day 1 ($p<0.05$) for all the hydrogels (table 2). The pH was slightly acidic during the initial phase and turned to neutral or slightly alkaline on day 30. The initial and final pH of the medium was statistically insignificant ($p>0.05$). However, the variations were significant on day 10 and 20 when compared with day 1 for all the scaffolds ($p<0.05$) (table 2).

Protein adsorption

The total proteins adsorbed on hydrogel surfaces were 41.05%, 49.4%, 75.4% and 46.7% for ACPV1, ACPV2, ASPG1 and ASPG2 respectively (table 1). The level of protein adsorption was significantly higher ($P=0.0466$) ASPG1 hydrogel; however, was statistically not significant in ACPV1, ACPV2 and ASPG2 ($P=0.2283$, $P=0.1036$ and $P=0.0752$ respectively). SDS PAGE analysis revealed predominant albumin adsorption onto the surface of all hydrogels. The relative albumin adsorption was 60.33%, 53.75%, 50.17%, and 56.25% respectively for ACPV1, ACPV2, ASPG1 and ASPG2 where plasma control presented 80.47% (figure 5).

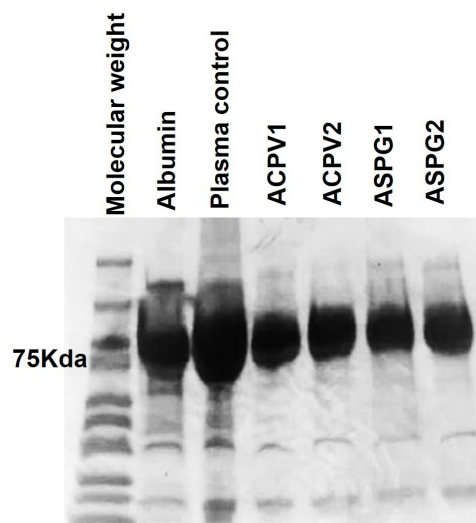


Figure 5: SDS-PAGE analysis of hybrid hydrogels after treatment with plasma demonstrating the conspicuous band corresponding to adsorption of albumin in comparison with control plasma and bovine serum albumin

Cytocompatibility

The H9c2 cells on contact with all the hydrogels retained their normal spindle morphology and deviation from the normal morphology was completely absent suggesting the non-toxic nature of the hydrogels revealing their biocompatibility (**figure 6A-6E**). MTT assay using H9c2 cells cultured with hydrogel extract revealed the viability 82%, 105.37%, 89.12% and 104.75% for ACPV1, ACPV2, ASPG1 and ASPG2 respectively when compared with the control (**figure 6F**). The difference in viability was statistically not significant among the groups ($p > 0.05$).

Antimicrobial Efficiency

ACPV and ASPG hydrogel subsets incorporated with different concentrations of amikacin and vancomycin exhibited significant increase in zone of inhibition when compared with the control (**table 3, figure 7**). Statistically significant increase in the zone of inhibition was observed between ACPV1(5_{Ami}) and ASPG1(5_{Ami}). However, the variations in zone of inhibition were statistically not significant for the other hydrogels incorporated with 5, 10 and 20 μ l of amikacin ($p > 0.05$). In addition, ACPV1(5_{Vanc}) showed significant difference ($p < 0.05$) between ACPV2(5_{Vanc}) and ASPG1(5_{Vanc}); however, was statistically not significant compared to ACPV1(5_{Vanc}) and ASPG2(5_{Vanc}) ($p > 0.05$). Similarly, ACPV2(5_{Vanc}) exhibited significant increase than ASPG1(5_{Vanc}) and ASPG2(5_{Vanc}) ($p < 0.05$); however, ASPG1(5_{Vanc}) and ASPG2(5_{Vanc}) displayed similar trend. ACPV1(10_{Vanc}) and ACPV2(10_{Vanc}) exhibited significant increase in zone of inhibition when compared with ASPG1(10_{Vanc}) and ASPG2(10_{Vanc}) ($p < 0.05$); however, the zone of inhibition among ACPV1(10_{Vanc}) and ACPV2(10_{Vanc}) and ASPG1(10_{Vanc}) and ASPG2(10_{Vanc}) were statistically not significant ($p > 0.05$). Also, non-significant variation was observed for any of the hydrogels incorporated with 20 μ l of vancomycin ($p > 0.05$).

Discussions

The panel of hydrogel scaffolds synthesized in this study were decorated with ample functional moieties contributing to the biological performance for cardiac applications. Evidently, IR analysis revealed the presence of abundant hydrophilic functional groups such as hydroxyl, carboxyl, and carbonyl on scaffold surface. The sharp peak near 1000 cm^{-1} which indicated C-O-C stretching in all hydrogels confirms the presence of polysaccharides as this vibration is characteristic for the glycosidic bonds in polysaccharides. Also, the weakening of C-O stretching vibration in ASPG3 reflects increased hydrogen bond formation between glycosidic oxygen and -OH groups indicative of a hydrophilic surface stabilized by hydrogen bonding. Importantly, the presence of hydrophilic moieties on scaffold surface greatly enhances the water absorption capacity of the hydrogels by promoting hydrogen bonding with water molecules [12]. Moreover, the abundance of surface functional moieties provides opportunities for chemical immobilization of biomolecules and other growth factors for improving cell adhesion and maturation [13].

The growth and survival of cells seeded in tissue engineering scaffolds is greatly influenced by its porosity, pore density, and pore size as the cell adhesion, migration, proliferation, differentiation, and cell-cell interaction are dependent on pore architecture [7]. Furthermore, the efficiency of nutrient trafficking and removal of metabolic exhaust is greatly influenced by pore morphology and density. The surface morphometry reveals that the four scaffolds displays pore architecture with pore length ranging between 4 μm to 12 μm and pore breadth ranging between 3 μm to 8 μm corresponding to the micro porous architecture an ideal tissue engineering scaffold [14]. Multiple reports conclude that microporous scaffold architecture improves cell migration,

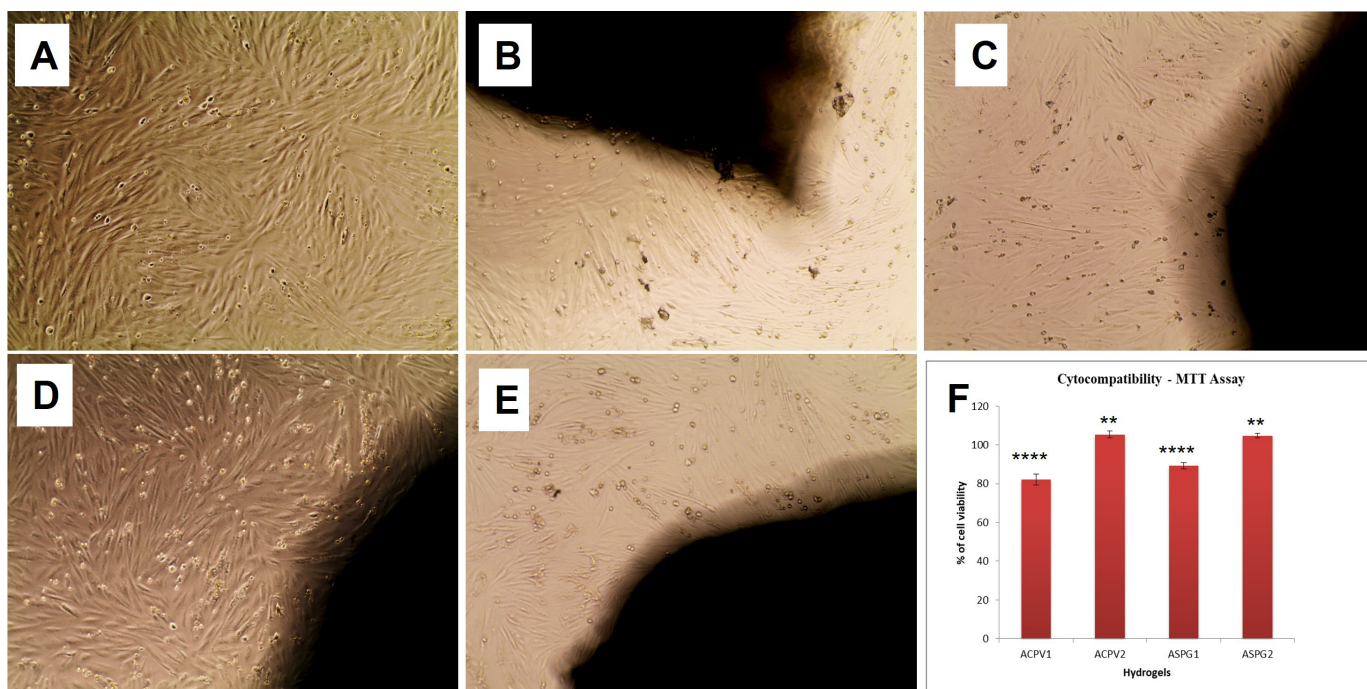


Figure 6: Direct contact assay of hybrid hydrogels using H9c2 cells showing the biocompatibility: (A) Control, (B) ACPV1, (C) ACPV2, (D) ASPG1, and (E) ASPG2. (F) MTT assay using hydrogel extract treated H9c2 cells showing increased cell viability

Table 3: Antimicrobial efficiency of Amikacin and Vancomycin loaded hydrogels revealing the zone of inhibition

Hydrogel	Amikacin			Vancomycin		
	5 µg/mL	10 µg/mL	20 µg/mL	5 µg/mL	10 µg/mL	20 µg/mL
ACPV1	2.37 ± 0.05	2.47 ± 0.05	2.73 ± 0.11	2.53 ± 0.11	3.03 ± 0.05	3.16 ± 0.05
ACPV2	2.30 ± 0.10	2.53 ± 0.11	2.87 ± 0.05	2.87 ± 0.05	3.20 ± 0.20	3.06 ± 0.05
ASPG1	2.06 ± 0.05	2.53 ± 0.05	2.66 ± 0.05	2.20 ± 0.10	2.63 ± 0.05	2.96 ± 0.15
ASPG2	2.23 ± 0.11	2.47 ± 0.11	2.76 ± 0.05	2.30 ± 0.20	2.63 ± 0.11	3.06 ± 0.05

attachment, and anchorage dependent cell to cell communication [15]. Moreover, neovascularization, fibroblast infiltration and cell survival are optimum in scaffolds with pore size range of 5 µm to 15 µm [16]. Interestingly, human embryonic stem cells (hESCs) demonstrated appreciable attachment on membranes with pore size ranging between 3 to 8 µm [17]. Additionally, poly(ethylene glycol) scaffolds with pore size of 12µm promoted better migration of mesenchymal stem cells (MSCs) [18]. These observations suggest that ASPG and ACPV hydrogels pose immense potential to support the growth of multiple cell types onto the interstices.

Water content of the hydrogels is the function of osmotic driving forces and the cohesive force exerted by the polymer network [19]. Both ACPV and ASPG hydrogel subsets demonstrated an EWC greater than 80% and swelling ratio between 5-7 attributing to ample hydrophilic functional groups and porosity as evidenced by IR analysis and SEM respectively. The superior water content is beneficial for in trafficking of metabolite and mass transfer. In addition, the increased water level relaxes the polymer chains to increase the surface area and pore size facilitating the cell survival and performance. [20]. Furthermore, the increased water content prevents dehydration thereby accelerating the wound healing responses [21]. Hence, the superior water content in the hydrogels favour for successful CTE.

Biodegradation of hybrid hydrogels were studied using PBS buffer for 30 days where all the hydrogels maintained their structure for the initial three weeks period followed by slower withering. ACPV1 and ACPV2 hydrogels lost 72% and 63.5% of their dry weight respectively after 30 days study. Similarly, ASPG1 and ASPG 2 hydrogels lost 52% and 81.6% of their dry weight respectively. TDS were increased in a time dependent fashion owing to the erosion of ions and other solid particles from the hydrogel surfaces confirming the degradation. Crosslinking of the polymer chain with calcium is affected by the formation of covalent bond between calcium ions and guluronic acid residues in the G block of alginate chains forming the characteristic egg box structure [8]. Interactions of the crosslinked alginate with monovalent ions such as sodium and potassium results in the replacement of calcium ions with monovalent ions result in the collapse of egg box leading to gel-sol transition and subsequent weakening the hydrogel [22]. Additionally, the slight drop in pH suggests the release of mild acidic degradation products which elicits minimal physiological responses owing to the efficient buffering capacity of circulating fluids [8].

Mechanical properties of the CTE scaffolds influence the cell adhesion, cell signalling pathways, angiogenesis, and neo-tissue formation. The superior tensile properties of ACPV2 and ASPG2 hydrogels reflect the increased crosslinking density owing to the increased level of alginate. The Youngs modulus of the hydrogels ranged between 1 to 4 MPa which has been reported to be ideal for soft tissue engineering. For instance, the electrospun polyester ether(urethane urea) scaffold with an elastic modulus ranging between 1-2 MPa was loaded with adeno associated viral genes and implanted into left ventricle of rat resulted in improved LV function owing to the mechanical properties of the scaffold [23] Interestingly, the ACPV and ASPG hydrogels are mechanocompatible for CTE allowing the tuneable mechanical properties by manipulating the crosslinking density by divalent cations.

The contact angle value of all the scaffolds falls within the range of amphiphilicity which is crucial in enhancing cell adhesion and

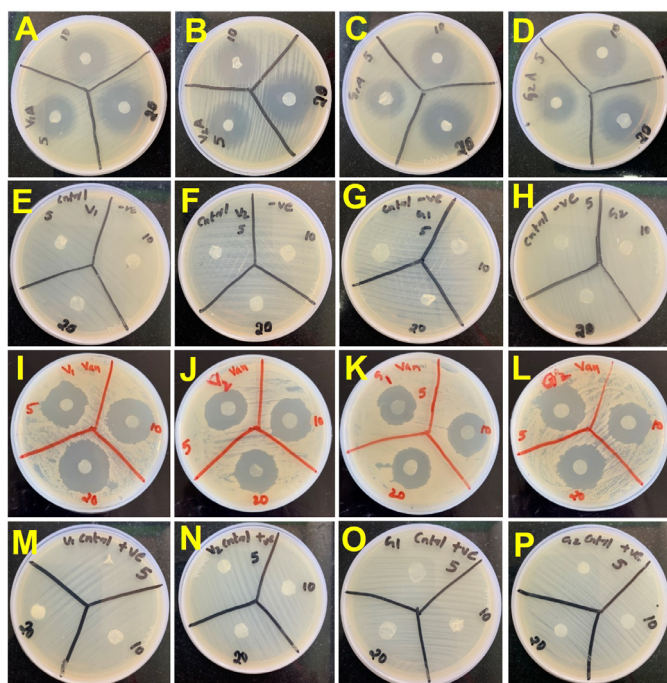


Figure 7: Antibiotic releasing efficiency of ACPV and ASPG hybrid hydrogel scaffolds (A) ASPG1 incorporated with different concentrations of amikacin (B) ACPV2 incorporated with different concentrations of amikacin (C) ASPG1 incorporated with different concentrations of amikacin (D) ASPG2 incorporated with different concentrations of amikacin (E) ACPV1 control for amikacin (F) ACPV2 control for amikacin (G) ASPG1 control for amikacin (H) ASPG2 control for amikacin (I) ACPV1 incorporated with different concentrations of vancomycin (J) ACPV2 incorporated with different concentrations of vancomycin (K) ASPG1 incorporated with different concentrations of vancomycin (L) ASPG2 incorporated with different concentrations of vancomycin (M) ACPV1 control for vancomycin (N) ACPV2 control for vancomycin (O) ASPG1 control for vancomycin (P) ASPG2 control for vancomycin.

proliferation [24]. The hydrophilicity of ACPV and ASPG hybrid hydrogel subsets owe to the presence of hydrophilic functional groups such as -COOH, and -OH on hydrogel surfaces as indicated by IR analysis. However, extremely hydrophilic, or hydrophobic surfaces are less favourable for cell adhesion whereas moderately wettable surfaces are optimal for cell adhesion and proliferation [25–27]. Hence, the amphiphilic nature of the hydrogels supports protein adsorption and the attachment, proliferation and migration of cells which is necessary for the integration of CTE implants.

The *in vivo* biocompatibility of a scaffold is greatly driven by the type and amount of protein adsorbed on the surface [28]. Post-implantation, cellular attachment on any scaffold surface is largely affected and regulated by the adsorbed protein layer as scaffold-protein interaction occurs prior to cell infiltration/adhesion. Protein adsorption on a hydrophobic scaffold surface is largely governed by hydrophobic interactions whereas on a hydrophilic surface favour electrostatic force. Interestingly, the hydrophilic surfaces retain confirmation of adsorbed proteins whereas hydrophobic results in structural deformities [29]. The adherence of albumin in the surface of scaffold results in smoothness and a rough surface is detrimental as the RBC membrane rupture occurs upon encountering circulation resulting in haemolysis, and activation and aggregation of platelets leading to thrombosis [30]. Importantly, adsorption of plasma albumin prevents unfavourable cell-scaffold interactions contributing to hemocompatibility and created favourable environment for the infiltrating cells [31]. Additionally, albumin binding on scaffold surface prevents the adsorption of fibrinogen preventing thrombosis and inflammation [32]. Also, there are reports on using albumin itself as biomaterial for fabricating tissue engineering scaffolds due to its exceptional biocompatibility [33]. In the present study, ACPV1, ACPV2 and ASPG2 exhibited superior adsorption of albumin from the serum whereas ASPG1 demonstrated a significantly higher adsorption (75%) which is attributed to the microporous and amphiphilic nature of scaffolds [34].

Importantly, the hydrogels are biocompatible, and the degradation products are non-toxic to the cells. Direct contact revealed the absence of morphological changes in H9c2 cells demonstrating the cytocompatibility of ACPV and ASPG hydrogels. Hence, the ACPV and ASPG hydrogel systems represent biocompatible templates for CTE applications. However, the translational challenges in tissue engineering strategy including infection following the invasive procedures are alarming [35]. Such infections result in unpredictable aftermaths including sustained inflammatory responses leading to treatment failure. Oral/intravenous administration of antibiotics help to prevent infections; however, limited bioavailability and bio-retention of antibiotics at the surgery site, and antibiotic resistance are challenging. In addition, the higher doses of antibiotics cause off target side effects including liver damage, and kidney disorders. A possible alternative to treat implant-driven infection is to incorporate antibiotics into scaffolds aiding in a sustained and localized delivery of antibiotics and eliminates the chances of systemic toxicity. In the present study, all the hydrogels incorporated with different concentrations of amikacin and vancomycin demonstrated excellent inhibition of bacterial proliferation. The exceptional hydrophilicity of the ACPV and ASPG enabled the loading/release of antibiotics by simple diffusion. Despite the establishment of the proof of the concept, the efficiency cell performance in antibiotic loaded ACPV and ASPG hydrogels warrants further optimization. However, our approach opens novel translational avenues for the management of nosocomial infections following CTE implantation.

Conclusion

In the present study, two sets of hybrid hydrogel viz ACPVs and ASPGs were prepared for cardiac tissue engineering and evaluated for physical and cytocompatible properties. The results showed that all the scaffolds were biodegradable with appreciable mechanical strength, optimum surface features, and water holding capacity and evoked no toxicological responses towards seeded cells. All the scaffolds were found to be promising for cardiac tissue engineering.

Acknowledgement: SKC is grateful to the staffs and scholars of KKTMGC and Christ College for their support to complete this study.

Conflict of Interest: All the authors have read the manuscript and declare no conflict of interest. No writing assistance was utilized in the production of this manuscript.

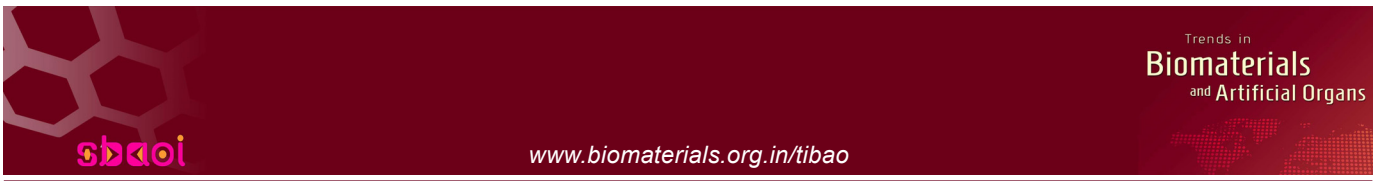
Funding: The authors did not receive any funding for this study.

Availability of data and materials: Data with the raw counts matrices and annotation are available upon request from the authors through proper channels.

References

- Majid Q.A., Fricker A.T.R., Gregory D.A., et al., Natural Biomaterials for Cardiac Tissue Engineering: A Highly Biocompatible Solution. *Front Cardiovasc Med*, 7, 554597 (2020).
- Virani S.S., Alonso A., Aparicio H.J., et al., Heart Disease and Stroke Statistics-2021 Update: A Report from the American Heart Association. *Circulation*, 143, e254–e743 (2021).
- Arjmand B., Abedi M., Arabi M., et al., Regenerative Medicine for the Treatment of Ischemic Heart Disease; Status and Future Perspectives. *Front Cell Dev Biol*, 9, 704903 (2021).
- Ikada Y. Challenges in tissue engineering, *J R Soc Interface* 3, 589–601 (2006).
- Neltner T.G., Kulkarni N.R., Alger H.M., et al., Navigating the U.S. Food Additive Regulatory Program. *Compr Rev Food Sci Food Saf* 10, 342–368 (2011).
- Hutmacher D.W., Scaffold design and fabrication technologies for engineering tissues - state of the art and future perspectives. *J Biomater Sci Polym Ed*, 12, 107–124 (2001).
- Finosh G.T., Jayabalan M., Regenerative therapy and tissue engineering for the treatment of end-stage cardiac failure: new developments and challenges. *Biomater*, 2, 1–14 (2012).
- Gnanaprakasam Thankam F., Muthu J., Sankar V., Kozhiparambil Gopal R., Growth and survival of cells in biosynthetic poly vinyl alcohol–alginate IPN hydrogels for cardiac applications. *Colloids Surf B Biointerfaces*, 107, 137–145 (2013).
- Gnanaprakasam Thankam F., Muthu J., Alginate based hybrid copolymer hydrogels—Influence of pore morphology on cell-material interaction. *Carbohydr Polym*, 112, 235–244 (2014).
- Finosh G.T., Jayabalan M., Vandana S., Raghu K.G., Hybrid alginate-polyester bimodal network hydrogel for tissue engineering—Influence of structured water on long-term cellular growth. *Colloids Surf B Biointerfaces*, 135, 855–864 (2015).
- Thankam F.G., Diaz C., Chandra I., et al., Hybrid interpenetrating hydrogel network favoring the bidirectional migration of tenocytes for rotator cuff tendon regeneration. *J Biomed Mater Res B Appl Biomater*, 110, 467–477 (2022).
- Singh M.R., Patel S., Singh D., Natural polymer-based hydrogels as scaffolds for tissue engineering. In: *Nanobiomaterials in Soft Tissue Engineering*. Elsevier, pp 231–260 (2016).
- Niemczyk-Soczynska B., Grady A., Sajkiewicz P., Hydrophilic Surface Functionalization of Electrospun Nanofibrous Scaffolds in Tissue Engineering. *Polymers*, 12, 2636 (2020).
- Vagaská B., Bacáková L., Filová E., Balík K., Osteogenic cells on bio-inspired materials for bone tissue engineering. *Physiol Res*, 59, 309–322 (2010).
- Bru•auskait I., Bironait D., Bagdonas E., Bernotien E., Scaffolds and cells for tissue regeneration: different scaffold pore sizes-different cell effects. *Cytotechnology*, 68, 355–369 (2016).
- Thankam F.G., Muthu J., Influence of physical and mechanical properties

- of amphiphilic biosynthetic hydrogels on long-term cell viability. *J Mech Behav Biomed Mater*, 35, 111–122 (2014).
17. Kim S., Ahn S.E., Lee J.H., et al., A novel culture technique for human embryonic stem cells using porous membranes. *Stem Cells Dayt Ohio*, 25, 2601–2609 (2014).
 18. Peyton S.R., Kalcioğlu Z.I., Cohen J.C., et al., Marrow-Derived stem cell motility in 3D synthetic scaffold is governed by geometry along with adhesivity and stiffness. *Biotechnol Bioeng*, 108, 1181–1193 (2011).
 19. El-Sherbiny I.M., Yacoub M.H., Hydrogel scaffolds for tissue engineering: Progress and challenges. *Glob Cardiol Sci Pract*, 2013, 316–342 (2013).
 20. Coenen A.M.J., Bernaerts K.V., Harings J.A.W., et al., Elastic materials for tissue engineering applications: Natural, synthetic, and hybrid polymers. *Acta Biomater*, 79, 60–82 (2018).
 21. Saravanan S., Chawla A., Vairamani M., et al., Scaffolds containing chitosan, gelatin and graphene oxide for bone tissue regeneration in vitro and in vivo. *Int J Biol Macromol*, 104, 1975–1985 (2017).
 22. Kurowiak J., Kaczmarek-Pawelska A., Mackiewicz A.G., Bedzinski R., Analysis of the Degradation Process of Alginate-Based Hydrogels in Artificial Urine for Use as a Bioresorbable Material in the Treatment of Urethral Injuries. *Processes*, 8, 304 (2020).
 23. Gu X., Matsumura Y., Tang Y., et al., Sustained viral gene delivery from a micro-fibrous, elastomeric cardiac patch to the ischemic rat heart. *Biomaterials*, 133, 132–143 (2017).
 24. Ghorbani F., Sahranavard M., Mousavi Nejad Z., et al., Surface Functionalization of Three Dimensional-Printed Polycaprolactone-Bioactive Glass Scaffolds by Grafting GelMA Under UV Irradiation. *Front Mater*, 7, 528590 (2020).
 25. Lin G., Zhang X., Kumar S.R., Mark J.E., Improved Hydrophilicity from Poly(ethylene glycol) in Amphiphilic Conetworks with Poly(dimethylsiloxane). *Silicon*, 1, 173–181 (2009).
 26. van Wachem P.B., Hogt A.H., Beugeling T., et al., Adhesion of cultured human endothelial cells onto methacrylate polymers with varying surface wettability and charge. *Biomaterials* 8, 323–328 (1987).
 27. van Wachem P.B., Beugeling T., Feijen J., et al., Interaction of cultured human endothelial cells with polymeric surfaces of different wettabilities. *Biomaterials*, 6, 403–408 (1985).
 28. Yu Q., Chen H., Interaction of switchable biomaterials surfaces with proteins. In, *Switchable and Responsive Surfaces and Materials for Biomedical Applications*. Elsevier, pp 167–188 (2015).
 29. Recek N., Mozetic M., Jaganjac M., et al., Adsorption of Proteins and Cell Adhesion to Plasma Treated Polymer Substrates. *Int J Polym Mater Polym Biomater*, 63, 685–691 (2014).
 30. Maruyama O., Nishida M., Yamane T., et al., Hemolysis resulting from surface roughness under shear flow conditions using a rotational shear stressor. *Artif Organs*, 30, 365–370 (2006).
 31. Gnanaprakasam Thankam F., Muthu J., Influence of plasma protein–hydrogel interaction moderated by absorption of water on long-term cell viability in amphiphilic biosynthetic hydrogels. *RSC Adv*, 3, 24509 (2013).
 32. Radhakrishnan A., Jose G.M., Kurup M., PEG-penetrated chitosan–alginate co-polysaccharide-based partially and fully cross-linked hydrogels as ECM mimic for tissue engineering applications. *Prog Biomater*, 4, 101–112 (2015).
 33. Li P.S., Liang Lee I., Yu W.L. et al., A Novel Albumin-Based Tissue Scaffold for Autogenic Tissue Engineering Applications. *Sci Rep* 4, 5600 (2015).
 34. Zhang K., Fan Y., Dunne N., Li X., Effect of microporosity on scaffolds for bone tissue engineering. *Regen Biomater* 5, 115–124 (2018).
 35. Kandi V., Vadakedath S., Implant-Associated Infections: A Review of the Safety of Cardiac Implants. *Cureus* 12, e12267 (2020).



Original Article

A Novel Use of Tissue Conditioner as a Local Drug Delivery Medium for Microbial Control around Dental Implants: *In Vitro* Release Studies of Antibiotics and Curcumin

Vibha Shetty¹, R. Deveswaran², Beena Antony³, Shrestha Shetty⁴, K. Ranganath⁵

¹Department of Prosthodontics, ²Department of Oral Surgery, Faculty of Dental Sciences, ³Department of Pharmaceutics, Faculty of Pharmacy, M.S. Ramaiah University of Applied Sciences, Bangalore, India

³Professor, Department of Microbiology, Fr Muller Medical College & Research Centre, Mangalore, India.

⁴Department of Public Health Dentistry, AJ institute of Dental Sciences, Mangalore, India

Received: 1 June 2023

Accepted: 29 June 2023

Published online: 30 June 2023

Keywords: amoxicillin, metronidazole, curcumin, tissue conditioner, peptostreptococcus, fusobacterium, porphyromonas

Microbe mediated inflammation is one of the common causes of peri-implantitis soon after surgery. A medium that delivers antibiotics locally in a sustained manner may mitigate the common side effects of the antibiotic especially gastric irritation. To determine the effectiveness of tissue conditioner as a carrying medium to deliver antibiotics and curcumin as an alternative at an implant surgical site post operatively, retaining the properties of tissue conditioner. The antibiotics amoxicillin-clavulonic acid and metronidazole, and the antimicrobial agent curcumin are incorporated into tissue conditioner (TC) at various concentrations. The antimicrobial properties are studied using antimicrobial sensitivity tests against *Peptostreptococcus*, *Fusobacterium*, and *Porphyromonas*. In addition, the flow properties and viscosity of selected TC-antimicrobial combinations are analyzed. Relevant statistical analyses are carried out to assess the data. The tissue conditioner (TC) mixed with antibiotic and curcumin separately, showed a zone of inhibition that was greater than the control used. This showed that there was elution from the tissue conditioner mixed with the chosen drugs into artificial saliva. The materials mixed in 1:1 ratio of metronidazole and different ratios of curcumin each with TC showed spreadability and viscosity similar to that of control. Differential Scanning Calorimetry showed no interaction between the drugs and tissue conditioner. Tissue conditioner can be used as an effective medium to carry antibiotics or curcumin with positive elution into artificial saliva. Treatment strategies could involve targeted pharmaceutical approach with drugs delivered locally.

© (2023) Society for Biomaterials & Artificial Organs #20066923

Introduction

Tooth loss due to periodontitis or dental caries is a debilitating disease that has been successfully treated with a predictable treatment option of dental implant supported restorations. These restorations provide rehabilitation solutions for patients with a few or all missing teeth. Yet the procedure is prone to failure. Early failure is determined by microbial contamination, improper case selection, poor surgical protocols, and habits, whereas delayed failures are caused by systemic conditions, lack of oral hygiene maintenance, occlusal overload and prosthetic defects. The human mouth is the habitat of over 750 aerobic and anaerobic microbes, that have been identified, genetically mapped and named by the

human oral microbiome project [1]. Therefore, the chances are high for the immediate post operative infection, which can lead to peri-implantitis and subsequent loss of implant.

Microbial colonization of the surgical site starts within a few hours to weeks after placing implants [2]. The microbial flora in mouth contain both aerobic and anaerobic bacteria, but the latter have largely been implicated in periodontitis and peri-implantitis [3]. Minimizing impact of microbial colonization has been achieved with pre-operative or post-operative antibiotic coverage [4]. Oral administration, namely the *per oral* (PO) route of antibiotics is associated with several side effects including gastrointestinal disturbances causing nausea, vomiting, diarrhea, pain and other symptoms [5]. Lack of patient compliance to complete the prescribed course is an equal challenge. Antibiotics are absorbed best through the intravenous route. However, antibiotics like

* Corresponding author

E-mail address: vibhashetty.pr.ds@msruas.ac.in (Prof. Vibha Shetty, MDS)

amoxicillin and metronidazole have good bioavailability even when administered through the PO route and are best absorbed through the small intestine. The addition of clavulanic acid to amoxicillin enhances the absorption of the antibiotic. In addition, due to the mode of normal distribution of antibiotics through the plasma and final delivery to the desired area of application, a large dose of antibiotic must be administered. This leads to the problem of high antibiotic resistance especially in the south Asian region [6]. Alternative therapeutics like curcumin have been explored to avoid the side effects of antibiotics [7].

Localized drug delivery has been identified as a good strategy to deliver higher doses to the site, rather than losing a large part of the administered drug to metabolism [8]. This could be presumably adopted to control the peri-implantitis, with two-fold advantage. A customized therapy is possible and the use of orally consumed broad spectrum antibiotics could be minimized, if not fully avoided. Currently, topically applicable antibiotic containing gels are available for local drug delivery in mouth, but they get washed away by saliva and demand constant re-application. For sustained drug delivery, it requires the use of a material that will remain *in situ* for a period of five to seven days, the normal duration of an antibiotic course or the time required for primary closure of the surgical site. A suitable carrying medium for the sustained delivery of antibiotic could solve the problem.

The present work proposes tissue conditioner (TC) or soft-liner materials as a potential media for sustained drug delivery to prevent or control peri-implantitis. Polymer based tissue conditioners are used often in Prosthodontics as a soft liner under dentures [9]. They have also been used as a medium to carry anti-fungal drugs to combat the problem of denture stomatitis [10]. Also, they are used to condition inflamed tissues when used with a denture. The use of tissue conditioner has not been assessed yet, as a medium to carry antibiotics to enable local drug delivery at an intra oral surgical site. It is worthwhile to explore the viability of tissue conditioner as a carrying medium of antibiotics and bacteriostatic agents like curcumin. Along with the good release characteristics ensuring the bioavailability of the drug, the addition of the drug must not change the well accepted handling properties of tissue conditioner.

The study is designed to determine the effectiveness of tissue conditioner (TC) as an alternative carrying medium to deliver antibiotics and curcumin at the implant surgical site post operatively, without changing its essential properties. Amoxicillin and metronidazole are commonly prescribed antibiotics as they are well absorbed through the PO route and administration with food or in a fasting state does not impact the absorption of either drug. The absorption of the drug is largely through the small intestine and has shown very good bioavailability [11]. Curcumin, on the other hand is proven to be a good anti-oxidant, anti-inflammatory, anti-bacterial, and anti-fungal agent [12-14].

The main objective of this study is to determine the release of amoxicillin-clavulonic acid, metronidazole and curcumin when incorporated in a tissue conditioner and the effectiveness against three common anaerobic microbes inhabiting the oral cavity. The tissue conditioner carrying effective ratios of antimicrobial agents were tested for physical properties like spreadability and viscosity, and the effectiveness of drug release was tested through the zone of inhibition method against *Peptostreptococcus*, *Fusobacterium*, and *Porphyromonas*. The compatibility of each additive with tissue conditioner is assessed using Differential Scanning Calorimetry. Bare polymer-based TC, a well-accepted material in Prosthodontics, is taken as the control material. The potential outcome is the

possibility of using TC to control peri-implantitis, when applied along with an immediate post-surgical denture.

Materials and Methods

Polymethyl methacrylate (PMMA) based tissue conditioner (GC Soft-Liner, GC Europe N.V) was used as the Tissue Conditioner (TC) material to be tested as the drug carrying medium. The antibiotics chosen were Amoxicillin and Potassium Clavulanate (Co-amoxiclav; MOXCLAV DS, 457 mg manufactured by Sun Pharmaceutical India Ltd, Dewas, M.P., India), Pure metronidazole powder (Astitva Chemicals, Valsad, Gujarat, India), and pure medical grade curcumin (Sami Labs, Peenya, Bangalore, Karnataka, India).

Sample preparation and handling

The test samples were prepared by mixing co-amoxiclav, metronidazole and curcumin with the powder part of the tissue conditioner (TC) in different ratios of 1:1, 1:2, 1:3, 1:4 and 1:5 by weight. The powders were weighed on a digital weighing machine, added as per the proportioned required and mixed thoroughly using mortar-pestle to get an even distribution. The sample discs of respective TC-antimicrobial agent combinations were made by mixing the powder and liquid components according to manufacturer's instructions (at a ratio 1.0:1.1, thoroughly stirred for 45 secs). Samples for the microbiological study were prepared as discs of 6mm diameter and 2 mm height by filling the mixed tissue conditioner in custom made acrylic molds (figure 1). Elutes of the samples of drug loaded TC and control TC were taken in triplicate by placing the discs in 2ml artificial saliva for 6 hours in test tubes.

Antibiotic sensitivity test

Disc diffusion technique was used to evaluate the antibiotic sensitivity to TC samples incorporated with antimicrobial agents. A control plate was used for each of the microbes with control discs of a β -lactamase inhibitor (30 μ g/disc), metronidazole (5 μ g/disc), and curcumin (50 μ g/disc). The elutes of TC-co-amoxiclav, TC-metronidazole and TC-curcumin discs were prepared in triplicate and collected aseptically. The samples were randomized and blinded with colour coding. The same was received by the second investigator who was blinded to the concentration and carried out the microbiological study.

Sterile filter paper discs were saturated with the elute samples and were placed over the Brucella blood agar plates inoculated with *Peptostreptococcus*, *Porphyromonas* and *Fusobacterium*. The antimicrobial activity was assessed by measuring the zone of inhibition (ZOI) around the sample discs.

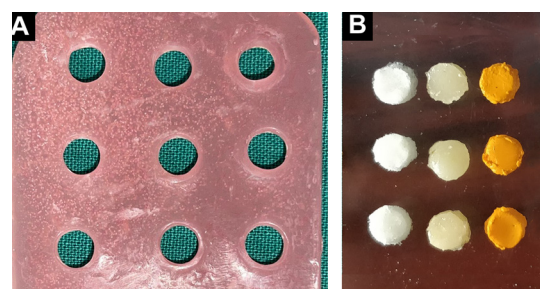


Figure 1: Sample preparation for microbiological study. Acrylic mold (A) and one set of sample discs (B)

The one-way analysis of variance (ANOVA) was used to determine any statistically significant differences between the means of each of the pharmaceutical agents used to create a zone of inhibition (dependent variable) measured in millimeters. The post hoc Tukey's test provides a deeper insight into the comparison between specific groups. A confidence interval of 95 % and error rate of 0.05 was set and a difference below 0.05 was considered to be statistically significant.

Testing physical properties

The characterization of relevant physical properties of the tissue conditioner was carried out to understand the potential changes in the relevant physical properties of tissue conditioner with the incorporation of antibiotics and antimicrobial agents.

(i) *Spreadability*: The spreadability testing apparatus contained two glass slides placed one over another on a horizontal platform. The lower glass plate is fixed to the platform and the upper one is free to slide over it. The test material (freshly mixed tissue conditioner) is placed in between the glass plates and the upper glass plate is pulled horizontally using a string running over a pulley fixed to the edge of the platform and loaded with a fixed weight. The time taken by the glass slide to travel the distance of 6 cm is measured with the help of a stop clock [15].

Combinations of the tissue conditioner loaded with Co-amoxiclav in the proportions of 4:1 and 5:1, metronidazole in the proportions of 1:1 and 4:1 and curcumin in the proportions of 1:1, 3:1 and 4:1 were taken for the test, wherein the bare tissue conditioner (TC) served as control. In each case, 0.5g of sample was put in between the glass slides kept in aligned position and the upper slide was pulled horizontally with a fixed weight of 20g. The sliding time was taken as the indication of spreadability.

(ii) *Viscosity*: Viscosity of tissue conditioner incorporated with antibiotics and curcumin was analysed using Brookfield viscometer. The viscometer uses the principle of rotation of a cylinder or disc in a fluid sample that shows viscous resistance, and measures the torque needed to overcome that resistance to movement brought about by the rotation of the cylinder. The spindle is rotated with an electric motor through a beryllium-copper spring [16]. All measurements were carried out at room temperature to simulate clinical mixing conditions. The viscometer was positioned, and the No.1 spindle was suitably centered in the samples taken in a 10 ml test tube to standardize the testing environment. Each sample was tested thrice and the mean of three readings was considered. The spindle was rotated at a standard 100 rpm, and the readings were recorded in centipoise when the reading became stable. This implied that the materials setting process had initiated and was no longer amenable to manipulation [16].

(iii) *Thermal phase transition*: The crystallization and phase transformation of antimicrobial agents and their interactions with the tissue conditioner were analysed using Differential Scanning Calorimetry (STA 449 F5 Jupiter, NETZSCH Geratebau, GmbH). Approximately 2-5 mg of each sample was heated in an aluminum pan with lid from 30 to 200°C at a scanning rate of 10°C min⁻¹ under a stream of nitrogen gas at a flow rate of 50mL min⁻¹. The DSC graphs of bare TC (control) and TC incorporated with Co-amoxiclav, metronidazole and curcumin were recorded.

Results

Microbial sensitivity through disc diffusion technique

The images of the plates of the anti-biotic sensitivity test are shown in figure 2. The zone diameter for each drug was interpreted using

criteria published by Clinical and Laboratory Standards Institute. Our controls showed ZOI comparable with those cited in literature for both co-amoxiclav and metronidazole. No ZOI was seen around curcumin control disc.

(i) *Zone of Inhibition values*: A zone of inhibition (ZOI) of ≥ 21 mm and ≥ 15 mm for Co-Amoxiclav (Amoxicillin- Clavulanic acid) and metronidazole respectively, is considered to be susceptible for gram negative anaerobe. A ZOI of ≥ 14 mm is considered resistant for co-amoxiclav. For metronidazole, ≥ 15 mm is considered resistant [5]. For curcumin, 9 mm was considered resistant, 9-12 mm as intermediate and 13 as susceptible [6]. All three antimicrobial agents were sensitive to *Peptostreptococcus* (table 1). Co-amoxiclav was sensitive to all three bacteriae. Metronidazole was effective against *Peptostreptococcus* and *Porphyromonas*, while curcumin was effective against *Peptostreptococcus* (table 1).

(ii) *Statistical comparison*: As per the one-way Anova, there was a significant difference in the ZOI of Co-amoxiclav, metronidazole and curcumin against the growth of *Porphyromonas*, *Fusobacterium* ($P < 0.001$) and *Peptostreptococcus* ($P < 0.011$) (table 1). The post hoc Tukey's analysis of antimicrobial activity by ZOI measurement showed that metronidazole exhibited the most difference as compared to Co-amoxiclav and curcumin against the growth of *Peptostreptococcus* (table 2). All three pharmaceutical agents showed good results against *Porphyromonas* and against *Fusobacterium*. Co-amoxiclav and metronidazole showed better ZOI than curcumin.

(iii) *Effectiveness of Co-amoxiclav, metronidazole and curcumin concentrations*: A comparison of the five concentrations showed that 5:1 ratio of Co-amoxiclav, 1:1 of metronidazole and 1:1 of curcumin is the most effective in producing a zone of inhibition against *Fusobacterium*. The concentrations of 4:1 of co-amoxiclav, 1:1 of metronidazole and 3:1 of curcumin are most effective in producing a zone of inhibition against *Porphyromonas*. The concentrations 5:1 of co-amoxiclav, 4:1 of metronidazole and 4:1 of curcumin are found most effective in producing a zone of inhibition against *Peptostreptococcus* (figure 3).

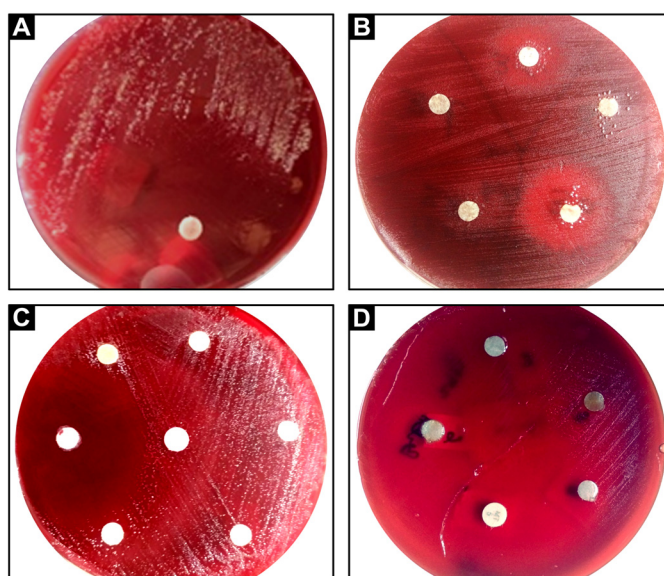


Figure 2: A) Zone of inhibition obtained with amoxicillin control against peptostreptococcus. B) Porphyromonas Zone of inhibition. C) Peptostreptococcus Zone of inhibition. D) Fusobacterium Zone of inhibition

Table 1: One-way ANOVA of zone of inhibition around three microbes by Amoxicillin - Clavulanic acid, Metronidazole, and Curcumin

Micro-organism	Material	N	Mean ZOI	SD	95% CI for Mean		F value	P value
					Lower Bound	Upper Bound		
Peptostreptococcus	Co-Amoxyclav	15	19.53	2.100	18.37	20.70	5.023	0.011*
	Metronidazole	15	24.00	6.448	20.43	27.57		
	Curcumin	15	20.20	2.455	18.84	21.56		
Porphyromonas	Co-Amoxyclav	15	24.87	2.560	23.45	26.28	20.280	0.001*
	Metronidazole	15	18.27	8.481	13.57	22.96		
	Curcumin	15	9.33	7.509	5.18	13.49		
Fusobacterium	Co-Amoxyclav	15	22.73	4.448	20.27	25.20	32.952	0.001*
	Metronidazole	15	10.40	4.852	7.71	13.09		
	Curcumin	15	11.00	4.766	8.36	13.64		

*Statistical significance $P < 0.05$

Table 2: Post hoc Tukey’s test of zone of inhibition around three microbes by Amoxicillin clavulanic acid, Metronidazole and Curcumin. Post Hoc Tukey Test.

Micro-organism	(I) group	(J) group	Mean Difference (I-J)	P value
Peptostreptococcus	Co-Amoxyclav	Metronidazole	4.467	0.014*
		Curcumin	0.667	0.900
	Metronidazole	Co-Amoxyclav	4.467	0.014*
		Curcumin	3.800	0.043*
	Curcumin	Co-Amoxyclav	0.667	0.900
		Metronidazole	3.800	0.043*
Porphyromonas	Co-Amoxyclav	Metronidazole	6.600	0.027*
		Curcumin	15.533	0.001*
	Metronidazole	Co-Amoxyclav	6.600	0.027*
		Curcumin	8.933	0.002*
	Curcumin	Co-Amoxyclav	15.533	0.001*
		Metronidazole	8.933	0.002*
Fusobacterium	Co-Amoxyclav	Metronidazole	12.333	0.001*
		Curcumin	11.733	0.001*
	Metronidazole	Co-Amoxyclav	12.333	0.001*
		Curcumin	0.600	0.935
	Curcumin	Co-Amoxyclav	11.733	0.001*
		Metronidazole	0.600	0.935

*Statistical significance $P < 0.05$

Spreadability

The material was mixed for 45 secs and the time taken for the initiation of tests was standardized to 45 seconds equaling the mixing time of 1.5 minutes by the manufacturer. Spreadability was calculated as the time taken by one glass slab to slide over 6 cm, measured with the help of a stop clock. The statistical analyses of the results showed significant difference between control and all other groups. Tissue conditioner with Co-amoxiclav showed the maximum deviation from the control. Tukey Post hoc test revealed significant difference between control and both ratios of amoxicillin. The spreadability of metronidazole 1:1 and curcumin 4:1 ratio remained similar to that of the control (table 3,4).

Viscosity tests

The time taken by the sample to start setting (initial setting time) marked the end of the viscosity test. Viscosity was measured in centipoise units. There was a significant difference between viscosity of the control vs viscosity of Co-amoxiclav (Amox), and two ratios of curcumin mixtures. The 3:1 ratio of curcumin and either ratio of metronidazole showed nearly the same viscosity as the control (tables 5, 6 and 7).

Thermal phase transition and crystallinity

The DSC for the control showed a prolonged glass transition

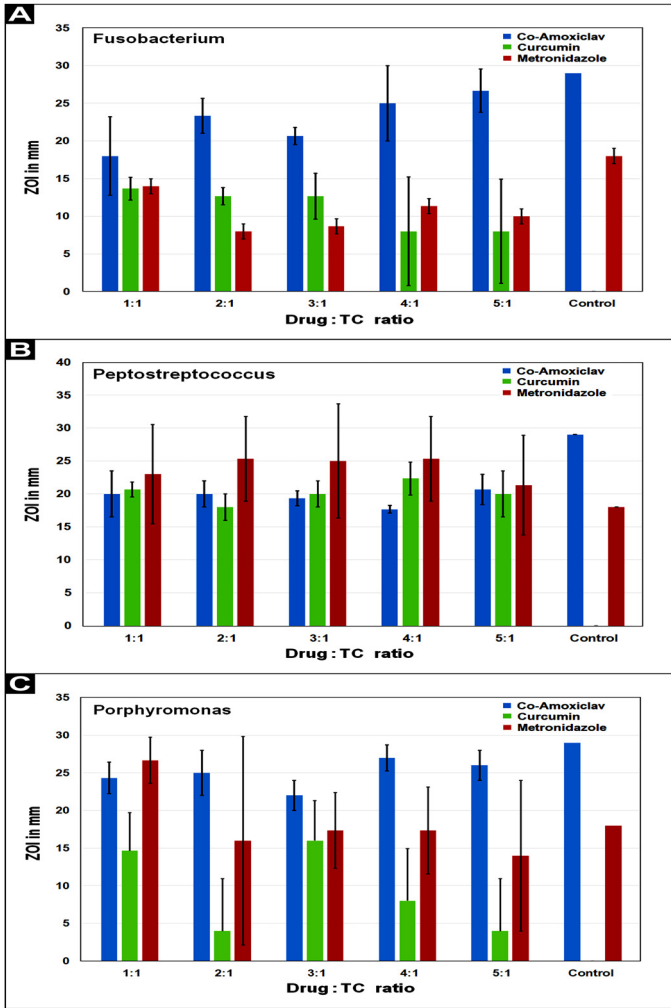


Figure 3: Comparison of effectiveness of various concentrations of Co-amoxycylav, Metronidazole and Curcumin against A) Fusobacterium; B) Peptostreptococcus and C) Porphyromonas

Table 3: Anova to determine significance between groups

Spreadability Between Groups	Sum of Squares	df	Mean Square	F	Sig.
	78246.049	7	11178.007	21.874	0.000

Table 4: Post hoc Tukey test of significance between specific groups

(I) Material	(J) Material	Mean Difference (I-J)	Std. Error	Sig.
Control	amox4:1	-143.097 [*]	18.45765	0.000
	amox 5:1	-119.430 [*]	18.45765	0.000
	metro1:1	1.57	18.45765	1.000
	metro4:1	4.47	18.45765	1.000
	cur1:1	-4.73	18.45765	1.000
Control	cur3:1	-4.53	18.45765	1.000
	cur 4:1	1.537	18.45765	1.000

temperature similar to that of polymers (figure 4A). The DSC for the sample with amoxicillin 4:1 showed an endothermic reaction with melting point of around 190°C, corresponding to that of amoxicillin. The nature of the peak implies that amoxicillin is in an amorphous form. The apparent increase in the enthalpy could be due to the glass transition of the tissue conditioner (figure 4B). This confirms that there is no interaction between tissue conditioner and amoxicillin. The DSC for the sample with metronidazole 1:1 showed an endothermic peak at 161°C, corresponding to the melting point of metronidazole. The nature of the peak implies that metronidazole is in a crystalline form (figure 4C). The DSC for the sample with curcumin 1:1 showed an endothermic peak at 179°C, corresponding to the melting point of curcumin. The nature of the peak implies that curcumin is in a crystalline form (figure 4D). This confirms that the tissue conditioner has no interaction with metronidazole and curcumin.

Discussion

Microbial control plays a crucial role in progress of healthy osseointegration. Anaerobic bacteria have been particularly identified as causative organisms in both early and late healing phases. Chronic periodontitis and peri implantitis may have similar microbial etiology [17]. A meta-analysis cited 19% of patients had peri

Table 5: Descriptive statistics for viscosity

	Mean	SD
Control	61.267	3.1086
Amox4:1	43.333	0.9452
Amox 5:1	37.300	1.1533
Metro1:1	65.533	0.8083
Metro4:1	61.267	1.0066
Cur1:1	40.467	1.1372
Cur3:1	65.333	1.0263
Cur 4:1	88.200	1.0000
Total	57.838	16.1756

Table 6: Anova for significance between groups

Viscosity Between Groups	Sum of Squares	df	Mean Square	F	Sig.
	5984.156	7	854.879	404.677	.000

Table 7: Post hoc Tukey test of significance between specific groups

(I) Material	(J) Material	Mean Difference (I-J)	Std. Error	Sig.
Control	amox4:1	17.9333 [*]	1.1867	0.000
	amox 5:1	23.9667 [*]	1.1867	0.000
	metro1:1	-4.2667 [*]	1.1867	0.039
	metro 4:1	0	1.1867	1.000
	cur1:1	20.8 [*]	1.1867	0.000
Control	cur3:1	-4.0667	1.1867	0.053
	cur 4:1	-26.9333 [*]	1.1867	0.000

*The mean difference is significant at the 0.05 level

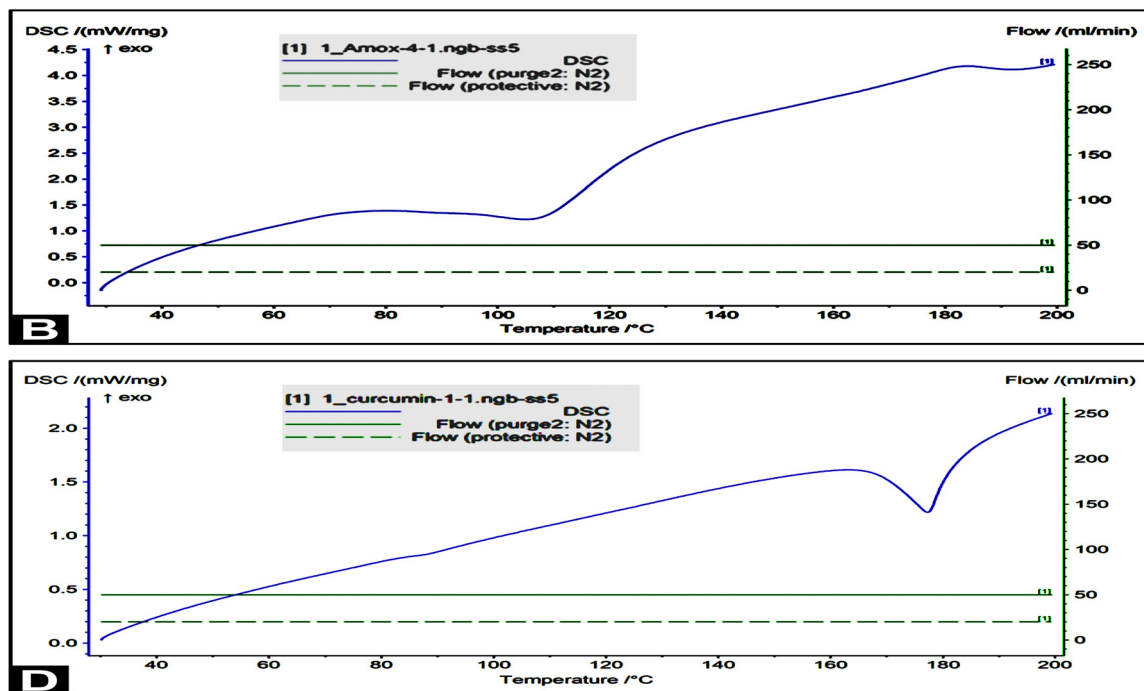


Figure 4: A) Control; B) Co-Amoxiclav 4:1; C) Metronidazole 1:1; D) Curcumin 1:1

implantitis and 46% of patients had peri implant mucositis [18].

The Disc Diffusion Method uses the principle of testing for antibiotic sensitivity against specific bacteria. The diameter of the zone of inhibition is directly proportional to the susceptibility of the microorganism to the tested drug [19]. As per the one-way Anova, there was a significant difference in the ZOI of Co-amoxyclov, metronidazole and curcumin against the growth of *Porphyromonas* and *Fusobacterium* ($P < 0.001$) and *Peptostreptococcus* ($P < 0.011$). The post hoc Tukey's analysis showed that metronidazole showed the most difference as compared to co-amoxyclov and curcumin against the growth of *Peptostreptococcus*. All three pharmaceutical agents showed good results against *Porphyromonas* and against *Fusobacterium*, Co-amoxyclov and metronidazole showed better ZOI than curcumin. This is in concurrence with a study that showed metronidazole displayed a 97% susceptibility rate when tested by the test method against anaerobe isolates from species like *Bacteroides*, *Prevotella* and *Fusobacterium* while Co-amoxyclov showed a 95.5% susceptibility rate just like imipenem [20].

The elute of curcumin obtained from the artificial saliva produced a zone of inhibition that was comparable with the recommended ZOI in literature [21]. While a minimum serum level of 16µg/ml of antibiotic is needed, the same is not known with curcumin. This is in concurrence with a study that showed the zone of inhibition of curcumin against gram positive aerobes, a bulk microbial component of the biofilm, was comparable to that of Ciprofloxacin. Another study showed minimum inhibitory concentrations achieved only in high concentrations of curcumin [22]. The study evaluated gram positive cocci and not anaerobic rods. This could explain why the control disc produced no zone of inhibition against anaerobic bacteria [23]. Further studies will be necessary to identify the strength required in serum levels to obtain

bactericidal activities with curcumin or antibiotics and compare them with levels reached in saliva or Gingival Crevicular Fluid on local application.

In this study, the effectiveness of each of the elutes was tested in creating a zone of inhibition against obligate gram negative anaerobes (*Porphyromonas* and *Fusobacterium*) as well as gram positive anaerobes like *Peptostreptococcus*, accounting for the poly microbial oral environment. Therefore, it is imperative that pharmaceutical agents have a bactericidal effect on a range of microbes.

The advantages of the disc diffusion method include simplicity, providing definite results of clinical relevance and flexibility to test a variety of pharmaceutical agents. The disadvantage is that all procedures are manual thereby making error inclusion inadvertent. Results could be either "susceptible", "resistant" and "intermediate" [19].

Post hoc Tukey analyses of spreadability test results showed significant difference in spreadability between control and Co-amoxyclov. Metronidazole 1:1 and the curcumin groups showed similar spreadability properties to that of the control, implying that the consistency of the mixed material did not vary significantly from that of control. Co-amoxyclov exhibited the maximum deviation from the control indicating drastic change in the spreadability of the tissue conditioner. The incorporation of Metronidazole and curcumin did not cause drastic changes in the spreadability of tissue conditioner when compared to Co-amoxyclov. The difference in spreadability upon adding the antibiotics and antimicrobial agents has significant clinical implication, as the spreadability of the material will influence the thickness of the material as well as the ease of handling [15]. A runny material will be hard to handle and a very thick material will not flow adequately as this may cause pressure on a new surgical site.

Viscosity is an important viscoelastic property of tissue conditioners that allows for adequate flow of the material within the setting time. A fluid has an internal friction referred to as shear and is a function of the amount of force required to overcome the internal friction. Shear rate is the speed at which the fluids move. The force per unit area to produce a shearing movement is the shear stress. A material requiring a shear stress of one dyne per square centimeter to produce a shear rate of one reciprocal second has a viscosity of one poise (P), or 100 centipoises (MPa). The rheology of semi-solids is very much influenced by the microstructure changes. In addition, the viscosity of a semisolid formulation as in the present case will influence its application and handling properties while being used intraorally [16]. Tissue conditioner with Co-amoxiclav in either ratio and Curcumin at 1:1 and 4:1 ratios showed significant difference from the control group. Incorporation of metronidazole and curcumin at 3:1 concentration did not significantly alter the viscosity of the tissue conditioner.

Differential Scanning Calorimetry is a highly sensitive technique to study the thermotropic properties of many different biological macromolecules and extracts. DSC is also a very relevant tool for analyzing the thermodynamic properties as a function of time and temperature of various pharmaceutical products, such as, biopolymers, proteins, peptides, and lipid carriers [24]. We obtain qualitative and quantitative details such as the melting and degradation temperatures, glass transition temperature which is a second order transition often seen in polymeric materials, melt and crystallization enthalpy, specific and latent heats, polymorphism, and purity of the materials. In amorphous solids, glass transition temperature is associated with molecular movement and their relaxation time. The resultant thermogram shows four transitions identified from low to high temperature as: glass transition temperature (T_g), crystallization temperature (T_c), melting temperature (T_m), and degradation temperature (T_d). The wide range of temperatures allows for easy analyzing of data of the transitions.

The DSC for the control showed a prolonged glass transition temperature like that of polymers. The powder of auto polymerizing acrylic based material consists of polyethyl methacrylate/copolymer, Polymethylmethacrylate/copolymer, benzoyl peroxide, phthalyl butyl glyconate, pigments, fillers. Liquid contains methyl methacrylate, ethylene glycol dimethacrylate, ester plasticizer mixture like dibutyl phthalate, butylphthalyl butylglycolate, benzylbutyl phthalate [16,24,25], dibutylsebacate, ethyl alcohol [25].

The nature of the peak for Co-amoxiclav implied that amoxicillin was in an amorphous form. An apparent increase in enthalpy was noted, which could be due to the glass transition of the tissue conditioner. This confirms that there is no interaction between tissue conditioner and amoxicillin [26,27]. The nature of peaks in test materials showed that the incorporated metronidazole and curcumin retained their crystalline form without interaction with the polymeric tissue conditioner [28,29]. The DSC of the tissue conditioner was similar to that of polymers. The incorporation of metronidazole or curcumin did not show any shift in the peak of the tested materials, indicating there was no interaction between the materials [28,29]. Therefore, they are compatible with each other, and tissue conditioner could be used a carrying medium.

Conclusion

This study proved definitively that polymer-based tissue conditioner can be used as an effective medium to carry drugs with positive elution. The elutes from tissue conditioner incorporated with antimicrobial agents showed a zone of inhibition around the

anaerobic and aerobic cultures indicating the effectiveness of release of the drugs. The handling properties like spreadability and viscosity can be kept similar to that of bare tissue conditioner using appropriate concentrations of the antimicrobial agents. No evident interaction was observed between the tissue conditioner and the drugs in differential scanning calorimetry test. The properties of tissue conditioner were not altered by the addition of specific drugs like metronidazole and curcumin. Also, the potency of antibiotics was not affected by the tissue conditioner. The addition of Co-amoxiclav changed the properties of the TC carrier marginally. The drug eluting tissue conditioner can open new treatment modalities in the management of peri-implantitis, with reference to effectiveness of local drug delivery and reduction of oral administration of antibiotics.

Acknowledgements

We acknowledge the Ramaiah University of Applied Sciences, Bangalore, Ramaiah Institute of Technology, Father Mullers Hospital for the test facilities and Sami Labs of the Sami-Sabinsa Group Limited, Bangalore, India for supplying free the curcumin required for this study. Also, we are grateful to Dr. Eva C. Das for the final copy editing of the manuscript.

References

- Chen T, Yu W.H., Izard J, Baranova O.V., Lakshmanan A., Dewhirst F.E., The Human Oral Microbiome Database: a web accessible resource for investigating oral microbe taxonomic and genomic information. Database (Oxford). 2010, baq013 (2010).
- Van Brakel R, Cune M.S., Van Winkelhoff A.J., De Putter C., Verhoeven J.W., Van der Reijden W, Early bacterial colonization and soft tissue health around zirconia and titanium abutments: An in vivo study in man. Clin Oral Implants Res. 22(6), 571-7 (2011).
- Aoki M., Takanashi K., Matsukubo T, et al., Transmission of periodontopathic bacteria from natural teeth to implants. Clin Implant Dent Relat Res., 14(3), 406-11 (2012).
- Dar-Odeh N.S., Abu-Hammad O.A., Al-Omiri M.K., Khraisat A.S., Shehabi A.A., Antibiotic prescribing practices by dentists: a review. Ther Clin Risk Manag., 6, 301-6 (2010).
- Mohsen S., Dickinson J.A., Somayaji R., Update on the adverse effects of antimicrobial therapies in community practice., Can Fam Physician. 66, 651-9 (2020).
- Venable S.J., Principles of antimicrobial therapy. Drug Ther Nurs. 10(39), 805-14 (2012).
- Najah A. Mohammed, Neama Y. Habil., Evaluation of antimicrobial activity of curcumin against two oral bacteria, Autom Control Intell Syst. Special Issue: Artificial Nano Sensory System., 3(2), 18-21 (2015).
- Wen H., Jung H., Li X., Drug Delivery Approaches in Addressing Clinical Pharmacology-Related Issues: Opportunities and Challenges. AAPS J. 7(6), 1327-40 (2015).
- Rathi S., Verma A., Resilient liners in prosthetic dentistry: An update. Int J Appl Den Sci., 4(3), 34-8 (2018).
- Urban V.M., De Souza R.F., Galvao Arrais C.A., Borsato K.T., Vaz L.G., Effect of the association of nystatin with a tissue conditioner on its ultimate tensile strength. J Prosthodont. 15(5), 295-9 (2006).
- Levison M.E., Levison J.H., Pharmacokinetics and pharmacodynamics of antibacterial agents. Infect Dis Clin North Am. 23(4), 791-815 (2009).
- Adamczak A., O zarowski M., Karpinski T.M., Curcumin, a natural antimicrobial agent with strain-specific activity. Pharmaceuticals (Basel). 13(7), 153 (2020).
- Ampicillin P. Statement 1996 CA-SFM Zone sizes and MIC breakpoints for non-fastidious organisms. Clin. Microbiol Infect., 2(1), S46-S49 (1996).
- Bomdya R.S., Shah M.U., Doshi Y.S., Shah V.A., Khirade S.P., Antibacterial activity of curcumin (turmeric) against periopathogens - An in vitro evaluation. J Adv Clin Res Insights., 4(6), 175-80 (2017).
- Kryscio D.R., Sathe P.M., Lionberger R., et al. Spreadability measurements to assess structural equivalence (Q3) of topical formulations - A technical note. AAPS PharmSciTech., 9(1), 84-6 (2008).
- Lubrizol Test Procedure TP N01004. Determination of Viscosity Using A Brookfield Viscometer for Conditioning Polymers. Lubrizol Adv Mater., 1-5 (2013).

17. De Boever A.L., De Boever J.A., Early colonization of non-submerged dental implants in patients with a history of advanced aggressive periodontitis. *Clin Oral Implants Res.*, 17(1), 8–17 (2016).
18. Lee CT, Huang YW, Zhu L, Weltman R. Prevalences of peri-implantitis and peri-implant mucositis: systematic review and meta-analysis. *J Dent.* 62, 1-12 (2017).
19. Giuliano C, Patel CR, Kale-pradhan PB. A Guide to Bacterial Culture Identification and Results Interpretation. *Pharmacy and Therapeutics.* 44(4), 192–200 (2019).
20. Shilnikova II, Dmitrieva N V. Evaluation of antibiotic susceptibility of Bacteroides, Prevotella and *Fusobacterium* species isolated from patients of the N. N. Blokhin Cancer Research Center, Moscow, Russia. *Anaerobe.* 31, 15–8 (2015).
21. Gul P, Bakht J. Antimicrobial activity of turmeric extract and its potential use in food industry. *J Food Sci Technol.*, 52(4), 2272–9 (2015).
22. Gunes H, Gulen D, Mutlu R, Gumus A, Tas T, Topkaya AE. Antibacterial effects of curcumin: An in vitro minimum inhibitory concentration study. *Toxicol Ind Health.*, 32(2), 246–50 (2016).
23. Jorgensen J.H., Ferraro M.J., Antimicrobial susceptibility testing: A review of general principles and contemporary practices. *Clin Infect Dis.* 49(11), 1749–55 (2009).
24. Chiu M., Prenner E., Differential scanning calorimetry: An invaluable tool for a detailed thermodynamic characterization of macromolecules and their interactions. *J Pharm Bioallied Sci.*, 3(1), 39–59 (2011).
25. Anupama Prasad D., Rajendra Prasad B., Shetty V., Shastry C.S., Krishna Prasad D., Tissue conditioners: A review. *Nitte Univ J Heal Sci.*, 4(2):152-7.
26. Swamivelmanickam M., Valliappan K., Reddy P.G., Madhukar A., Manavalan R. Preformulation studies for amoxicillin trihydrate and dicloxacillin sodium as mouth dissolve tablets. *Int. J ChemTech Res.*, 1(4), 1032-1035 (2009).
27. Concannon J., Lovitt H., Ramage M., Tai L.H., McDonald C., Sunderland V.B., Stability of aqueous solutions of amoxicillin sodium in the frozen and liquid states. *Am J Hosp Pharm.*, 43(12), 3027-30 (1986).
28. de Souza, N.A.B., de Souza, F.S., Basílio, I.D. et al. Thermal stability of metronidazole drug and tablets. *J. Thermal Analysis and Calorimetry* 72, 535–538.
29. Sayyar Z., Jafarizadeh H., Temperature effects on thermodynamic parameters and solubility of curcumin O/W nanodispersions using different thermodynamic models. *Int. J. Food Engg.*, 15 (1-2), 20180311 (2019).



Review Article

Yeast: A Potential Vaccine Delivery Carrier

V.C. Patole*, J.G. Mahore, S.S. Deshkar, S. Shekade, A. Gutte

Department of Pharmaceutics, Dr.D.Y.Patil Institute of Pharmaceutical Sciences and Research, Pimpri,Pune, Maharashtra, India

Received: 9 October 2022

Accepted: 27 November 2022

Published online: 30 June 2023

Keywords: yeast, vaccine, recombinant, oral, immune response, proteins, genes

Yeasts are genetically tractable, and they share many features with humans. They represent a potential carrier for the delivery of drugs, proteins and genes for the treatment of various diseases and disorders. Yeast offers various advantages such as rapid growth rate, inexpensive, easy availability, minimum growth requirements, allows genetic modification, non-immunogenic, natural adjuvant and well defined fermentation technology which makes them a suitable model for development of vaccines. The specific cellular characteristics possessed by yeast makes them resistant to gastro-intestinal environment and allows passage through the gastro-intestinal membrane, enabling them to be a potential carrier for oral vaccines. In this review, we seek to outline the beneficial role of yeast using its recombinant modification with supporting evidence to achieve effective vaccine delivery in stimulating and modulating the immune response in the host. In addition, the efficacy of yeast based carrier for oral vaccines is also highlighted.

© (2023) Society for Biomaterials & Artificial Organs #20063423

Introduction

Conventional vaccines have proven invaluable in combating infectious diseases. Conventional vaccines make it possible to eradicate smallpox and polio [1]. However, these success stories do not negate the challenges in the current method of vaccine preparations, which has many drawbacks, such as multiple injections and the need of the adjuvant to potential immune response [2]. Moreover, these vaccine preparations are inherently pathogenic because the live attenuated vaccines revert to virulence if they are not handled properly by the immune system. Development of vaccines against infectious diseases is hindered by the mass cultivation of pathogens. Traditional vaccines have been associated with a steady increase in allergic or hypersensitive reactions following vaccination in certain groups of individuals [3]. As the number of HIV-positive individuals continues to rise, as do the number of transplant recipients under immunosuppressive drugs, there is an additional concern regarding the use of live or attenuated vaccines in immunocompromised individuals [4]. A second issue associated with conventional vaccines is maintaining a cold chain from a manufacturing unit to an end-user [5]. Considering these limitations of conventional vaccines, the vaccine delivery efficiency is still far from optimal and exploring new kinds of biomaterials for vaccine administration

remains a challenge. Improving the biocompatibility of materials used in vaccine delivery is a constant challenge. The recent achievements have shown, there are still several unsolved issues that can be addressed by using microorganisms [6].

The biochemical properties of microorganisms and breakthroughs in genetic engineering tools have shown promising results in drug delivery utilizing microorganisms, such as bacteria, viruses, or fungi [7]. Amongst all microorganisms, yeast is particularly resilient and exhibits a wide range of physiochemical tolerance. Furthermore, some yeast species are given a lot more attention by the scientific community than others, such as *Saccharomyces cerevisiae*, *Saccharomyces bayanus*, *Candida utilis*, *Kluyveromyces fragilis*, *Torulopsis lipofera*, *Edomycetvernalis*, and *Cryptococcus curvatus* [8].

A constant challenge for vaccine development is to increase the biocompatibility of the antigen carriers. A capsular non-pathogenic yeast shell microparticle offers biocompatibility and can be administered safely in vaccine delivery. It is possible to facilitate antigen loading on yeast because of its uniform particle size and hollow nature [9].

Although GRAS status assures the safety of the yeast in vaccine delivery, heat inactivation is used to reduce potential safety-related risks associated with administering living cells [10]. Furthermore, by using heat-inactivated and lyophilized yeasts, the need for refrigeration can also be reduced.

* Corresponding author

E-mail address: vinita@dypvp.edu.in (Dr. Vinita C. Patole, Assistant Professor)

With the advent of yeast for vaccine delivery researchers can overcome the challenges in conventional vaccine delivery, such as reduced thermal stability, short shelf lives at room temperature, and short-lived protection against multiple pathogens. Living recombinant microorganisms have been used in the past couple of centuries to deliver vaccines with significant improvement in therapeutic outcomes. Recombination of microorganisms makes it possible to increase antigen-specific immunity by coupling antigens to the surface of yeast microcapsules [11].

It is possible to stimulate both MHC class I- and class II-restricted primary T-cell responses by whole yeast as an adjuvant [12]. An antigen-presenting cell surface contains pathogen-related molecular pattern receptors called Dectin-1 and complement receptor 3, which can specifically identify the yeast. As a carrier of vaccine, yeast-derived β -1,3-D-glucan and mannan have gained a lot of attention since they possess the inherent adjuvant capacity that can enhance the immune system by enhancing the functionality of neutrophils, and macrophages, DCs, and epithelial cells. The ability of the *Saccharomyces cerevisiae* glucan to increase TNF-alpha in the rat alveolar macrophages, made it possible to use yeast microparticle-mediated vaccine delivery for cancer immunotherapy [13]. This indispensable β -1,3-D-glucan of yeast vaccine could contribute to intensifying the immune response in vaccine delivery [14].

For a synthetic strain of yeast to be introduced into the body niche with minimal unwanted effects, it is imperative to understand the dynamics of the microbial ecosystem at the site of interest. The yeast is mostly involved in indirect interaction with the microbial ecosystem in the body, such as competition, commensalism, mutualism, and amensalism [15]. This is all because yeast cells are rich in glucans, mannoses, and chitin, which stimulates the coaggregation of cells as well as cohesion, which favors probiotic survival. Co-aggregation occurs as a result of the interaction between dectin-like identified proteins on the surface of bacteria and yeast mannans. Using yeast to transport antigen appears to be a viable technique since it offers several advantages over other systems, including the lack of toxicity, the ability to administer via the oral route, and immunostimulating qualities. Therefore, the present review is directed toward applications of yeast as an effective carrier for vaccine delivery.

Yeast as Vaccine Delivery System

The innovative approaches in the delivery of vaccines using living recombinant micro-organisms (act as an antigen) to elicit immune response have helped significantly to improve the therapeutic outcomes. The antigen-presenting cells are adept at internalizing many pathogens *in vivo*, but biosafety concerns limit the use of live pathogens in vaccines [16]. Direct administration of pathogens is associated with potential risks [17]. However a capsule made of yeast shell can present the antigen to dendritic cells, thus acting as a potential vaccine delivery platform [18]. Recently, the yeast shells are also been studied for delivery of cancer immunotherapy vaccines [9]. The cell wall of yeast is composed mainly of β -glucan which has a thickness of around 100-115nm, this thicker cell wall enables the yeast to be used as microcapsule [19]. The yeast microcapsules offer an attractive way to load antigens as well as it allows binding of antigens on its surface to induce immune response. The porous and hydrophilic nature of the yeast capsules pose some difficulty in loading the antigens, on the other hand linking antigen on its surface is much easier and feasible approach. Studies report that when antigens are linked to surfaces rather than encapsulated, the immune response is enhanced [9]. β -glucans (structural cell wall component of fungi) are widely recognized by the monomers of dectin (cell-surface immune receptor for β -glucans). The molecules

of dectin have an important part in the defence mechanism of the host against the fungal infections. They arrange themselves into dimers that bind to β -glucans, thus increasing its binding ability to the dectin molecules [20]. The process of phagocytosis and internalization of associated proteins (antigens) by dendritic cells results in the uptake of β -glucan particles after binding to the dectin molecules. [8]. By delivering antigens via β -glucan particles, the immune response can be enhanced [12]. Once the yeast cells are uptaken by the dendritic cells, they get mature into antigen presenting cells (APC)'s. Proteins (antigens) expressed by the yeast cells are represented to either major histocompatibility (MHC) class-I antigen presenting pathway, which presents the antigens to the cytotoxic T cells with CD8+ receptors or to (MHC) class -II antigen presenting pathway where in the antigens are presented to helper T-cells with CD4+ receptors helping to generate cell mediated immunity [21]. Alternately, with the yeast display technique (where the antigens are bound to the surface), the antigens attach to the bound antibody as well as it can bound to soluble antibody inside the body and induce humoral response. Huang *et al.* physically encapsulated antigen in β -glucan particles by linking the antigen to the yeast surface [22].

Recombinant modification of yeasts for vaccine delivery

With the advancement in the field of molecular biology, it is now possible to express protein in any cell (prokaryotic or eukaryotic) organism. Yeast represents an attractive model for the expression of heterologous genes. Among the yeast species, *Saccharomyces cerevisiae*, is widely used for the expression of heterologous genes and help in the production of therapeutically effective proteins. The complete information about *Saccharomyces cerevisiae* on its molecular biology and genetic sequence makes it an ideal model for expression of proteins [10]. The protein expression in the yeast cells is similar to that of the mammals. The easy availability of yeast cells and the simple technique of its cultivation on a large scale enable it to be used for several biotechnological purposes. *Saccharomyces cerevisiae* has been commonly used from several years in the fermentation process especially for brewing and baking which indicates its non-toxic nature. It is discovered that the yeast cells have the ability to be used as natural adjuvants and are able to elicit immune response [23]. The profound knowledge of genetic engineering and DNA cloning has enabled researches to develop recombinant products. The unique ability of the yeast cells to allow easy mutations in them make an attractive carrier for large scale production of genetically recombinant products. Another important advantage offered by the yeast cells is their long term antigen stability at room temperature.

Saccharomyces cerevisiae-based vaccines have been developed by Ardiani et al (2010), in which the yeast is engineered to express tumor-specific antigens that stimulate CD4+ and CD8+ T-cells and stimulate strong immune responses against malignant or virally infected cells. In addition to CD4+ and CD8+ T-cell activation, *Saccharomyces cerevisiae*-based vaccines can also reduce abnormal cell growth by releasing immunomodulatory cytokines [24].

Hepatitis B vaccine derived from yeast was developed and produced by J. Stephenne in 1990 using recombinant DNA technology. A seed lot principle was followed in the production of yeast-derived vaccines. This process involved maintaining a master seed lot of recombinant yeast strains, which were then stored individually in ampoules at -70°C. Fermentation could be carried out using seed stocks that could be stored for many years. The yeast multiplied itself in the petri dishes. The study involved the extraction and purification of antigen from yeast cells. After preparation, yeast-derived vaccines based on recombinant DNA technology were filled

into sterile vials, sealed, packaged for use, and stored at 4°C [25]. The yeast-derived vaccines proved to be safe, potent, and cost-effective vaccines, which could be used in mass vaccination programs.

Recombinant proteins containing the receptor-binding domains (RBDs) of SARS-CoV-2 were developed by Zhang *et al.* (2021). The vaccine antigen for SARS-CoV-2 is SARS-CoV-2-S or its RBD, because these antigens produce antibodies against the infection. *Pichia pastoris* (*P. pastoris*) yeast could be transformed with the expression vector pPinká-HC-RBD to produce monomeric RBD for SARS-CoV-2-S. Transformed yeast-derived RBD-monomers induce neutralizing antibodies against SARS-CoV-2 infection when injected intraperitoneally into mice. Moreover, the authors reported that genetically engineered dimeric RBD produced longer lasting neutralizing antibodies when compared to monomeric RBD. Researchers found that antisera raised against the RBD of a prototype strain of SARS-CoV-2 neutralized the two dominant circulating variants, B.1.1.7 and B.1.351, indicating a broad range of protective potential for RBD-based vaccines. SARS-CoV-2 vaccines for global distribution can be developed rapidly and cost-effectively using yeast-derived RBD-based recombinant vaccines based on RBD [26].

Han Lei, *et al.* reported the development of yeast surface-displayed H5N1 avian influenza vaccines by presenting H5N1 hemagglutinin (HA) to the surface of the yeast cells. Initially, the host cell for HA was constructed on the surface of the yeast cells by DNA cloning using *S. cerevisiae* shuttle plasmid pYD1 and pcDNA3.1/H5N1/HA/optimized plasmid to form *S. cerevisiae* EBY100. After the immunization of mice with EBY100/pYD1-HA vaccines, there was increase in both humoral and cell-mediated immunity in mice with the detection of high level of H5N1 HA-specific IgG1 and IgG2a antibody after boost immunization. The recombinant yeast based vaccine H5N1 hemagglutinin (HA) was effective in providing complete protection from H5N1 virus infection in mice [27].

Since *S. cerevisiae* contains DNA plasmids, it makes an attractive model for genetic manipulation. A DNA plasmid allows yeast to serve as a cloning vector. For plasmid to function, a selective marker is required, which is crucial for identifying the transformed cell after cloning. It is these selective markers that are known as shuttle vectors. There has been much evidence that yeast has the ability to clone specific DNA sequences from *Escherichia coli* that can then be transferred into *Saccharomyces cerevisiae*'s cell wall for the purpose of production [28]. As far as yeast cloning vectors (yeast shuttle vectors) are concerned, there are several types, such as yeast episomal plasmids (YEPs), which are capable of replicating independently, and yeast integrative plasmids (YIPs), which can't. Apart from the fact that recombinant proteins expressed in yeast are easier to purify, they are also immunogenic, making them a good candidate for developing therapeutically effective proteins. It is possible to integrate genes into non-transcriptional spaces (NTSs) of yeast rRNA gene, as well as a desired clone to be integrated at yeast chromosomal centromere, which facilitates stable cloning. It was possible to integrate antigens with high copy numbers into rDNA region of yeast using nontranscriptional spaces of yeast rRNA.

Yeast for delivery of oral vaccines

Yeast also provide an attractive platform for the development of edible vaccine, they are generally regarded as safe by (GRAS) by USFDA [29]. The composition of yeast cell wall is basically composed of β -glucan and chitin. The chitin cell wall enveloped by mucilaginous glycoalyx, enables the adhesion of the yeast to the host cell membrane as well as acts as GI absorption enhancer. The analog of chitin (chitosan) exhibits mucoadhesive properties at the acidic pH which helps to improve the paracellular permeability

by affecting the tight epithelial junctions allowing the transport of actives into the blood stream at acidic pH [30]. The benefit of edible vaccine in promoting or activating immune cells in the mucosal tissue is far more advantageous than parenteral vaccines, which are not completely able to generate the immune response in the mucosal tissue. The immune response induced in the mucosal membrane of the yeast cells not only provides protection to the orally administered vaccine antigen against the adverse gastrointestinal conditions but also promote the adjuvant properties of the vaccines. Studies reported by Bal *et al.* emphasized that orally administered yeast based vaccine effectively initiated immune response in the mucosal tissue with the enhanced secretion of IgA antibodies and IgG antibodies in the blood stream [31]. The mucosal membrane is spread throughout the host's body and it represents a major portion through which the pathogens can invade the host system, hence activating mucosal membrane immune response is important to control and prevent various infections. Elena Ivanova (2021) reported the role of yeast-based delivery systems for oral vaccines and oral gene therapies. The administration of vaccines and gene therapies by oral route, possess challenge due to varying physiological environment and enzymes in the gastrointestinal tract causing in effective GI absorption. The cellular structure of yeast helps in protecting the vaccines (antigens) from the harsh environmental conditions of GI tract. Yeast capsules even play an important role in stimulating the host immune response. After the oral administration of yeast, the M cells located in the gastro-intestinal tract help in the uptake of antigens by the APC's situated in the Peyer's patch. This step play an important role in inducing the immune response associated with the mucosal membrane. The author further reports that genetically modified recombinant yeast can express cell penetrating proteins with improved cell adhesion properties which could prove to be beneficial in the delivery of oral gene therapies [32].

Kumar and Kumar (2019) reported that *Saccharomyces cerevisiae* and *Pichia pastoris* represents a promising model for vaccine development due to their non- pathogenic nature and complete information on their genome sequence [33]. The authors further report in their review that the ability of yeast to express heterologous proteins which are therapeutically effective against bacterial, fungal, viral, protozoan infections and even their possible use in the cancer therapy. The yeast based vaccines can be used in several ways such as whole recombinant yeast, yeast display, purified protein immunogens and virus like particles. The yeast display based vaccines recognizes the pathogenic antigens immediately and its particulate nature enables the engulfment of the whole cell by the dendritic cells thus stimulating the T-cells mediated immune response. Alternatively, in case the of yeast display based vaccines the antigens are recognized on their surface by the antibodies in blood or bound to the surface of the B- cells. The capability of the yeast to produce CD81, CTLs cells involved in the identification and killing of the tumor cells makes them a potential candidate in modulating tumor growth and thus can be used in cancer therapies. The authors further emphasizes that the development of yeast based vaccines will prove to be an cost effective way for development of oral vaccines wherein the feasibility of the mass culture of associated pathogens is a difficult task [9].

Whole recombinant yeast based vaccines provides an effective approach to overcome the stability related issues of pure peptide based vaccines by providing an appropriate cellular environment required to maintain the protein structure of antigen and its stability. The strategy of expressing immunogenic proteins from pathogenic species on the whole recombinant yeast is known as yeast display which provides an opportunity for the development of edible

vaccines. Virus like proteins are self assembled protein complexes similar to virus, but they lack viral genes and are reported to elicit higher immunogenic response as compared to the purified protein antigen [33]. Additionally, their particulate nature of VLP can help to produce both B and T cell immune response. This self assembled virus like particles can be fused with yeast Ty retro-transposon without affecting the immunogenic nature.

C.Sabu *et al.* (2019) studied the effective use of bio-inspired oral insulin delivery system using yeast microcapsule in the treatment of diabetes mellitus [34]. The authors reported that insulin degradation in gastro-intestinal tract could be prevented by coating insulin loaded yeast microcapsules with alginate. It is commonly observed that the acidic environment of the stomach along with enzymes in the gastrointestinal tract lead to the degradation of drugs. In this case, insulin was loaded into microcapsules derived from *Saccharomyces cerevisiae*. The use of bioinspired insulin yeast microcapsule (YMC) coated with alginate have shown promising results in hyperglycemia. The alginate coating protected the YMC from adverse environment of the gastro-intestinal tract. The presence of 1,3- β -glucan polysaccharides in the outer shell wall of yeast facilitated receptor-mediated uptake of YMC by phagocytic cells via M-cell endocytosis. This process enabled the systemic absorption of the drug delivery via lymphatic transport in the management of diabetes mellitus.

In another study by Han Lei *et al.* (2020), the authors reported the application of yeast display technology for the development of influenza H7N9 oral vaccine. Hemagglutinin (HA) of A/Anhui/1/2013 (AH-H7N9) was presented to the surface of the yeast cells to form recombinant *S. cerevisiae* EBY100. After, the oral administration of *S. cerevisiae* EBY100/pYD5-HA to mice, high level of IgG antibody along with appreciable amounts of cytokines (IFN- γ and IL-4) were detected. The vaccine based on yeast display technology was able to elicit both the humoral and cell-mediated immunity in mice and helped to achieve effective immune protection against (AH-H7N9) virus challenge [35].

Conclusion

Vaccines have proved to be effective, since ages, to combat various infectious pathogens affecting humans and animals. The important characteristics of yeast cells such as easy availability, well known genomic structure, no toxicity with immunostimulatory properties and ability to secrete proteins have made them as an attractive carrier for delivering drugs including proteins, peptides and genes. Yeast, thus represents a potential carrier for delivery of antigens to immune cells using their adjuvant and specific structural properties attributed due to the presence of β -glucan cell wall and induce specific host immune response to manage various diseases and disorders.

Future Perspective

The advanced genetic engineering tools have made possible to display antigens on the surface of the yeast to be used as vaccines. With inclusion of knowledge of nanoscience and nanotechnology coupled with genetic engineering, the recombinant yeast cell could be loaded with nanoparticles for specific targeting to the tissues and even to the cells. This approach would help to achieve specific cellular targeting. In the coming years, yeast based delivery approach represents a powerful platform to change the vaccine delivery systems of DNA, mRNA, proteins and genes to oral route. However, research on physicochemical characteristics of yeast cells, its adhesion and permeation properties needs to be explored further to achieve its adoption widely. With regards to the licensing these yeast based system for human use there is a need to strengthen, improve and

build a potential delivery platform fulfilling the regulatory requirements to assure distribution of safe, stable and immunogenic vaccines. To summarize, the yeast based vaccines have a bright future in the coming years, yes of course by overcoming the hurdles in its way.

References

1. B. Greenwood, The contribution of vaccination to global health: past, present and future, *Philos Trans R Soc Lond B Biol Sci.*, 369(1645), 1-9 (2014).
2. S. Awate , L.A. Babiuk, G. Mutwiri G, Mechanisms of action of adjuvants, *Front Immunol.*, 4(114), 1-10 (2013).
3. V. Sampath, G. Rabinowitz, M. Shah, S. Jain, Z. Diamant, M. Jesenak, R. Rabin S. Vieths, I. Agache, M. Akdis, D. Barber, H. Breiteneder, S. Chinthrajah, T. Chivato W. Collins, T. Eiwegger, K. Fast, W. Fokkens, R.E.O'Hehir, M. Ollert, L.O'Mahony , O.Palomares, O. Pfaar. C. Riggioni, M.H. Shamji, M. Sokolowska, M. Jose Torres C.Traidl-Hoffmann, M. van Zelm, Y. Wang, L. Zhang, C.A. Akdis, K.C. Nadeau, Vaccines and allergic reactions: The past, the current COVID-19 pandemic, and future perspectives, *Allergy*, 76(6), 1640-1660 (2021).
4. K. Duly, F.A. Farraye, S. Bhat, COVID-19 vaccine use in immunocompromised patients: A commentary on evidence and recommendations, *Am J Health Syst Pharm.*, 79(2), 63-71 (2022).
5. O.S Kumru, S.B Joshi, D.E Smith, C.R Middaugh, T. Prusik, D.B.Volkin, Vaccine instability in the cold chain: mechanisms, analysis and formulation strategies, *Biologicals*, 42(5), 237-59 (2014).
6. M. Brisse, S.M. Vrba, N. Kirk, Y. Liang, H. Ly, Emerging Concepts and Technologies in Vaccine Development *Front. Immunol.*, 11, 1-11 (2020).
7. J. Claesen, M.A Fischbach, Synthetic microbes as drug delivery systems, *ACS synthetic biology*, 4(4), 358-364 (2015).
8. C. de Souza Varize, R.M. Christofoleti-Furlan, E. de Souza Miranda Muynarsk, G.V. de Melo Pereira, L.D. Lopes, L.C. Basso, Biotechnological Applications of Nonconventional Yeasts, In: Basso, T. P. , editor. *Yeasts in Biotechnology* [Internet]. London: IntechOpen; (2019).
9. Y. Pan, X. Li, T. Kang, H. Meng, Z. Chen, L. Yang Y. Wu, Y. Wei, M. Gou, Efficient delivery of antigen to DCs using yeast-derived microparticles, *Sci Rep.* 5(10687), 1-9 (2015).
10. K. Ravinder, K. Piyush, Yeast-based vaccines: New perspective in vaccine development and application, *FEMS Yeast*, 19(2), 1-22 (2019).
11. Z. Yang, M. Xu, Z. Jia, Y. Zhang, L. Wang, H. Zhang, J. Wang , M. Song, Y. Zhao Z. Wu, L. Zhao, Z. Yin, Z. Hong, A novel antigen delivery system induces strong humoral and CTL immune responses, *Biomaterials*, 134, 51-63 (2017).
12. R.C. Duke, D. Bellgrau A. Franzusoff, C.C. Wilson, Yeast-antigen compositions and methods of using the same, US8221763B2, US Patent (2001).
13. R. De Smet, L. Allais, C.A. Cuvelier, Recent advances in oral vaccine development: yeast-derived β -glucan particles, *Hum Vaccin Immunother.*, 10 5), 1309-18 (2014).
14. A. Abraham, G. Ostroff, S.M. Levitz, P.C.F. Oyston, A novel vaccine platform using glucan particles for induction of protective responses against *Francisella tularensis* and other pathogens. *Clin Exp Immunol.* 198(2), 143-152 (2019).
15. Y. Moënné-Loccoz, P. Mavingui, C. Combes, P. Normand, C. Steinberg, Microorganisms and Biotic Interactions. In: Bertrand, J.C., Caumette, P., Lebaron, P., Matheron, R., Normand, P., Sime-Ngando, T. (eds) *Environmental Microbiology: Fundamentals and Applications*. Springer, Doedrecht (2015). doi: 10.1007/978-94-017-9118-2_11
16. J.W. Yoo, D.J. Irvine, D.E. Discher, et al. Bio-inspired, bioengineered and biomimetic drug delivery carriers. *Nat Rev Drug Discov.*, 10(7), 521-535 (2011).
17. D.T.O Hagan , R. Rappuoli, The safety of vaccines. *Drug Discov Today.* 9(19), 846-854 (2004).
18. J.S. Lewis, T.D. Zaveri, 2nd C.P. Crooks, B.G. Keselowsky, Microparticle surface modifications targeting dendritic cells for non-activating applications. *Biomaterials*, 33, 7221-7232 (2012).
19. G. Coradello, N. Tirelli, Yeast Cells in Microencapsulation. *General Features and Controlling Factors of the Encapsulation Process. Molecules* (Basel, Switzerland), 26(11), 3123, 1-20 (2021).
20. B.G. De Geest, M.A. Willart, H. Hammad, et al. Polymeric multilayer capsule-mediated vaccination induces protective immunity against cancer and viral infection. *ACS Nano.* 6, 2136-2149 (2012).
21. C. Remondo, V. Cereda, S. Mostböck et al, Human dendritic cell maturation and activation by a heat-killed recombinant yeast (*Saccharomyces cerevisiae*) vector encoding carcinoembryonic antigen,

- Vaccine, 27, 987–94 (2009).
22. H. Huang et al. Distinct patterns of dendritic cell cytokine release stimulated by fungal α -glucans and Toll-like receptor agonists. *Infect. Immun.* 77, 1774–1781 (2009).
 23. A. Madhavan, K.B. Arun, R. Sindhu et al. Customized yeast cell factories for biopharmaceuticals: from cell engineering to process scale up. *Microb Cell Fact* 20, 124 (2021).
 24. A. Ardiani, J.P. Higgins, J.W. Hodge, Vaccines based on whole recombinant *Saccharomyces cerevisiae* cells. *FEMS yeast research.* 10(8), 1060-1069 (2010).
 25. J. Stephenne, Development and production aspects of a recombinant yeast-derived hepatitis B vaccine, *Vaccine*, 8, S69-73 (1990).
 26. J. Zang, Y. Zhu, Y. Zhou, C. Gu, Y. Yi, S. Wang, S. Xu, G. Hu, S. Du, Y. Yin, Y. Wang. Yeast-produced RBD-based recombinant protein vaccines elicit broadly neutralizing antibodies and durable protective immunity against SARS-CoV-2 infection. *Cell Discovery.* 7(1), 1-6 (2021).
 27. H. Lei, S. Jin, E. Karlsson, S. Schultz-Cherry, K. Ye K, Yeast Surface-Displayed H5N1 Avian Influenza Vaccines, *J Immunol Res.*, 2016 (4131324) 1-12 (2016).
 28. E. Iizasa, N. Yukio, Highly efficient yeast-based in vivo DNA cloning of multiple DNA fragments and the simultaneous construction of yeast/*Escherichia coli* shuttle vectors, *BioTechniques*, 40(1), 79-83 (2006).
 29. Silva, Anna Jéssica Duarte et al. Yeasts as a promising delivery platform for DNA and RNA vaccines. *FEMS Yeast Research*, 21, 3 (2021).
 30. M. Thanou, J.C. Verhoef, H.E. Junginger, Chitosan and its derivatives as intestinal absorption enhancers, *Adv Drug Deliv Rev.*, 50(S1), S91-101 (2001).
 31. B. Jyotiranjana et al. Comparative immunogenicity of preparations of yeast-derived dengue oral vaccine candidate, *Microb. Cell Factories*, 17(24), 1-14 (2018).
 32. E. Ivanova E. Yeasts in nanotechnology-enabled oral vaccine and gene delivery. *Bioengineered*, 12(1), 8325-8335 (2021).
 33. S. Nooraei, S.H. Bahrulolum, Z.S. Hoscini, et al, Virus-like particles: preparation, immunogenicity and their roles as nanovaccines and drug nanocarriers, *J Nanobiotechnol.*, 19(59), 1-27 (2021)
 34. C. Sabu, D. Raghav, U.S. Jijith, P. Mufeedha, P.P. Naseef, K. Rathinasamy K. Pramod, Bioinspired oral insulin delivery system using yeast microcapsules, *Mater Sci Eng C Mater Biol Appl.*, 103, 109753 (2019).
 35. H. Lei, B. Xie, T. Gao, Q. Cen Y. Ren, Yeast display platform technology to prepare oral vaccine against lethal H7N9 virus challenge in mice, *Microb Cell Fact.*, 19(1), 53 (2020).

Review Article

A Review on Biomedical Applications of Titanium Dioxide

Pradeep C. Dathan¹, Deepak Nallaswamy¹, S. Rajeshkumar², Suja Joseph¹,
Shahin Ismail¹, Lakshmi Ajithan¹, Leon Jose³¹Department of Prosthodontics, ²Nanobiomedicine Lab, Department of Pharmacology, Saveetha Dental College and Hospitals, SIMATS, Saveetha University, Thandalam, Chennai 602105, India³Department of Mechanical Engineering, Indian Institute of Technology Madras, Chennai 600036, IndiaReceived: 4 February 2023
Accepted: 25 March 2023
Published online: 30 June 2023**Keywords:** titanium, titanium dioxide, titania, nanoparticles, nanotubes, cancer therapy, photodynamic

Titanium is a wonder metal with broad range of application in all aspects of life. Applications include aeronautical, industrial, military, automobiles agriculture and in the field of medicine. Titanium dioxide is the most common compound of titanium it occurs commonly in three crystalline forms namely anatase, rutile and brookite. The nano particles of titanium dioxide have low toxicity, versatile fabrication adaptability which forms the basis for its broad range of application. This review article discusses applications of titanium dioxide nanoparticles in cancer therapy, targeted drug delivery, photodynamic therapy, antibacterial effect, role in bone formation and general applications.

© (2023) Society for Biomaterials & Artificial Organs #20066823

Introduction

The wonder metal titanium was discovered in 1791 by William Gregor in Great Britain. Martin Heinrich Klaproth named it Titanium, after the 'titans' of Greek mythology. The element has an atomic number of 22 and is represented by the symbol Ti in the periodic table. The metal exists in nature as an oxide form and, on reduction, a bright metal with silver color is formed. It has got superior strength, low density and is resistant to corrosion in chlorine, aqua regia and salt water. Kroll and Hunter process is used to extract the metal from its mineral ores [1]. The alloys of Titanium can be formed by alloying titanium with various other metals like molybdenum, iron, vanadium, and aluminum to get light weight alloys with high strength. Its applications are vast, including aeronautical, industrial, military, automobiles and agriculture. In the field of medicine its application includes medical equipment, orthopedic implants, dental implants etc. The alloys can also be used for general application, including jewelry, equipment in sports and building materials. The melting point of titanium is reported as 1668°C, because of this it is commonly used as a refractory metal. The thermal and electric conductivity is low. It is para magnetic and cooling below its critical temperature of 00.49K converts the metal into a superconductor [2-5].

The most common compound of titanium is titanium dioxide (TiO₂) other names include titania or titanium(IV) oxide. It is a naturally occurring compound, formed when oxygen in air reacts with titanium. Titanium tetrachloride (TiCl₄) and titanium trichloride (TiCl₃) are the other compounds [6-8]. The commonly occurring three crystalline forms of titanium dioxide are anatase, rutile and brookite. Anatase as well as brookite are produced in large scale and are important white pigments. Anatase (80%) and Brookite (20%) form the mixed polymers of titanium dioxide and is used extensively for biomedical purposes. American food and drug administration has approved the utilization of titanium dioxide in pharmaceutical products as it is non-toxic and cost effective [9-12].

Nano particles of titanium dioxide have low toxicity, versatile fabrication adaptability and a smaller size which makes it a compound with a broad range of application. They have excellent cytocompatibility and enhances the proliferation, differentiation and spreading of osteoblast cells [12,13]. Titanium dioxide nanoparticles like titania nano tubes (NTs) are stable against disintegration when used as surface coating on implants. They also act as a delivery system that controls the drug release in implants [14]. TiO₂NTs has a porous structure which promotes bone regeneration and repair [15-19]. There is ample evidence in the literature which proves that titanium dioxide nano particles are inert and compatible when used in human body. This review

* Corresponding author
E-mail address: dathanphd@gmail.com (Pradeep C. Dathan)

discusses the future challenges and biomedical applications of titanium dioxide.

Structure and Properties

The dioxide forms of titanium have an octahedral geometry with six oxide anions are bonded to it. These oxide anions remain attached to three titanium centers. One of the dioxide rutile form has got a tetragonal crystal structure, whereas anatase and brookite exhibit orthorhombic structure. The oxygen substructures in rutile shows close packing with slight distortions. Distorted hexagonal close packing of oxide anion is found in anatase, whereas in brookite the crystal structure is cubic close packing and double hexagonal close packing.

Applications of Titanium Dioxide

Titanium in cancer therapy

Chemotherapeutic agents can cause cytotoxicity on normal cells. To overcome this currently nano technology is applied in the diagnosis and treatment of cancer [16-20]. In nano technology nano structures that deliver and release drugs are developed. The therapeutic effect of the drug is increased and at the same time the adverse effect of the chemotherapeutic agents is reduced by aiming only the diseased cells by these nano structures which acts as vehicle [21]. Since the drugs are delivered to the target and drug release is controlled, the healthy normal cells remain unaffected, this reduces the side effects. TiO_2 nano structures has the ability to enhance the therapeutic effect of conventional chemotherapeutic agents by delivering it to specific sites and by controlling the drug release. This is achieved mainly because of its high biocompatibility, non-toxicity and harmonious drug releasing ability.

Targeted/smart delivery of drugs

The therapeutic effect of anti-neoplastic drug can be enhanced by surface modified nano particles, these nano particles deliver the chemotherapeutic agent to the affected cell and reduces the toxicity of drug [16,18,20]. Studies have highlighted that TiO_2 nanostructures based chemotherapeutic agents increased the therapeutic effect of antineoplastic drugs. The application of titanium dioxide whiskers (TiO_2 Ws) for drug delivery in cancer treatment was investigated by Li et al and found that the intracellular potency of Daunorubicin (DNR) can be increased by TiO_2 Ws and it also enhances the anti-tumor efficacy of DNR in hepatocarcinoma

cells (SMMC- 7721). This is an indication for the use of TiO_2 Ws as drug delivery vehicle for DNR into the specific cells. They concluded that TiO_2 Ws based drug delivery is a favorable approach in the treatment of cancer [22]. According to Akram et al combination of Doxorubicin and titanium dioxide nano particles (TiO_2 NPs) had synergistic effect in breast cancer cell lines [23].

Venkatasubbu et al. reported the anti-neoplastic effect of paclitaxel attached to modified hydroxyl apatite and TiO_2 NPs. Biochemical analysis showed superior anti-neoplastic activity of surface modified paclitaxel attached to hydroxyl apatite and TiO_2 NPs when compared to paclitaxel [24]. The nano structure mediated smart drug delivery increased the therapeutic effect of anti-neoplastic drugs, minimizes the toxicity and enhances the biological availability and time dependent delivery of drugs.

Photodynamic therapy in cancer treatment

TiO_2 NPs is widely used in photodynamic therapy (PDT). In PDT a photosensitizing agent is administered for localizing the tumor and is activated using a light of specific wavelength [25]. This therapeutic technique has an illumination source a photosensitizer (PS) and an oxygen molecule. A non-toxic photosensitizer is introduced into the living tissues and are activated by photons from the illumination source. This transfers energy into the oxygen molecule and produces singlet oxygen ($^1\text{O}_2$) and reactive oxygen species (ROS) [26, 27]. PDT is considered as a viable alternative non-invasive treatment for cancer [28-30]. This treatment modality is successful in superficial areas and natural cavities where invasive surgery is of great risk [31-33]. Its efficacy in deep seated tumors remains questionable, as light cannot penetrate into deeper tissues and generation of singlet oxygen and other reactive oxygen species with curative quantity becomes difficult. PDT is proven to be more efficient against skin and oral infections [34,35].

In the early stages, TiO_2 NPs were activated with ultraviolet light of less than 385nm wavelength. It can create light induced holes and electrons, which can react with hydroxyl ions of water (OH^-) to form powerful oxidative radicals (OH^\cdot , HO_2^\cdot). These oxidative radicals can destroy bacteria, fungi and tumor cells. High photocatalytic efficiency, low toxicity and excellent photo stability of TiO_2 makes its application in cancer treatment a success. Fujishima et al first reported the photo destructive activity of TiO_2 to malignant cells [36]. Surface of TiO_2 electrode was cultured with Hela cells and UV irradiation was used to anodically polarize the

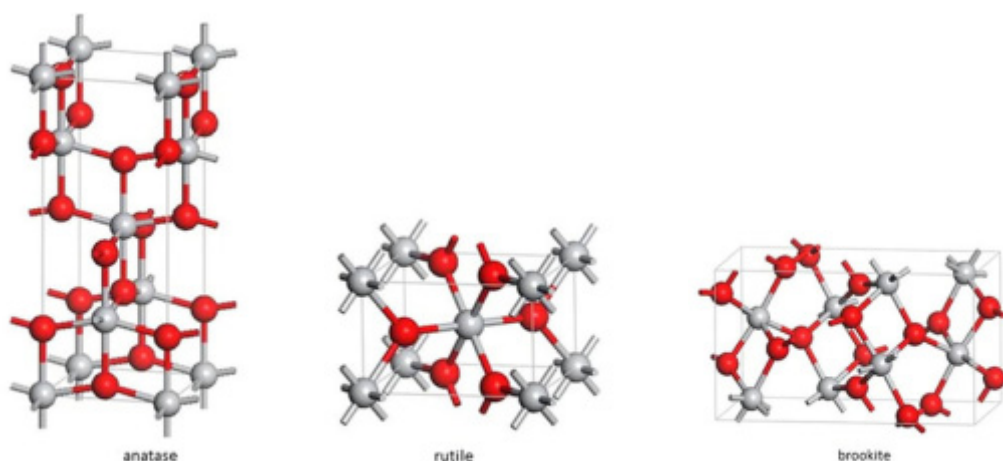


Figure 1: Crystal forms of anatase rutile and brookite

Table 1: Properties of titanium

Chemical formula	TiO ₂
Appearance	White solid
Odour	Odourless
Molecular mass	79.866 g/mol
Boiling point	2972°C
Solubility in water	Insoluble
Magnetic susceptibility (χ)	+5.9 · 10 ⁻⁶ cm ³ /mol
Refractive Index (n_D)	2.488 (anatase)
	2.583 (brookite)
	2.609 (rutile)

electrode. This caused damage of Hela cell membrane. The neoplastic cells were not destroyed when the electrodes were 10 mm away from the surface of cell. A TiO₂ microelectrode which was polarized and illuminated showed selective anti-tumor activity for single T24 cell which are cancerous [37]. Seo et al. used high temperature non hydrolytic method to make water soluble TiO₂NPs. These nanoparticles were short and rod shaped with diameter of 3.5 nm and length of 10.4 nm, which was highly toxic to human melanoma cells (A375) in the presence of UV irradiation [38]. UV light was used to activate TiO₂ but this light source was found to be damaging, therefore visible light was used to activate TiO₂ which produced a positive effect. The optical activation of TiO₂ with visible light was adapted through dye-adsorbed and doping methods. In dye-adsorbed method hypericin B [39], chlorine e [40] and zinc phthalocyanine [41] was used as PDT sensitizers whereas in doping methods metal elements (Pt,Fe) [42-44] and non-metal elements (C,N) [45-47] have been used. Li et al. synthesized nitrogen doped TiO₂NPs (N-TiO₂). Calcination of anatase TiO₂NPs was done under an ammonia atmosphere. The obtained N-TiO₂NPs had a higher absorbance and anti-tumor activity in the visible region than pure TiO₂NPs [48-50].

The anti-neoplastic effect of TiO₂ is effective but tumor cells were not specifically destroyed. Improved TiO₂NPs which identify and bind the receptors of neoplastic cells were developed. This increased the specific destruction of tumor cells and reduced the death of normal cells. Monoclonal antibody proteins (CEA, 83 pre-S1/S2, 84 IL13a2R85 and EGFR86) with high affinity and specificity were immobilized on the surface of TiO₂NPs. The NPs are directed towards the neoplastic cells as the monoclonal antibody proteins are over expressed on their surface.

TiO₂ antibacterial effect

Compared to other antimicrobial agents nanotechnology based materials like metal and metal oxides are effective microbicidal agents with more safety and stability [51-53]. The photocatalytic microbicidal action of TiO₂ was first reported by Matsunaga et al. (1985), when they investigated the antimicrobial effect of TiO₂ against *Lactobacillus acidophilus*, *Saccharomyces cerevisiae* and *E. Coli* [54]. Ahmed et al. found that multi drug resistant *P. aeruginosa* associated infections were effectively treated with TiO₂NPs and antibiotics [55]. Inhibition of bacterial growth by TiO₂NPs was due to its nanometric scale and powerful oxidizing ability.

Antibacterial effect of ZnO₂ and TiO₂NPs against metallo beta lactamase and biofilm producing *Pseudomonas aeruginosa* was reported by Vincent et al. [56]. Antibacterial action against *P.*

aeruginosa was evident when TiO₂NPs was preexposed to UV radiation. ROS which causes cell wall lysis was formed on exposure of sixty minutes [57]. TiO₂ photo catalyst can disinfect a broad spectrum of microorganisms which have a deleterious effect on cellular respiratory activity and can result in cell death [58]. This property is used in tooth paste it also enhances the antimicrobial activity on dental plaque. Rimjim et al. suggested its effectiveness in both aerobic and anaerobic bacteria [59]. The strong oxidizing power of TiO₂ by free radicals like hydroxyl and superoxide anion radicals reduces the growth of *E. coli* and *staphylococcus* [60]. Roy et al. concluded that the antibacterial action of beta lactams, cephalosporins, aminoglycosides, glycopeptides, macrolides, lincosamides and tetracycline was enhanced against methicillin resistant *staphylococcus aureus* [61].

Surface modification of implants with TiO₂NPs provides antibacterial property and enhances osteogenic activity [62,63]. Liu et al. confirmed that implant efficacy improved when TiO₂NPs along with zinc was used in proper concentration this was due to cytocompatibility and antibacterial functions [64]. Ti dental implants when modified with multiple layer of TiO₂ nano network increases the cell adhesion, proliferation and mobility [65]. When heat and plasma treatment was compared it was seen that plasma treatment reduces the adhesion of *prophyromonas gingivalis* without affecting the activity of osteoblast. The heat treated group at 400°C was the most suitable for dental implants because of optimum osteoblast and anti-bacterial activity [66]. Vishnu et al. reported that hydrothermal treatment of etched Ti implants at 225°C for five hours altered the topography and enhanced the antibacterial effect against methicillin resistant *staphylococcus aureus*. These Ti implants improved the calcium deposition by osteoblast and was not cytotoxic against mammalian cells [67].

Titanium dioxide and bone formation

Titanium and its alloys are used as implants in bones as they have superior strength, stability, elastic modulus similar to the elastic modulus of tissues and ability and capability to form a thin stable oxide layer that is resistant to corrosion. TiO₂ nano structures have been successfully used in implants because of its nano topographical characteristics. Low toxicity, flexibility, high corrosion resistance and high tensile strength makes the titanite nanostructures a powerful candidate for implants [68]. Surface properties, micro topography, nanotopography and composition are the key factors for integration of implants with live bone.

Various research has concluded that titanium dioxide surface properties promote attachment of bone forming cells. The bioactivity of crystalline TiO₂ is associated with existence of hydroxyl groups on the surface and negative charges that are induced which in turn draw calcium and then phosphorous ions from the body fluids to the surface of implant. It has also been reported that during change in structure of titanium dioxide layer from anatase to rutile the rate of dissolution of metallic ions are substantially reduced in a stimulated body fluid.

TiO₂ is a bioactive factor which upregulates ALP activity. Haugen demonstrated the ability of porous TiO₂ scaffold to promote new bone formation without causing inflammation and tissue necrosis in a peri implant cortical defect. The bone volume increased significantly when the defects were treated with the TiO₂ scaffolds. Histologically presence of newly formed bone was seen in close proximity with scaffold surface and the cortical section of the defect showed new bone formation. The newly formed bone present in the marrow space put forward the suggestion that the TiO₂ scaffold has the ability to act as a material with osteoconductive properties.

The study concluded by highlighting the ability of TiO₂ scaffold to integrate well with bone and this ability can be utilized to enhance formation of bone and growth of bone adjoining implants as well as bone formation in larger defects [69].

Chung et al. created a uniform non porous structure on titanium implant by coating it with hydroxyl apatite -TiO₂ (HApTiO₂) and immobilize BMP-2 on the surface. The proper porous structure of HApTiO₂ encouraged cell growth and adhesion leading to the time reduction in bone healing at implant bone interface [70]. Mohammedi et al. reported that presence of TiONPs in calcium phosphate cement increases the mechanical strength when used in repair of bone defects. Surface area and porous structure of TiO₂NTs increased due to nanometric thickness, this promoted cell adhesion and improved bone capabilities [72]. TiO₂ NTs diameter influence cell adhesion and osseointegration. Collagen type-I (Col-I) was adsorbed with a higher outcome and faster speed when TiO₂NTs of diameter of 100 nm compared to 30 nm diameter. Hydrogen bond and van der Waals forces that existed between Col-I molecules and TiO₂NTs was the driving force in adsorption mechanism [73]. The length also influenced adhesion, longer the length less was the adhesion. 0.04 μm length of TiO₂NTs have increased adhesion strength compared to NTs with length of 2 μm, this was because of less interfacial stress [74]. Surface topography of dental implants influences osseointegration. Dental implants showed high percentage of osseointegration when the surface of implants were coated with TiO₂ NTs through anodic oxidation and were loaded with BMP₂ [75]. TiO₂ NTs possess good blood compatibility therefore it can be used for surface modification of blood contacting implants, biological molecules like Gly- Arg- Gly- Asp-Ser peptide when immobilized on TiNTs improved osseointegration in dental implants [76]. Jin and his co-workers found that osteoblast adhesion was enhanced when TiO₂ NTs less than 100 nm diameter was used. It also upregulated the alkaline phosphatase enzyme which clearly indicates the bone forming potential and bone tissue interaction of orthopedic implants coated with TiO₂NTs [77]. Huang et al. pointed out that the surface chemistry, structure, wettability and crystalline phase of TiO₂NTs had a positive effect in platelet rich plasma properties. It was found that cell adhesion, migration, proliferation and differentiation improved when properties such as wettability, surface texture and chemistry was altered [78].

Titanium dioxide films and coatings have high biocompatibility and is resistant to corrosion, therefore its use as bone anchored implants are extensively studied. The coatings of TiO₂ on implant surface is accomplished through various methods like laser ablation, dip coating, sol-gel process, heat treatment, electrochemical methods, sputtering, thermal spraying etc. Fabrication of TiO₂ film makes it a bioactive coating and this allows the implant to bond with the surrounding bone by enhancing the growth of calcium phosphate layer on TiO₂ film in presence of body fluids. The nano topography of surface of dental implants enhances blood response, cell adhesion and osseointegration of dental implants and adds to the success of the implants.

Other Applications of Titanium Dioxide

The titanium dioxide has a wide range of applications in pharmaceutical industry. It is used as an active ingredient in various medications. The inherent property of titanium dioxide to absorb UV light and its capacity to scatter light can be utilized to extend the shelf life of pharmaceutical products. TiO₂ protects the active photosensitive ingredient present in the pharmaceutical preparation against UV light and heat degradation and there by enhances the safety and efficacy of drugs [79].

The opacifying and pigmentation ability of titanium dioxide helps to maintain color uniformity over time. As different colors of medication indicate different doses eg: Warfarin, also color indication helps in diagnosis of drug over dosage or intoxication in emergency rooms, therefore color stability of drug plays a significant role, the uniformity and consistency in the maintenance of color ensures pharmaceutical safety [79]. This helps the medical professionals and patients to differentiate medications especially in people with limited eye sight. TiO₂ nano coating on maxillofacial silicone elastomers reduces its color degradation compared with silicone's that are noncoated. Maxillo facial silicones with surface nano coating of ALD TiO₂ was a novel color stable material to be used potentially in extra oral maxillofacial silicone processes [80]. The wound healing ability of titanium dioxide was demonstrated by Sankar et al. TiO₂ nano particles exhibited enhanced wound repair, wound contraction, matured collagen deposition and epithelialization in the wound [81].

A research conducted by Langle et al concluded that TiO₂ can be considered as an appropriate vehicle in the delivery of active substances to treat diabetes mellitus. TiO₂ Stevia Rebaudiana Bertoni (20 and 30 μm) combination has a potent and prolonged anti diabetic activity [82]. A similar conclusion was derived from another research by Samyuktha et al as TiO₂ exhibited alpha amylase inhibition which highlights its anti-diabetic effect [83].

Adverse Effects of Nano TiO₂

Inert nano materials when administered to human body through injections can perform differently. Oral, transdermal/inhalation are the routes of exposure which can cause adverse effects on vital organs including respiratory system [84], gastro intestinal tract, reproductive system, excretory system, circulatory system and nervous system [85]. One of the nano materials commonly studied for pulmonary toxicity is TiO₂ [86]. It is reported that chronic exposure of nano TiO₂ in murine models can cause inflammation, epithelial hyperplasia and pulmonary carcinoma [87]. The size of particles also affects the toxicity; it is reported that large size TiO₂ is comparatively less toxic than smaller sized. It was also seen that in murine models TiO₂ nano particles can cause lesion in brain and fatty degradation of the hippocampus [88]. On the basis of these toxicity of nano structures used in bio medical application needs to be thoroughly evaluated before use. Therefore, careful evaluation of toxicity and clinical outcome of TiO₂ is required before applying in clinical practice.

Conclusion

Titanium dioxide has a wide range of application in all aspects of daily life. As titanium dioxide has the ability to absorb ultra violet light it protects the skin from ultraviolet radiation. This property extends its use in sunscreen lotions, cosmetic products and skin care products. Photo catalytic activity of titanium dioxide results in thin coatings which exhibits self-cleansing and disinfection properties on exposure to ultra violet radiations. Alloys of titanium are characterized by being light weight, very high tensile strength even at high temperatures, high corrosion resistance and ability to withstand high temperature makes the wonder metal titanium as an ideal metal to be used in air crafts, pipes for power plants, Armour plating, naval ships, space crafts and missiles. Unique properties such as non-toxicity, bio compatibility and affordability made TiO₂ nano structure and their composites to gain attention and use in biomedical field. Researches demonstrate that TiO₂ nano structures are safer than any other nano material for bio medical application. Chemo therapeutic agents for clinical applications when modified by TiO₂ NPs improved the bioavailability and the release

time of chemotherapeutic agents. The uniqueness of TiO₂ nano materials is non toxicity and nano topographical characteristics. These characteristics made the material available for the use in orthopedic and dental implants. There are numerous studies in literature that give evidence for the potential of titanium and its oxides to be used as bone, dental and drug releasing implants. Considering all the above mentioned aspects it can be concluded that titanium, titanium dioxide and nano materials based on titanium dioxide can be judiciously and effectively used as valuable material for dental implants and other biomedical applications.

References

1. Lide, D. R., ed., CRC Handbook of Chemistry and Physics (86th ed.). Boca Raton (FL): CRC Press. (2005).
2. Titanium, Columbia Encyclopedia (6th ed.). New York: Columbia University Press. 2000–2006 (2000).
3. Stwertka, Albert, Titanium, Guide to the Elements (Revised ed.). Oxford University Press. pp. 81–82 (1998).
4. Baan R, Straif K, Grosse Y, Secretan B, El Ghissassi F, Coglianò V. Carcinogenicity of carbon black, titanium dioxide, and talc. *Lancet Oncol.*, 7(4), 295 (2006).
5. Bavykin DV, Friedrich JM, Walsh FC. Protonated titanates and TiO₂ nanostructured materials: synthesis, properties, and applications. *Adv Mater.*, 18(21), 2807–2824 (2006).
6. Encyclopaedia Britannica. 2006. Retrieved 19 January 2022
7. Steele, M.C.; Hein, R.A., Superconductivity of Titanium. *Phys. Rev.* 92(2), 243-247 (1953).
8. Thiemann, M. et al., Complete electrostatics of a BCS superconductor with eV energy scales: Microwave spectroscopy on titanium at mK temperatures, *Phys. Rev. B.* 97(21), 214516 (2016).
9. McCullagh C, Robertson JM, Bahnemann DW, Robertson PK. The application of TiO₂ photocatalysis for disinfection of water contaminated with pathogenic micro-organisms: a review. *Res Chem Intermed.*, 33(3–5), 359–375 (2007).
10. Bonetta S, Bonetta S, Motta F, Strini A, Carraro E. Photocatalytic bacterial inactivation by tio2-coated surfaces. *AMB Express.*, 3(1), 59 (2013).
11. El, Goresy; Chen, M; Dubrovinsky, L; Gillet, P; Graup, G, An ultradense polymorph of rutile with seven-coordinated titanium from the Ries crater. *Science.* 293(5534), 146770 (2001).
12. Gao A, Hang R, Huang X, et al. The effects of titania nanotubes with embedded silver oxide nanoparticles on bacteria and osteoblasts. *Biomaterials.*, 35(13), 4223–4235 (2014).
13. Hang R, Gao A, Huang X, et al. Antibacterial activity and cytocompatibility of cu–ti–o nanotubes. *J Biomed Mater Res A.*, 102(6), 1850-1858 (2014).
14. Xu Z, Jiang X. Rapid fabrication of tio2 coatings with nanoporous composite structure and evaluation of application in artificial implants. *Surf Coat Technol.*, 381, 125094 (2020).
15. Weetall HH. Biosensor technology what? Where? When? And why? *Biosens Bioelectron.*, 11(1–2), i–iv (1996).
16. Razavi H, Janfaza S. Medical nanobiosensors: a tutorial review. *Nanomed J.*, 2(2), 74–87 (2015).
17. Janfaza S, Nojavani MB, Nikkhal M, Alizadeh T, Esfandiari A, Ganjali MR. A selective chemiresistive sensor for the cancer-related volatile organic compound hexanal by using molecularly imprinted polymers and multiwalled carbon nanotubes. *Mikrochim Acta.*, 186(3), 137 (2019).
18. Hashemzadeh H, Allahverdi A, Peter E, N-M H. Comparison between three-dimensional spheroid and two-dimensional monolayer in a549 lung cancer and pc9 normal cell lines under treatment of silver nanoparticles. *Modares J Biotechnol.*, 10(4), 573–580 (2019).
19. Esfandiyari J, Shojaedin-Givi B, Mozafari-Nia M, Hashemzadeh H, Naderi-Manesh H. Diatom biosilica shell manipulation with gold, spion nanoparticles and trastuzumab with aims of diagnostics of her2 cells. *Modares J Biotechnol.*, 10(4), 581–588 (2019).
20. Zabarjadi A, Hashemzadeh H, Taravat E. Telomere, chromosome end, and telomerase enzyme as a cancer biomarker. *Genet Third Millennium.*, 11(1), 3018–3027 (2013).
21. Hashemzadeh H, Javadi H, Darvishi MH. Study of structural stability and formation mechanisms in dspc and dpsm liposomes: a coarse-grained molecular dynamics simulation. *Sci Rep.*, 10(1), 1837 (2020).
22. Li Q, Wang X, Lu X, et al. The incorporation of daunorubicin in cancer cells through the use of titaniumdioxide whiskers. *Biomaterials.*, 30(27), 4708–4715 (2009).
23. Akram MW, Raziq F, Fakhar-e-Alam M, et al. Tailoring of au-TiO₂ nanoparticles conjugated with doxorubicin for their synergistic response and photodynamic therapy applications. *J Photochem Photobiol a Chem.*, 384, 112040 (2019).
24. Venkatasubbu GD, Ramasamy S, Reddy GP, Kumar J. in vivo and in vivo anticancer activity of surface modified paclitaxel attached hydroxyapatite and titanium dioxide nanoparticles. *Biomed Microdevices.*, 15(4), 711–726 (2013).
25. T. J. Dougherty, C. J. Gomer, B. W. Henderson, G. Jori, D. Kessel, M. Korbelik, J. Moan and Q. Peng, Photodynamic therapy: *Natl Cancer Inst.*, 90(12), 889-905 (1998).
26. T.A. Heinrich, A.C. Tedesco, J.M. Fukuto and R.S. da Silva, *Dalton Trans.*, 43, 4021–4025 (2014).
27. M.A. Biel, in *Biofilm-based Healthcare-associated Infections*, Springer, 119–136 (2015).
28. M. Triesscheijn, P. Baas, J.H. Schellens and F.A. Stewart, Photodynamic therapy in oncology, *Oncologist*, 11(9), 1034-44 (2006).
29. R. R. Allison and C. H. Sibata, photodynamic therapy photosensitizers: a clinical review, 7(2), 61-75 (2010).
30. A. Fujishima, J. Ohtsuki, T. Yamashita and S. Hayakawa, *Photomed. Photobiol.*, 8, 45 (1986).
31. R.J. Skyrme, A.J. French, S.N. Datta, R. Allman, M.D. Mason and P.N. Matthews, *BJU Int.*, 95, 1206–1210 (2005).
32. L. E. Rhodes, M. de Rie, Y. Enström, R. Groves, T. Morken, V. Goulden, G. A. Wong, J.-J. Grob, S. Varma and P. Wolf, *Arch. Dermatol.*, 140, 17–23 (2004).
33. H.I. Hung, J.M. Schwartz, E.N. Maldonado, J. J. Lemasters and A.L. Nieminen, *J. Biol. Chem.*, 288, 677–686 (2013).
34. D. Ferguson, A. Perry, M.E. Wood, P.G. Winyard and M. Whiteman, *Free Radical Biol. Med.*, 76, S135 (2014).
35. R.G. Lopes, M.E.S.O. Santi, B.E. Franco, A.M. Deana, R.A. Prates, C.M. França, K.P.S. Fernandes, R.A.M. Ferrari and S.K. Bussadori, *Lasers Med. Sci.*, 5, 146–152 (2014).
36. R. Cai, K. Hashimoto, Y. Kubota and A. Fujishima, Induction of cytotoxicity by photoexcited TiO₂ particles, *Chem. Lett.*, 52(8), 2346-8 (1992).
37. Sakai, H., Baba, R., Hashimoto, K., Fujishima, A. and Heller, A., Local Detection of Photoelectrochemically Produced H₂O₂ with a Wired Horseradish-Peroxidase Microsensor. *The Journal of Physical Chemistry*, 99, 11896-11900 (1995).
38. J.W. Seo, H. Chung, M.Y. Kim, J. Lee, I.H. Choi and J. Cheon, *Small*, 3, 850 (2007).
39. S. Xu, J. Shen, S. Chen, M. Zhang and T. Shen, *J. Photochem. Photobiol.*, B, 67, 64 (2002).
40. Y. Tokuoka, M. Yamada, N. Kawashima and T. Miyasaka, *Chem. Lett.*, 35, 496 (2006).
41. T. Lopez, E. Ortiz, M. Alvarez, J. Navarrete, J. A. Odriozola, F. Martinez-Ortega, E. A. Pa'ez-Mozo, P. Escobar, K. A. Espinoza and I. A. Rivero, *Nanomed.: Nanotechnol., Biol. Med.*, 6, 777 (2010).
42. A Jan, Wolnicka-Gubisz, Urbanska, G. Stochel, W. Macyk, Photodynamic activity of platinum(IV) chloride surface-modified TiO₂ irradiated with visible light. *Photochem. Photobiol.*, B, 92, 54 (2008).
43. R Damoiseaux 1, S George, M Li, S Pokhrel, Z Ji, B France, T Xia, E Suarez, R Rallo, L Mädlar, Y Cohen, E M V Hoek, A Nel: No time to lose-high throughput screening to assess nanomaterial safety, 3(4), 1345-60 (2011).
44. S. George, S. Pokhrel, Z. Ji, B. L. Henderson, T. Xia, L. Li, J. I. Zink, A. E. Nel and L. Mädlar, *J. Am. Chem. Soc.*, 133, 11270 (2011).
45. Z. Hu, Y. Huang, S. Sun, W. Guan, Y. Yao, P. Tang and C. Li, *Carbon*, 50, 994 (2012).
46. Asahi, R., Morikawa, T., Ohwaki, T., Aoki, K. and Taga, Y. (2001) Visible-Light Photocatalysis in Nitrogen-Doped Titanium Oxides. *Science*, 293, 269-271.79 J. Zhong, F. Chen and J. L. Zhang, *J. Phys. Chem. C*, 114, 933 (2010).
47. Z. Li, L. Mi, P. N. Wang and J. Y. Chen, *Nanoscale Res. Lett.*, 2011, 6, 356.
48. Y. Cong, J. Zhang, F. Chen, M. Anpo, and D. He, "Preparation, Photocatalytic Activity, and Mechanism of Nano-TiO₂ Co-Doped with Nitrogen and Iron (III)," *J. Phys. Chem. C*, 111, 10618-10623 (2007).
49. M. Abdulla-Al-Mamun, Y. Kusumoto and M. S. Islam, Synergistic cell-killing by photocatalytic and plasmonic photothermal effects of Ag@TiO₂ core-shell composite nanoclusters against human epithelial carcinoma (HeLa) cells. *Chem.*, 22, 5460 (2012).
50. J. Xu, Y. Sun, J. Huang, C. Chen, G. Liu, Y. Jiang, Y. Zhao and Z. Jiang, *Bioelectrochemistry*, 71, 217 (2007).
51. McCullagh C, Robertson JM, Bahnemann DW, Robertson PK. The application of TiO₂ photocatalysis for disinfection of water contaminated with pathogenic micro-organisms: a review. *Res Chem Intermed.*, 33(3–5), 359–375 (2007).

52. Calamak S, Shahbazi R, Eroglu I, Gultekinoglu M, Ulubayram K. An overview of nanofiber-based antibacterial drug design. *Expert Opin Drug Discov.*, 12(4), 391–406 (2017).
53. Kaviyarasu K, Geetha N, Kanimozhi K, et al. in vivo cytotoxicity effect and antibacterial performance of human lung epithelial cells a549 activity of zinc oxide doped tio2 nanocrystals: investigation of biomedical application by chemical method. *Mater Sci Eng C.*, 74, 325–333 (2017).
54. Matsunaga T, Tomoda R, Nakajima T, Wake H. Photoelectrochemical sterilization of microbial cells by semiconductor powders. *FEMS Microbiol Lett.*, 29(1–2), 211–214 (1985).
55. Ahmed FY, Farghaly Aly U, Abd El-Baky RM, Waly NGFM. Comparative Study of Antibacterial Effects of Titanium Dioxide Nanoparticles Alone and in Combination with Antibiotics on MDR Pseudomonas aeruginosa Strains. *Int J Nanomedicine.*, 15, 3393-3404 (2020).
56. Vincent MG, John NP, Narayanan PM, Vani C, Murugan S. In vitro study on the efficacy of zinc oxide and titanium dioxide nanoparticles against metallo beta-lactamase and biofilm producing Pseudomonas aeruginosa. *J Appl Pharm Sci.*, 4(7), 41–46 (2014).
57. Arora B, Murar M, Dhumale V. Antimicrobial potential of Tio2 nanoparticles against MDR Pseudomonas aeruginosa. *J Exp Nanosci.*, 10(11), 819–827 (2015).
58. Maness P, Smolinski S, Blake DM, Huang Z, Wolfrum EJ, Jacoby WA. Bactericidal activity of photocatalytic TiO₂ reaction: toward an understanding of its killing mechanism. *Appl Environ Microbiol.*, 65(9), 4094–4098 (1995).
59. Rimjhim AT. Analysis of Antimicrobial Activity of Titaniumdioxide Nanoparticles on Aerobic and Anaerobic Dental Isolates.
60. de Dicastillo, C.L. , Correa, M.G. , Martínez, F.B. , Streitt, C., Galotto, M.J. Antimicrobial Effect of Titanium Dioxide Nanoparticles. In: Mare, M. , Lim, S.H.E. , Lai, K. , Cristina, R. , editors. Antimicrobial Resistance - A One Health Perspective [Internet]. London: IntechOpen (2020).
61. S. Roy, Aashis; Parveen, Ameena; R. Koppalkar, Anil; Prasad, M. V. N. Ambika, Effect of Nano - Titanium Dioxide with Different Antibiotics against Methicillin-Resistant Staphylococcus Aureus. *Journal of Biomaterials and Nanobiotechnology*, 1(1), 37–41 (2010).
62. Azzawi ZG, Hamad TI, Kadhim SA, Naji GA-H. Osseointegration evaluation of laser-deposited titanium dioxide nanoparticles on commercially pure titanium dental implants. *J Mater Sci Mater Med.*, 29(7), 96 (2018).
63. Souza JC, Sordi MB, Kanazawa M, et al. Nano-scale modification of titanium implant surfaces to enhance osseointegration. *ActaBiomater.*, 94, 112–131 (2019).
64. Liu W, Su P, Chen S, et al. Antibacterial and osteogenic stem cell differentiation properties of photoinduced tio2 nanoparticle-decorated tio2 nanotubes. *Nanomedicine.*, 10(5), 713–723 (2015).
65. Choi SH, Jang YS, Jang JH, Bae TS, Lee SJ, Lee MH. Enhanced antibacterial activity of titanium by surface modification with polydopamine and silver for dental implant application. *J Appl BiomaterFunct Mater.*, 17(3), 2280800019847067 (2019).
66. Ji M-K, Oh G, Kim J-W, et al. Effects on antibacterial activity and osteoblast viability of non-thermal atmospheric pressure plasma and heat treatments of tio2 nanotubes. *J Nanosci Nanotechnol.*, 17(4), 2312–2315 (2017).
67. Vishnu J, Manivasagam VK, Gopal V, et al. Hydrothermal treatment of etched titanium: a potential surface nano-modification technique for enhanced biocompatibility. *Nanomedicine.*, 20, 102016 (2019).
68. Williams DF. On the mechanisms of biocompatibility. *Biomaterials.*, 29(20), 2941–2953 (2008).
69. Lars M. Bjursten; Lars Rasmusson; Seunghan Oh; Garrett C. Smith; Karla S. Brammer; Sungho Jin, Titanium dioxide nanotubes enhance bone bonding in vivo., 92(3), 1218-24 (2010).
70. Chen H-I, Shu H-Y, Chung C-J, He J-L. Assessment of bone morphogenic protein and hydroxyapatite–titanium dioxide composites for bone implant materials. *Surf Coat Technol.*, 276, 168–174 (2015).
71. Mohammadi M, Hesaraki S, Hafezi-Ardakani M. Investigation of biocompatible nanosized materials for development of strong calcium phosphate bone cement: comparison of nano-titania, nano-silicon carbide and amorphous nano-silica. *Ceram Int.*, 40(6), 8377–8387 (2014).
72. Brammer KS, Frandsen CJ, Jin S. TiO₂ nanotubes for bone regeneration. *Trends Biotechnol.*, 30(6), 315–322 (2012).
73. Yang W, Xi X, Ran Q, Liu P, Hu Y, Cai K. Influence of the titania nanotubes dimensions on adsorption of collagen: an experimental and computational study. *Mater Sci Eng C.*, 34, 410–416 (2014).
74. Yang W, Xi X, Ran Q, Liu P, Hu Y, Cai K. Influence of the titania nanotubes dimensions on adsorption of collagen: an experimental and computational study. *Mater Sci Eng C.*, 34, 410–416 (2014).
75. Hu N, Wu Y, Xie L, et al. Enhanced interfacial adhesion and osseointegration of anodic TiO₂ nanotube arrays on ultra-finegrained titanium and underlying mechanisms. *Acta Biomater.*, 106(1), 360–375 (2020).
76. Kim G-H, Park S-W, Lee K, et al. Evaluation of osteoblast-like cell viability and differentiation on the gly-arg-gly-asp-ser peptide immobilized titanium dioxide nanotube via chemical grafting. *J Nanosci Nanotechnol.*, 16(2), 1396–1399 (2016).
77. K.S. Brammer, S. Oh, C.J. Cobb, L.M. Bjursten, H. van der Heyde and S. Jin, *Acta Biomater.*, 5, 3215–3223 (2009).
78. Huang HH, Chen JY, Lin MC, Wang YT, Lee TL, Chen LK. Blood responses to titanium surface with tio2 nano-mesh structure. *Clin Oral Implants Res.*, 23(3), 379–383 (2012).
79. Das, R., Ambardekar, V., Bandyopadhyay, P.P. Titanium Dioxide and Its Applications in Mechanical, Electrical, Optical, and Biomedical Fields. In: Ali, H. M. , editor. Titanium Dioxide - Advances and Applications [Internet]. London: IntechOpen
80. <https://tdma.info/the-essential-role-of-titanium-dioxide-in-pharmaceuticals/>
81. Bishal AK, Wee AG, Barão VAR, Yuan JC, Landers R, Sukotjo C, Takoudis CG. Color stability of maxillofacial prosthetic silicone functionalized with oxide nanocoating. *J Prosthet Dent.*, 121(3), 538-543 (2019).
82. Langle, Ariadna; González-Coronel, Marco Antonio; Carmona-Gutiérrez, Genaro; Moreno-Rodríguez, José Albino; Venegas, Berenice; Muñoz, Guadalupe; Treviño, Samuel; Díaz, Alfonso, Stevia rebaudiana loaded titanium oxide nanomaterials as an antidiabetic agent in rats. *Revista Brasileira de Farmacognosia*, 25(2), 145–151 (2015).
83. Samyuktha PS, Ganapathy DM, Rajeshkumar S. In Vitro Study Of Antidiabetic Effect Of Green Synthesised Titanium Dioxide Nanoparticles. *Natural Volatiles & Essential Oils Journal*, 25, 7260-70 (2021).
84. Sankar, Renu; Dhivya, Ravishankar; Shivashangari, Kanchi Subramanian; Ravikumar, Vilwanathan, Wound healing activity of Origanum vulgareengineered titanium dioxide nanoparticles in Wistar Albino rats. *Journal of Materials Science: Materials in Medicine*, 25(7), 1701–1708 (2014).
85. B. L. Baisch, N. M. Corson, P. Wade-Mercer, R. Gelein, A. J. Kennell, G. Oberdorster and A. Elder, *Part. Fibre Toxicol.*, 11, 5 (2014).
86. W. McKinney, M. Jackson, T. Sager, J. Reynolds, B. Chen, A. Afshari, K. Krajnak, S. Waugh, C. Johnson and R. Mercer, *Inhalation Toxicol.*, 24, 447–457 (2012).
87. Nogueira CM, de Azevedo WM, Dagli ML, Toma SH, Leite AZ, Lordello ML, Nishitokukado I, Ortiz-Agostinho CL, Duarte MI, Ferreira MA, Sipahi AM. Titanium dioxide induced inflammation in the small intestine. *World J Gastroenterol.*, 18(34), 4729-35 (2012).
88. G. Oberdörster, E. Oberdörster and J. Oberdörster, *Environ. Health Perspect.*, 113, 823–839 (2005).